Université
de Strasbourg

UNIVERSITE DE STRASBOURG

msii
ÉCOLE DOCTORALE

ÉCOLE DOCTORALE MSII (ED n° 269)
LABORATOIRE ICUBE (UMR 7357)

THÈSE
présentée par :

Wenhui YU

soutenance le 10 avril 2019

pour obtenir le grade de docteur de : **Docteur de l'Université de Strasbourg**
Discipline Spécialité : Electronique, Microélectronique, Photonique

Mesure de distance absolue utilisant l'interférométrie à balayage de longueur d'onde étalonnée par un peigne de fréquences

Thèse dirigée par :

M. PFEIFFER Pierre	Maître de conférence HDR, Université de Strasbourg
M. FONTAINE Joël	Professeur, Co directeur , INSA de Strasbourg

Rapporteurs :

M. CHASSAGNE Luc	Professeur , Université Versailles Saint-Quentin
M. LINTZ Michel	Chargé de recherche , HDR, Observatoire de la Côte d'Azur Nice

Examinateurs :

M. SALVADE Yves	Professeur, Haute Ecole Arc Saint-Imier (Suisse)
M. LEONARD Jérémie	Chargé de recherche, CNRS, Université de Strasbourg

Abstract

In this thesis, we implemented a high-precision absolute distance measurement (ADM) system using frequency sweeping interferometry (FSI). The FSI technique requires the frequency tuning range of the swept laser to be measured with high accuracy and precision, which is challenging due to the lack of an easy way to measure the high frequency of a sweeping laser in real time. In this thesis, a frequency comb has been used for measuring the frequency tuning range of the sweeping laser. A frequency comb formed by a femtosecond laser consists in millions of evenly spaced comb lines, so that it can be regarded as a light frequency ruler. The frequency calibration of the sweeping laser was realized by filtering the heterodyne signal between the sweeping laser and the comb lines using a narrow bandpass filter. This approach allows us to detect the calibration signal when the frequency of the sweeping laser is in the vicinity of a comb line. As the frequency interval between the comb lines can be precisely measured or actively phase-locked against a stable radio-frequency (RF) oscillator, the tuning range of the sweeping laser could be measured with high accuracy. Especially, each two calibration peaks can be used in the calculation of distance, which we call 'sub-measurements' in a single sweeping. Combined with the large number of the comb lines, averaging of the sub-measurements improves greatly the measurement precision without multiple sweeping.

In the thesis, the conditions of detecting and the characteristics of the heterodyne signal between the sweeping laser and the comb line are presented. A filter design for filtering the heterodyne signal is performed. A modeling work concerning the effect of the phase noise of lasers on the envelope distortion of the calibration peak has been presented.

Experimental works based on the measurement concepts have been carried out. It shows that using the proposed measurement scheme can greatly improve the distance measurement precision. In one of the measurements, a precision of 30 nm for a distance around 0.8 m, corresponding to 37×10^{-9} relative uncertainty has been achieved. The result was obtained based on a fringe counting signal processing method. The high precision was obtained thanks to the large number of sub-measurements and the stability of the evenly spaced comb lines. We have found that vibration measurement of the target can be also performed taking the advantage of the dense comb lines. A high sensitivity, limited by 1.7 nm noise RMS, of vibration measurement has been achieved. This result allows us to monitor the vibration of the target, which is an important issue of FSI technique.

Acknowledgments

Being a PhD student pushes me to face many challenges not only in academic research, but also in all aspects of life. Yet, at the end of my PhD life in ICube Laboratory, I suddenly realized that I have never gain so much in such a short time. I wish to acknowledge all those who have helped and supported me for the past three and half years.

My most grateful thanks to my supervisor, Dr. Pierre Pfeiffer, not just for his dedicated guidance in research, but also for all the patience and inculcation. He has not only taught me the knowledge about the topic, but also showed the spirit of doing research.

My immense gratitude to my co-supervisor Prof. Joël Fontaine, without whom I would not have the chance to do my PhD here. Even though we are not at the same place for most of the time, he always finished many things at the first time. I want to thank his guidance throughout my studying in the ICube Lab.

Many thanks to all the IPP members, who make the office a great place to work. Special thanks go to Sylvain Lecler, who helped a lot in different ways and for the revision of my first research article; to Paul Montgomery, who guided me to solve many problems; to Amandine Elchinger for her revision of my papers and the writing training; and to Patrice Twardowski, Manuel Flury and Gérard Philippe for their beneficial discussions on different problems. I would like to thank Alireza Morsali for his discussions during the daily coffee break among us and for his help in many aspects.

Great thanks to all my Chinese friends in Strasbourg, who make an alien living remotely from his hometown do not feel lonely. Specially, I want to thank Dr. Jianming Yang, with whom I have discussed a lot of different topics from serious scientific issues to philosophy and to many amusing jokes; thank Dr. Lihong Liu, who is so kind that always help me to deal with different problems; We have had a very good time on the tram every workday when we went back home; thank Chenchen Liu, with whom we have had many happy moments. Also thank Shangzhi Chen, Xiaopo Zhen and Ye Yuan *et al*. I wish them both all the best in their life.

Mostly, I want to thank my parents for their endless support. I deeply feel regret for not being able to accompany with them, especially in some gathering moments for the others like right now. On this occasion, I want to convey my deep love to them. Also, I want to thank the other family members for their concerning. Wish you all the best.

The author gratefully acknowledges the financial support for this work from the China Scholarship Council (CSC).

Table of Contents

List of Figures

List of Abbreviations

ADM	Absolute Distance Measurement
AMCW	Amplitude Modulation Continuous Wave
ATLAS	A Toroidal LHC Apparatus
CCD	Charge Coupled Device
CERN	Conseil Européen pour la Recherche Nucléaire
c.w.	Continuous Wave
DAQ	Data AcQuisition board
ECLD	External Cavity Laser Diode
ESA	European Space Agency
FAST	Five-hundred-meter Aperture Spherical radio Telescope
FIR	Finite Impulse Response
FMCW	Frequency Modulation Continuous Wave
FSI	Frequency Sweeping Interferometry
FWHM	Full Width at Half Maximum
GPIB	General Purpose Interface Bus
GPS	Global Positioning System
IF	Intermediate Frequency
LHC	Large Hadron Collider
LiDAR	Light Detection and Ranging
LISA	Laser Interferometer Space Antenna
LO	Local Oscillator
LTI	Linear Time-Invariant
MS/s	Mega Sample points per Second
MWI	Multiwavelength Interferometry
NASA	National Aeronautics and Space Administration

NBF	Narrow Bandpass Filter
OPD	Optical Path Difference
PDF	Probability Density Function
ppm/ppb	Part-Per-Million/Part-Per-Billion
PZT	Piezoelectrical Transducer
RF	Radio Frequency
RMS	Root-Mean-Square
RR	Retro Reflector
SCPI	Standard Commands for Programmable Instruments
SNR	Signal-to-Noise Ratio
TIA	Transimpedance Amplifier
TLS	Tunable Laser Source
TOF	Time-of-Flight

List of Symbols

v_{SN}	Normalized tuning speed of the tunable laser source
BW	Bandwidth of filters
c	Speed of light in vacuum, 299 792 458 m/s
D	Measured geometric distance
$\Delta\nu$	Optical frequency tuning range of the tunable laser
$\delta\nu$	Laser linewidth
Δx	Difference of two values of x
δx	Absolute error of x
σx	Relative error of x, which is $\frac{\delta x}{x}$
$E(t)$	Electric field of light
ε	Fractional phase
f	Electric frequency
f_N	Electric frequency normalized to the bandwidth of a bandpass filter.
f_0	Carrier-envelope offset frequency of frequency comb; Initial frequency
f_r	Repetition frequency of frequency comb
ϕ	Phase of the electric field of light
φ	Phase difference of the electric fields of light in interferometers or heterodyne detector
i, j	Units of imaginary number, $i, j = \sqrt{-1}$
$\boldsymbol{k}$	Wave vector of light
L	Measured Optical path difference (OPD)
λ	Wavelength of light
n	Phase refractive index
ν	Optical frequency of lasers
P	Power of light

π	Ratio of a circle's circumference to its diameter
R	Response of photodetector
v_S	Tuning speed of the tunable laser source

Introduction

High precision distance metrology plays a fundamental role in many scientific and technological applications, including larger-scale assembly, satellite formation flying and precision manufacture, to name a few. Traditional laser interferometry achieved nanometer-scale precision with a non-ambiguity range of half of the wavelength, thus only suitable for displacement measurement. In this thesis, a technique named frequency sweeping interferometry (FSI) is implemented for absolute distance measurement (ADM), which measures distances longer than the wavelength without moving of the target. The frequency of the light source is swept linearly in FSI. Due to the difference of propagation time between a reference arm and the unknown distance, a beat signal is generated between the two beams from the reference arm and the measurement arm. The beat frequency is proportional to the tuning speed of the swept laser and the distance. This technique is similar to the existing frequency modulation continuous wave (FMCW) in the radio frequency (RF) domain, in which the distance resolution is proportional to the frequency tuning range. Since lasers can be tuned with higher broadband compared to RF sources, typically in the range of hundreds of GHz, the resolution can reach hundreds of micrometers.

The challenge is that lasers can only be tuned in a quasilinear manner, which deteriorates the distance measurement accuracy and resolution. Active linearization of the laser tuning function faces the problem of rising excess laser noise and rising required feed-back bandwidth for large tuning range and high sweeping rate. Passive linearization requires the frequency tuning range of the sweeping laser be measured with high accuracy. It was commonly realized using high finesse Fabry-Perot etalon, auxiliary interferometer with well-known length or transition lines of molecule/atom in gas cell. However, the instability of the Fabry-Perot etalon and reference interferometer introduces distance measurement uncertainty and the transition lines of the molecule/atom are too broad and therefore introduce large uncertainty.

In this thesis, we use a frequency comb formed from a femtosecond laser to measure the tuning range of the sweeping laser. An optical frequency comb contains a large number, typically in the order of 10^6, of optical frequencies components that are evenly spaced by hundreds of megahertz. More important, the absolute frequencies of the components can be fully controlled and stabilized by two RF frequencies, namely the offset frequency f_0 and the repetition frequency f_r; the frequency of the n^{th} components can be expressed as: $\nu_n = nf_r + f_0$, where n is an integer in the order of 10^6. Therefore, the optical frequency combs build a bridge to connect the RF with the optical domain. The unique properties of frequency combs make them be widely applied in the state-of-the-art metrology systems, which are described in the first chapter of this thesis.

The existing applications of combs in distance metrology were mostly using combs for stabilization of static lasers, such as to increase the accuracy of multi-wavelength interferometry. In the present work, we explore the ability of the combs in the calibration of dynamic laser frequency. Using an electronic filter, we are allowed to detect the calibration signal when the frequency of the sweeping laser is in the vicinity of a comb line. As it will be seen in the following chapters, the proposed comb-calibrated frequency sweeping interferometry allows us to greatly improve the measurement accuracy and precision. This is achieved on one hand due to the fact that the intervals of the comb lines are directly referenced to a highly stable frequency oscillator-a frequency counter in our case. High accuracy of the frequency tuning range, which is the dominant distance measurement uncertainty in frequency sweeping interferometry, thus can be achieved. On the other hand, we can perform a large number of sub-measurements in only one sweeping period using each comb lines. Averaging the sub-measurement results will decrease the statistical uncertainty by the order of $\sqrt{N}$, where N is the number of the sub-measurements. In other word, it is equivalent to the measurement result of thousands of sweeping in a time as short as one sweeping.

The thesis is organized as the following:

In the first chapter, we start with a review of some typical applications of absolute distance metrology in a variety of domains, along with the most common methods performing ADM. The working principles of these optical methods are given, aiming at discussing the merits, such as range, precision and complexity, of different methods.

In chapter 2, theoretical backgrounds of frequency sweeping interferometry and frequency combs are introduced. We will see some important considerations of using FSI in ADM, such as the distance drift amplification effect, chromatic dispersion of the medium, *etc*. The concept of our measurement scheme is introduced at the end of this chapter.

Chapter 3 focuses on the heterodyne detection between a tunable laser and the frequency comb as well as the filter design for the heterodyne signal filtering. This chapter presents the ability of frequency calibration using a frequency comb and heterodyne filtering approach. The measurement results of the nonlinear tuning of the tunable laser are presented.

In chapter 4, we describe the modeling work concerning the phase noise effect of the lasers on the shape of the calibration signal. It deals with the phenomenon we observed in our experiment that the envelope of the filtered calibration peaks is deteriorated compared to the ideal signal. We assume that this phenomenon is caused by the phase noise of the lasers. The modeling results show some important information on how the phase noise affects the envelope. In the present work, only Gaussian white noise was taken into consideration due to the fact that the 1/f noise plays a role in a longer time than the sweeping time across the comb lines.

In chapter 5, we present the experimental setup and the results of distance measurement using the proposed method. We will see that high precision ADM as well as vibration measurement are achieved. Measurement uncertainties will be presented.

Chapter 6 contains the conclusion and some perspectives for future work.

Chapter 1. Research and Applications of Absolute Distance Measurement (ADM)

As one of basic physical quantities, distance between two objects gives much valuable information in scientific and technological fields. The ultrahigh precision distance measurement based on laser interferometry makes the 'nearly impossible'[1] detection of the gravitational wave possible, opening a new window for us to observe the universe. The global positioning systems (GPS) have been playing important role both in military and civil fields for positioning and navigation. Light ranging and detection (LiDAR) systems map our world in three-dimension (3D) [1], providing abundant information of our environment. High precision displacement sensors in photolithography allows the wafers to be positioned with accuracy of sub-nanometer scale [2]. Long range precision laser metrology allows large scale industrial components, such as aeroplanes and turbines, being assembled with micron or even sub-micron precision [3]. Today, the precision distance measurements are mostly based on lasers as the interrogation carrier. Compared to radar (radio ranging and detection) systems, lightwave can achieve higher lateral selectivity and better longitudinal resolution, thanks to the better directionality and shorter wavelength in electromagnetic spectrum. Using lightwave as the measuring carrier also has the advantages of non-contact, fast and long-range compared to other distance measurement methods, such as mechanical contact of stylus, capacity and Eddy current sensor [4].

Conventional laser interferometry achieves nanometer range precision, but the maximum non-unambiguous range is only half of the wavelength. To measure larger distance, the auxiliary reflector, such as a spherically mounted retroreflector, should be displaced continuously from a reference point to the target. Once the laser beam has been interrupted during measurement, the above displacement procedure should be performed again. In some applications, where displacement measurement is unpractical, the absolute distance measurement (ADM) is required. The absolute distance between two objects is measured without moving the reflecting mirror. Due to the 2π phase wrapping of lightwave, it should be modulated either for amplitude, phase or frequency, in order to obtain the absolute distance. In the following sections, different modulation strategies can be found in various measurement methods.

---

[1] The gravitational wave is so weak that Einstein wrote, 'If we take into account that $\chi = 1.87 \times 10^{-27}$, then we see that A must in all conceivable cases have a practically vanishing value' in *Approximately integration of gravitational field equations*, session reports of the Royal Prussian Academy of Sciences (Berlin), 1916.

In this chapter, a review on some of the typical applications of absolute distance metrology is presented, including LiDAR, large-scale metrology, scientific projects alignments and space missions; then some of the optical techniques performing ADM are introduced, including the principle of measurement and state-of-the-art relating to these techniques.

1.1. Applications of ADM

The ADM is widely needed both in scientific and industrial domains, with different measuring range, resolution and precision. This is because dimensional measurement provides a spatial sensing of our world and can greatly affect the systematic performance of instruments. In this section, some typical applications of ADM are listed.

1.1.1 Light Detection and Ranging (LiDAR)

LiDARs have been used in a wide range of applications, especially in the automatic driving area in recent days. They map their surroundings in 3D by measuring the distance in the direction of transmitted light and by steering the beam to different orientations. Point clouds are obtained with high spatial resolution, as shown in Fig. 1.1. Combined with state-of-the-art artificial intelligent technique, the point cloud can be analyzed by the automotive to identify different targets and predict their behavior.

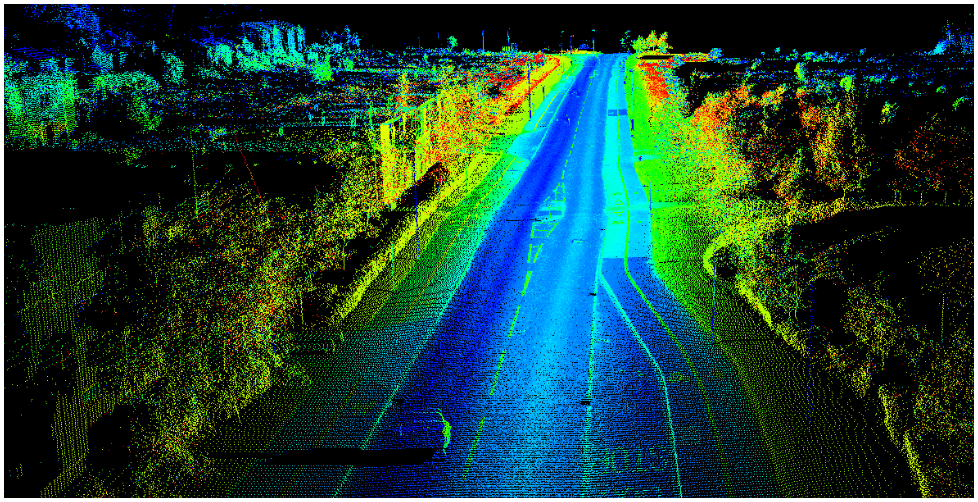

Fig. 1.1. Point cloud obtained from a LiDAR. From Gallery of AEye Corp™.

The LiDAR point cloud shown in Fig. 1.1 is obtained commonly using pulsed time-of-flight (TOF) method. It is gathered by sending short light pulses, typically in nanoseconds [5], and received the reflected pulses from the target by an optical receiver. The system clock records the flight time of the pulses and is used in calculating the distance of the target by multiplying the speed of light. The working principle of pulse TOF is detailed in section 1.2.1. There are many different LiDARs with various beam steering mechanisms and ranging principles. Most LiDARs measure the distance based on pulse time-of-flight (see Section 1.2.1), but frequency modulation continuous wave (FMCW) LiDAR is emerging for automatic driving that features velocity measurement along with the distance measurement. For auto driving application, the laser wavelength is most around 900 nm, but the 1550 nm has been used recently; the advantage is that higher power can be emitted due to eye safety in this wavelength and longer distance can be measured. The difficulty is that it cannot be detected with silicon detector, so that more expensive material like InGasAs should be used. LiDARs have also been applied in remote sensing, geodesy, geomatics, seismology, forestry, atmospheric physics etc.

1.1.2 Large-Scale Assembly

Large-scale metrology refers to the measurement and positioning of large machines and structures ranging from tens to hundreds of meters. The challenge is that, as the observation by Puttock in 1978, “it is necessary in almost every case to adapt available instrumentation and techniques to meet particular requirements and a considerable degree of ingenuity is a necessary attribute of the metrologist undertaking work in this field.” [6]. Even though, there does exists some versatile tools, such as laser tracker and LiDAR, that have been used in different applications. Common techniques used in the large-scale assembly are shown in Fig. 1.2, in which the absolute distance metrology involved in the optical systems is our main concern. The ability to measure large artefacts accurately is a key enabling technology to improve quality and facilitate automation. In terms of quality, precision measurement allows higher efficiency, less energy consuming and better performance.

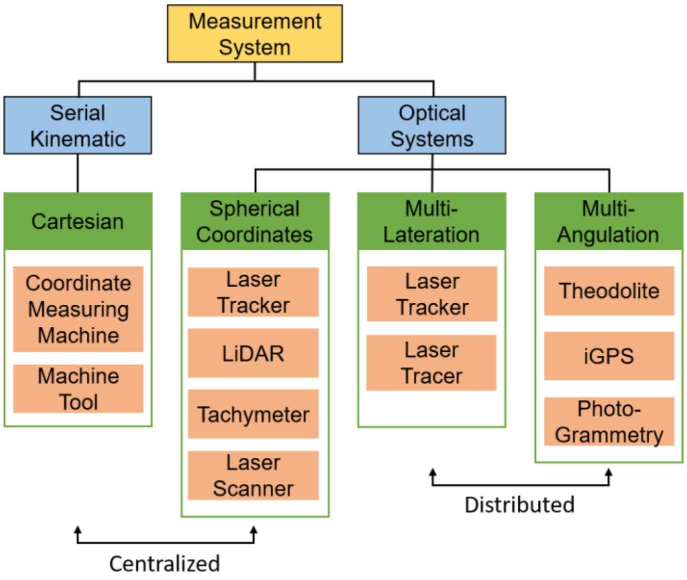

Fig. 1.2. Classification of large-scale metrology. A centralized system is a stand-alone unit that can independently measure the coordinate of a point on an object. A distributed system consists of several independent units whose measured data are jointly processed in sequence for the system to determine the coordinates of a point. Adapted from Ref. [3].

Here we list some aspects relating to the application of distance measurement in large-scale assembly.

1.1.2.1 Manufacturing and Assembly of Aeroplane Components

Traditional methods for aeroplane assembly rely on large fixed tools as shown in Fig. 1.3(a). The quality of assembly is thus affected by the positioning precision of the hard tools. In order to ensure the quality, the tools should be periodically certified, which is time and cost-consuming. The fixed tools also have the drawback that they are designed for the assembly of a specific product thus cannot be applied for the other models.

Fig. 1.3. Aeroplane assembly. (a). Traditional assembly based on hard tooling. (b). Measurement-assisted assembly using laser trackers.

The aeroplane producer, Airbus company, are now building new measurement-assisted assembly, shown as in Fig. 1.3(b). Based on laser trackers, the positions of the fuselage or wings are monitored dynamically. It is commonly assumed that, compared to a 'conventional' assembly process, using the measure-assisted assembly method produces many benefits, including drastically reducing the cost of tooling and jigs, producing a more repeatable assembly junction, improving junction tolerance achievement, allow a large range of station flexibility etc. Besides, three main principles [7, 8] are commonly used to fulfill the requirement of the high accuracy as well as large size: theodolites, photogrammetry and laser ranging techniques.

1.1.2.2 Laser Trackers and Laser Scanner

A laser tracker is a spherical coordinate measurement instrument consisting of following units: laser head, angular measurement unit, steering mechanics, distance measurement unit, and beam position sensor. A typical configuration of laser tracker is depicted in Fig. 1.4. Early versions, and even many latest, of laser tracker are equipped with a He-Ne laser interferometer for measuring radial displacement. The first tracking laser interferometer, was demonstrated in 1986 by Lau *et al*. [9], motivated by the need for rapid, high-accuracy measurements of the positioning errors of industrial robots. Before measuring the dimension of the object under measurement, the spherically mounted retroreflector (SMR) moves continuously from a home point from the laser tracker to the object. Then the SMR moves continuously along the profile of the object to complete measurement. The orientation of the laser tracker traces the movement of the SMR by the signal from the position sensing device so that the laser beam always points at the SMR. Meanwhile, the two-axis angular measurement device record the angular position of the steer mirror, forming spherical coordinate measurement.

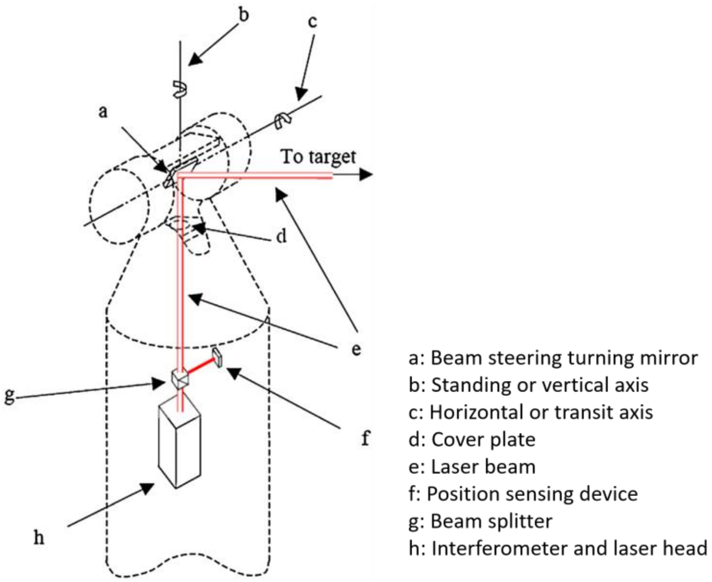

Fig. 1.4. Schematic of the configuration of a laser tracker.

Since the interferometer measures the distance by counting the fringes during the SMR displacement, any event of a break of the beam will fail the measurement. Because there are many tasks where it is a challenge to complete measurements without breaking in the beam, tracker manufactures began introducing ADMs in addition to He-Ne interferometers in their systems. Performances of these laser trackers in ADM metrology is around $10\ \mu\mathrm{m} \pm 0.5\ \mu\frac{\mathrm{m}}{\mathrm{m}}$. One of the current commercial laser tracker producers is FARO, which can be found in a variety of applications in large-scale metrology [6].

1.1.3 Alignment of Large Scientific Instruments

In most cases, the large scientific instruments require high precision of dimensional measurement to fulfill the theoretical specifications. Universal distance measurement instruments such as laser tracker sometimes cannot be used due to the hostile environment and high requirements in terms of precision, speed and robustness. Here we list two examples of how the ADM is applied in alignment of large scientific instruments.

1.1.3.1 ATLAS Project

The semiconductor tracker in A Toroidal LHC Apparatus (ATLAS) detector in CERN (stands for the French name: Conseil Européen pour la Recherche Nucléaire) was used to record the energy and momentum of the particles produced by proton-proton collisions at the Large Hadron Collider (LHC). The measurement performance of the semiconductor tracker, shown in Fig. 1.5(a) is expected to degrade by 20% if there is an unobserved relative misalignment in the three-dimensional position of the detector elements of order 10 μm. This sets a baseline requirement for the geodetic alignment precision of 10 μm in three dimensions and corresponds to a 1 μm length measurement precision requirement for each grid line.

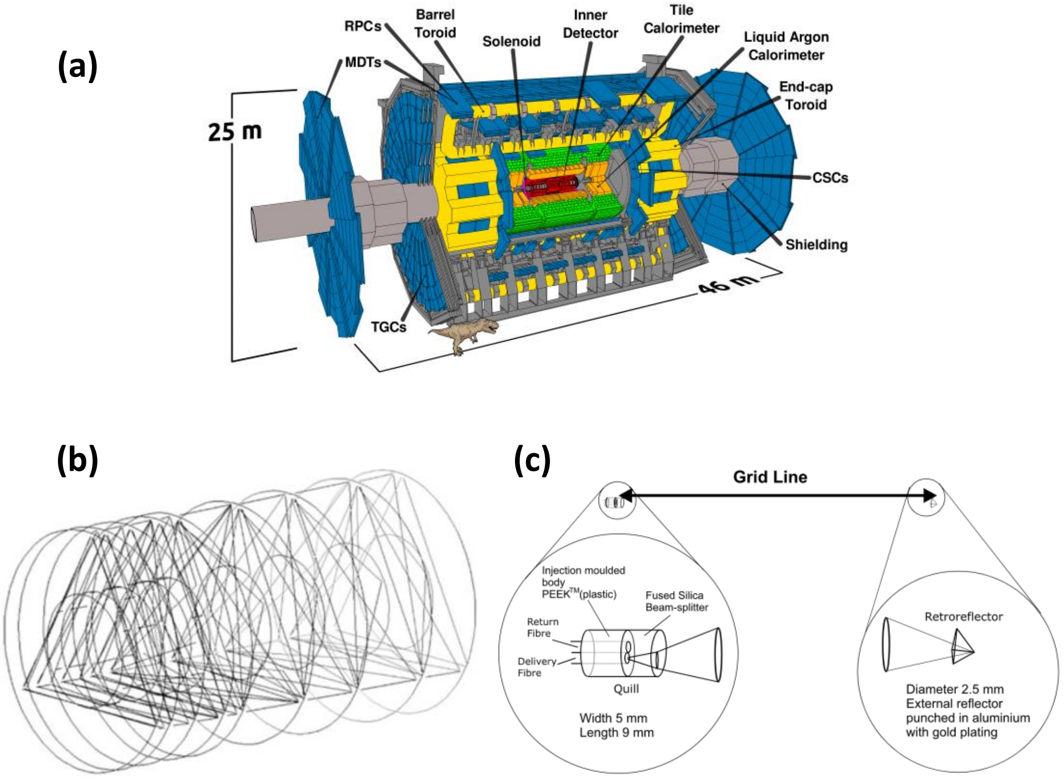

Fig. 1.5. (a). The ATLAS semiconductor tracker. (b). An example design for the geodetic grid connecting the nine support rings. The length of each line is measured by a grid line interferometer of the design shown in (c). Schematic of a grid line interferometer designed for ATLAS. After Ref. [10].

As shown in Fig. 1.5(b) and (c), the lengths of the supporting grid lines are monitored by fiber interferometers. Due to the high radiation levels inside ATLAS, measurements will be made remotely. The robust design is needed for monitoring changes in tracker shape over ten years, because there will be no access to the interferometers for realignment or replacement.

1.1.3.2 <u>Five Hundred Meters Aperture Spherical radio Telescope (FAST)</u>

The FAST is currently the largest radio telescope in the world, which the overall reflective surface of the telescope has a spherical shape. However, in order to observe different zenith of sky, only 300 m aperture is illuminated, as shown in Fig. 1.6(a). The feed cabin follows the focus surface, while the illuminated surface changes from spherical to parabolic shape to focus the signal from the remote universe.

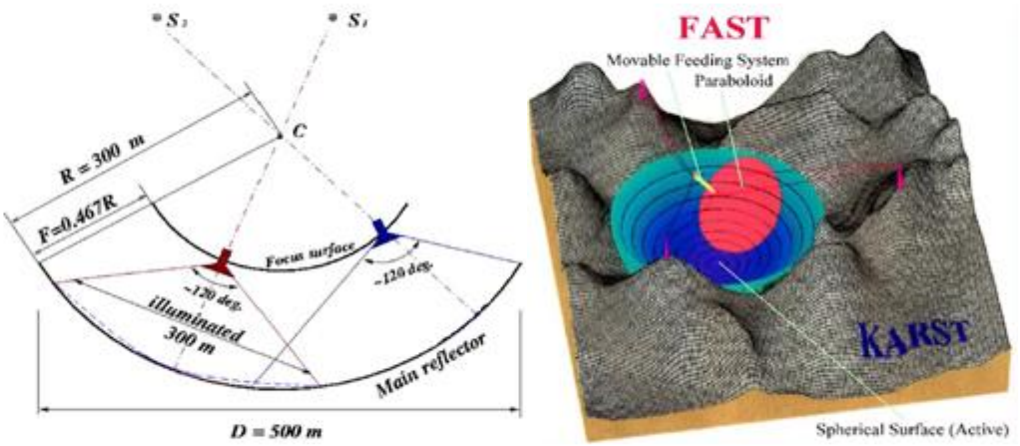

Fig. 1.6. (a) FAST geometrical configuration and (b) the concept. After Ref. [11].

FAST is a telescope where all parts are movable. High-accuracy measurements and control technologies are required to read the spatial coordinates precisely and quickly over long distances for both driving the focus cabin and shaping the main reflector accurately. To measure the position and orientation of the focus cabin, a measuring instrument with an accuracy of 2 mm and refreshing rate of more than 10 Hz is required over a distance of about 300 m. Measurement techniques have been tested on different scaled down models of FAST, indicating that no single technology is available on the market that could fully meet the requirements of FAST. GPS with a sampling rate of 10 Hz can only achieve the accuracy of 1 cm; Total Station can work over long distance but for static targets; laser trackers have both high accuracy and high sampling rate but not over great distances; a one-dimensional charge-coupled device(CCD) refreshes at 20 Hz with an accuracy of 5 mm; the inertial measurement unit owns accelerators and gyros with high accuracy and high sampling rate but cannot work for long time continuously.

For the focus cabin, three steps of mechanical and optical methods ensure the positioning. First, the six cables will be driven by six sets of servo-mechanisms controlled by a central computer, so that the movement of the focus cabin along its caustic trajectory can be realized. Secondly, a group of receivers with multibeam feeds will be mounted on a stabilizer in the focus cabin. A laser ranging system, the third part, will be adopted to accurately measure the position of the feed in real time. The final pointing accuracy of the cable car configuration achieved is 0.52 mm on a 50 m model.

For the reflective surface, a photographic approach would be ideal to measure. There are 80 measuring subfields in the outer ring with a scanning period of 5 s and an accuracy of 0.5 mm. This fits well to the requirements of the measuring task for the reflector. The laser ranging system for the FAST is shown in Fig. 1.7.

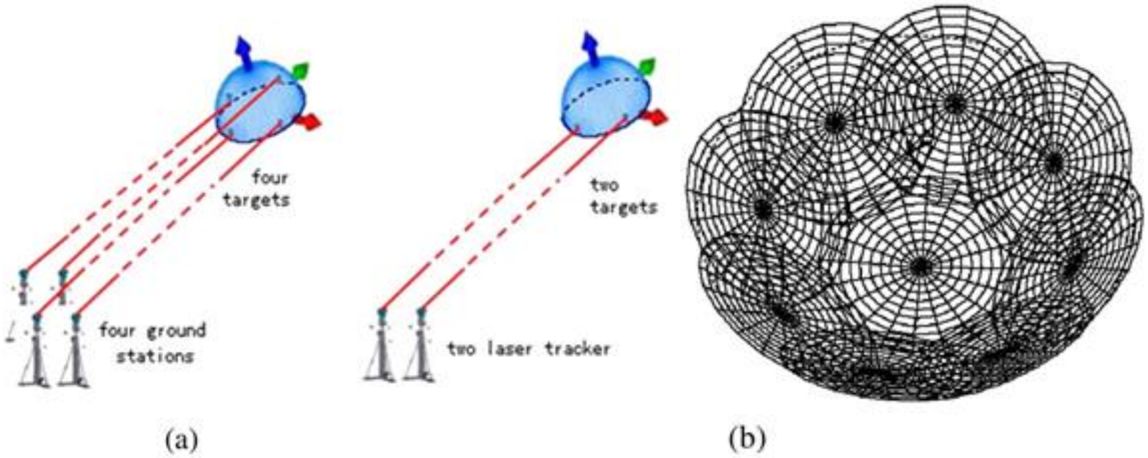

Fig. 1.7. (a) The measuring instruments for driving the focus cabin: two laser trackers (right) and four total stations (left) will be employed. (b) Nine sections for the cameras to photographically measure the shape of the reflector. After Ref. [12].

1.1.4 Satellite Formation Flying

Satellite formation flying involves several satellites working together. Three different types of formations are possible to accomplish different missions. The first one is the 'trailing' formation, in which multiple satellites orbit on the same path to view a target at different times or obtain varied viewing angles of the target. Notable pairs are NASA's EO-1 with Landsat-7 and Terra with Aqua. The EO-1 satellite flies only 60 seconds (450 kilometers) behind Landsat-7 and maintains the separation within ± 3 km by autonomous controlling. This amount of precision was be achieved by onboard GPS system.

The second formation flying is 'constellation', in which a number of satellites with coordinated ground coverage, operating together under shared control. Examples for constellation formation are the navigation satellite systems, such as GPS by United States of America, Galileo by the European Union, BDS by China, and GLONASS by Russia. Distance between the receiver and the satellite is measured coarsely by the flight time of a code that synchronized between the two and more finely measured by the phase shift of the radio wave.

The third formation flying is 'cluster', which is formed by satellites in a dense tightly spaced arrangement. These arrangements are best for high resolution interferometry. Examples of satellite formation flying are the ESA's DARWIN mission, where five satellites flying 25 meters away and the LISA gravitational-wave space detector, where three satellites flying 2.5×10^6 kilometers away.

1.1.4.1 DARWIN Mission

DARWIN mission was proposed *to direct detection and study Earth-type planets and characterize them as possible abodes of life*. To eliminate the strong light of the parent star, nulling interferometry [12] was adopted. It consists of six 1-meter scale satellites separated by about 25 m, as shown in Fig. 1.8. A nulling interferometer can best be described by considering two telescopes. By restricting the beams coming from each of the telescopes to the diameter of the point spread function, and after making the light beams parallel, we can introduce a phase shift of $\varphi = \pi$ into one of the ray paths, which will achieve destructive interference on the optical axis of the system (in the combined beam). At the same time, we will have constructive interference a small angle θ away. This angle θ depends on the distance between the two input telescopes. The output of this system is a set of interference fringes, with a sharp 'null' in its center. By placing the central star under this null, and the planet under a bright fringe, one can effectively diminish the bright light of the parent star.

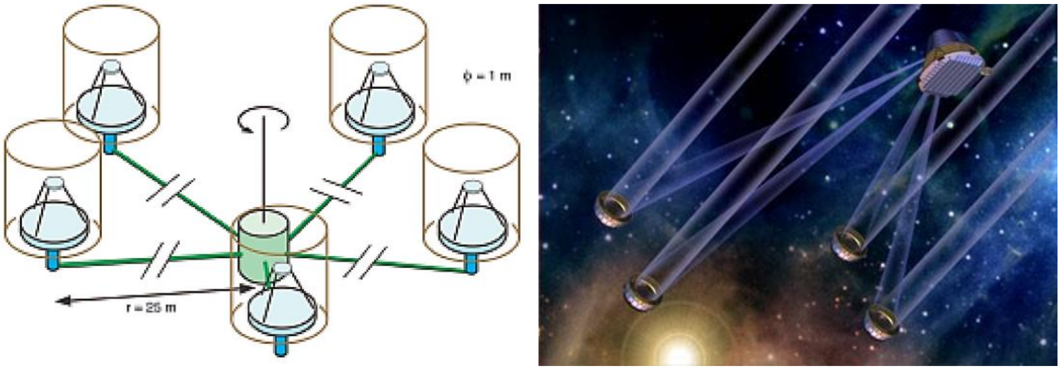

Fig. 1.8. ESA's Darwin mission. Left: layout of the six satellites for nulling interferometry. Right: artistic illustration of the cluster of the satellites.

Nulling interferometry puts stringent requirement of the relative positions of the formation flying satellites. The OPD between various beams have to be less than 10^{-3} of the wavelength. To achieve this, a local GPS system keeps the spacecraft within ten millimeters of their intended positions, while a laser metrology system measures their actual positions to within 5 nm.

1.1.4.2 Gravity Recovery and Climate Experiment (GRACE) and follow-on mission

The standard gravity is by definition 9.806 65 m/s^2, however, local gravity may vary due to tides, climate, earthquakes and more. The GRACE mission aims to measure the global gravity field distribution and its dynamic change. The main principle is to measure the relative distance variation between two satellites separated by 220 kilometers, as illustrated in Fig.

1.9. Launched in March of 2002, the GRACE mission is accurately mapping variations in Earth's gravity field. Due to its greatly success, a follow-on mission (GRACE-FO) has been launched in 2017, with an improvement distance measurement accuracy from some micrometers to tens of nanometers at 0.1 Hz.

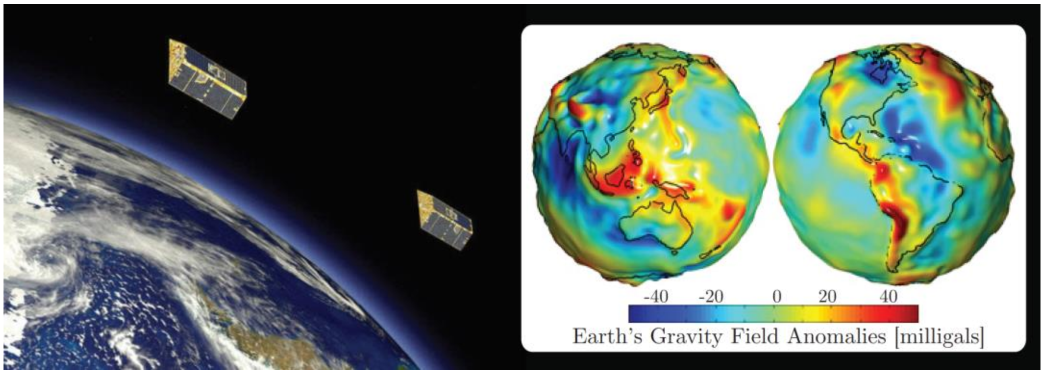

Fig. 1.9. Artist impression and the measured gravity field of GRACE.

The improvement was achieved by replacing the previous radio ranging by a laser ranging interferometer.

1.2. Review of Techniques for ADM

There are many methods to perform ADM with different measuring range and precision. In general, these methods can be classified into two categories: by measuring the time-of-flight (TOF) for the lightwave propagation through the original point to the target, or by measuring the relative phase of the light wave (interferometry). The first category includes pulsed TOF, in which short light pulses are sent to the target; amplitude modulated continuous wave (AMCW), in which the intensity of light is modulated sinusoidally; and frequency modulated continuous wave (FMCW), in which the frequency of lightwave is modulated quasi-linearly. The second category includes multiwavelength interferometry (MWI), frequency sweeping interferometry (FSI) and dispersive interferometry. All the methods required some kind of modulation of light, whether in amplitude, frequency and polarization. In the following, these methods are reviewed.

From the last decade, the concept of frequency comb generated from mode-locked femtosecond lasers has revolutionized the metrology. Not only the traditional distance measurement methods have been improved [13-19], but also some new strategies have been exploited [20-25]. This is, in frequency domain, due to that the frequency comb acts as a perfect frequency ruler that can be used to measure the optical frequency (and thus the wavelength) of a light source. A frequency comb comprises a large number of frequency components that are evenly spaced by the pulse repetition rate of the femtosecond laser f_r, and the absolute position of these frequency components can be well controlled and stabilized with the same precision of RF reference. On the other hand, in time domain, the pulses are highly coherent because the relative phase between the lightwave carrier and its envelope can be controlled. Thus, a small optical path difference (OPD) between two pulse trains causes a significant interference intensity change (cross-correlation function). With the assistance of a frequency comb in metrology system, the precision and non-ambiguous range can be improved. In the following review, the traditional methods are first introduced, and for each method, the integration of femtosecond laser frequency comb is introduced. In the last part of this ADM method review, the measurement methods that only based on frequency comb are introduced.

1.2.1 Pulsed Time-of-Flight

The most straightforward method to measure absolute distance is by sending light pulses and measuring the round-trip time for the pulses to travel between the light source and the target. The distance can be measured by multiplying the round-trip time and the speed of light. The working principle of ADM based on pulsed TOF is shown in Fig. 1.10.

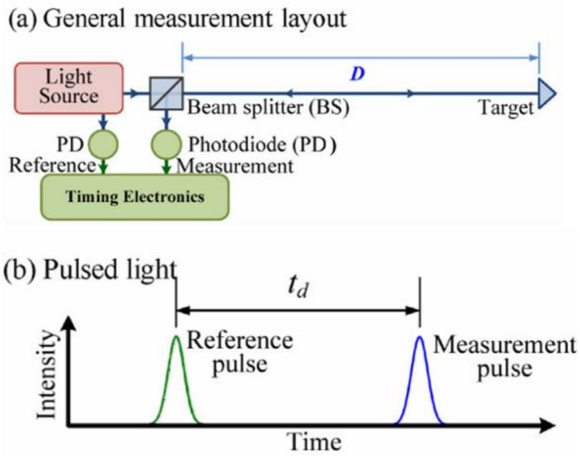

Fig. 1.10. Schematic of typical ADM system based on pulse TOF. (a). General measurement layout. The system includes a pulse light source and a timing electronics to record the time difference between output reference pulse and the reflected measurement pulse. (b). Illustration of the reference pulse and measurement pulse. After Ref. [4].

The distance between the measuring origin and the target is measured by multiplying the time interval between the reference and the target, and dividing by 2 to get the single-trip length:

$$D = \frac{1}{2n} c\Delta t \qquad \text{Eq. 1.1}$$

where n, c, and Δt are the refractive index, light speed in vacuum, and the round-trip time of the pulse, respectively. It is obvious that the distance measurement resolution using pulse TOF is limited by the resolution of the pulse's flight-time measurement. This is ultimately limited by the electronic response of the photodetection circuit and the delay characteristics of the electronics involved. For instance, if the flight time can be determined with a resolution of 1 ns, which corresponds to a bandwidth of 1 GHz of the photodetector, the distance can be determined with a resolution of 15 cm. For shorter distances in the order of a few hundred meter, a resolution of a few mm is achieved after averaging of the measurements. Therefore, this method is mostly applied in large distance measurement without high precision requirement, such as remote sensing.

An interesting advance for flight time determination has taken place using femtosecond pulse cross correlation detection [26]. The working principle is shown in Fig. 1.11.

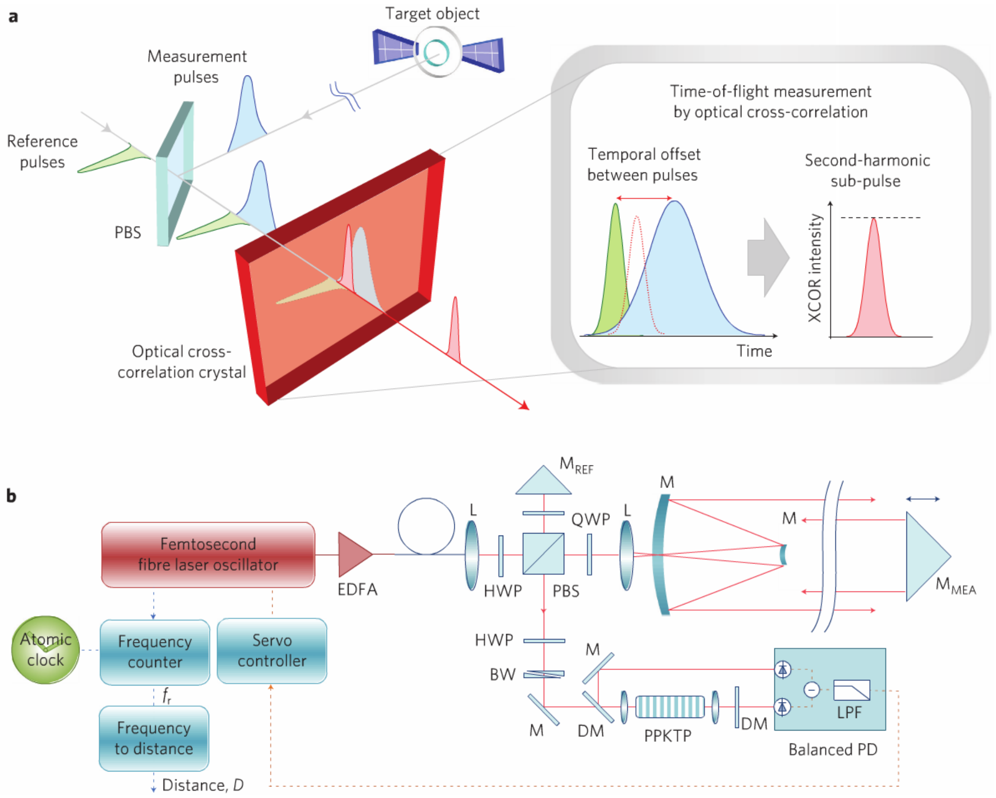

Fig. 1.11. Time-of-fight measurement of femtosecond light pulses. a. Timing of femtosecond pulses by means of optical cross-correlation. b. Hardware configuration. The PPKTP crystal produces the balanced cross-correlation (BCC) signal, which enables precise timing of the returning pulses with respect to the reference pulses. XCOR, cross-correlation. The pulse repetition rate is controlled to lock the BCC signal to its zero-crossing point. EDFA, erbium-doped fiber amplifier; L: lens; PBS:

polarization beamsplitter; HWP: half-wave plate; QWP: quarter-wave plate; M: mirror; MREF (MMEA), reference (target) mirror; PD: photodetector; BW: birefringent wedge; DM: dichroic mirror; f_r: pulse repetition rate. After Ref. [26].

Instead of measuring the TOF by direct intensity detection of the light pulse, the proposed method records the TOF by adjusting the repetition rate to ensure that the returning pulse is exactly overlapped with the reference pulse, thus the TOF is the exact integral times of the pulse separation. The error signal is offered by the balance cross-correlation signal, shown in Fig. 1.11(a). The precision depends on how accurately the locking control of f_r can be performed to achieve the zero-offset overlap between the reference and the measuring pulses. It enables a precision of $\pm 1\ nm$ in terms of Allan deviation at 1 second averaging time. This precise TOF determination is achieved by the unique characteristic of the high coherence of the femtosecond pulses, which ensures that the cross-correlation function is highly sensitive with respect to the spatial offset between the pulses.

1.2.2 Amplitude Modulation Continuous Wave (AMCW)

The pulse TOF is based on the direct light intensity measurement, which cannot resolve small distance difference. One mean to increase the measurement accuracy is through sinusoidally modulating the amplitude of the transmitted light beam and measure the phase difference between the transmitted and the reflected light. The working principle of AMCW is shown in Fig. 1.12.

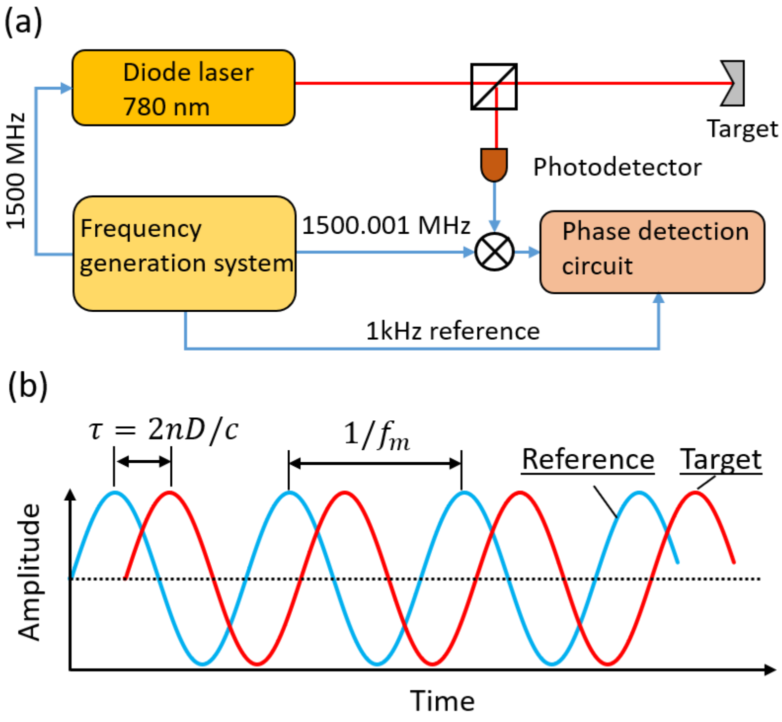

Fig. 1.12. Working principle of AMD based on AMCW. (a). Diagram of a typical AMD system based on AMCW. (b). Illustration of emitted and received signals. Adapted from Ref. [27].

The phase difference between the transmitted and received waveforms is:

$$\Delta\phi = 2\pi \frac{2nD}{c} f_m \qquad \text{Eq. 1.2}$$

where f_m is the modulation frequency and D is the single trip length of the unknown distance. The modulation wavelength equals to the propagation distance of the light within one period of modulation signal that is $\frac{c}{f_m}$. Thus, the non-unambiguous range of AMCW method is half of the modulation wavelength $NAR = \frac{c}{2f_m}$. It is preferable using lower modulation frequency in order to increase the non-ambiguous range. However, the measurement accuracy will degrade because the lower resolution of the phase measurement for a given SNR. By accurately measuring the phase, some range finders applying this method achieved a resolution of 100 µm. In Ref. [28] a distance resolution of a 1 µm at 5 m has been achieved with a modulation frequency of 28 GHz. This high modulation frequency is made possible by external modulation using an electro-optical modulator.

Interestingly, the femtosecond pulses from a mode-locked laser can be regarded as the superposition of many sinusoidal waves when we Fourier transform the time domain pulses. Different desired modulation frequency can be obtained through filtering. The work using femtosecond laser performing AMCW was carried out in 2000 by Minoshima *et al.*, shown as Fig. 1.13.

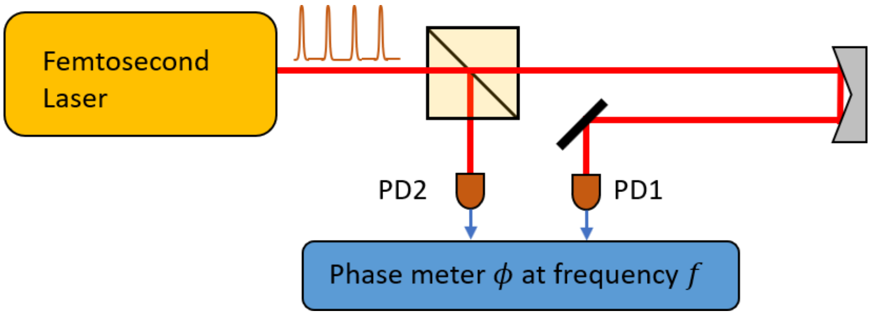

Fig. 1.13. Experimental setup for the high-accuracy distance meter with the intermode beats of a femtosecond mode-locked laser. Adapted from Ref. [18].

In fact, it was the first attempt using mode-locked femtosecond laser in distance measurement. This offers flexibility of generating different modulation frequencies with the harmonics of the repetition frequency ($f_r = 50\,\mathrm{MHz}$) of the femtosecond laser. In their experiment, the absolute mechanical distance of 240 m with 8 ppm accuracy was obtained, and it is possible to achieve higher resolution by use of higher frequency components.

1.2.3 Multi-Wavelength Interferometry (MWI)

To increase measuring NAR of traditional single wavelength interferometry, multi-wavelength interferometry can be used. Using two wavelengths λ_1 and λ_2, we can determine the distance with NAR of $\frac{\lambda_1\lambda_2}{2(\lambda_1-\lambda_2)}$. The mathematical model for obtaining absolute distance from the factional fringe of each wavelength interference signal is first discussed by Tilford in 1977 [29]. The fractional fringe of individual wavelength can be measured using super-heterodyne approach, as shown in Fig. 1.14.

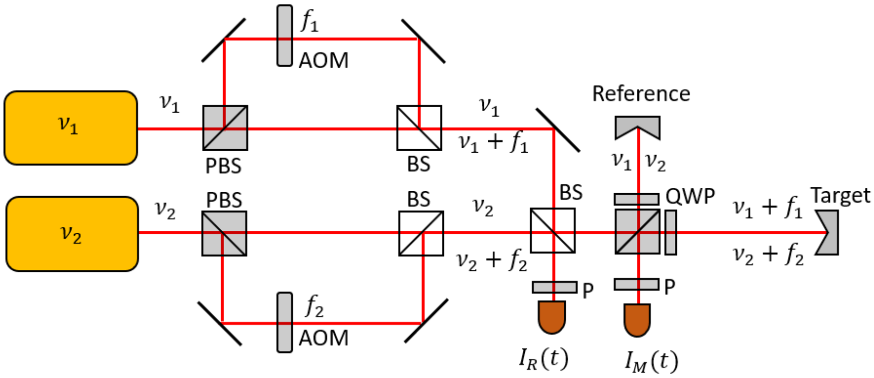

Fig. 1.14. Optical setup for two-wavelength super-heterodyne interferometry. AOM, acousto-optical modulators; P, Polarizer; QWP: quarter-wave plate. After Ref. [30].

For the measurement using each wavelength, the laser source is stabilized by a wavelength selecting and stabilization system working at single frequency. The fractional phase is obtained from the phase meter. The heterodyne signal on the reference photodetectors and the measurement interferometer system are:

$$\begin{gathered} I_R(t) = a_{0\mathrm{R}} + a_{1\mathrm{R}}\cos(2\pi\, f_1 t) + a_{2\mathrm{R}}\cos(2\pi\, f_2 t) \\ I_M(t) = a_{0\mathrm{M}} + a_{1\mathrm{M}}\cos(2\pi f_1 t + \phi_1) + a_{2\mathrm{M}}\cos(2\pi f_2 t + \phi_2) \end{gathered} \qquad \text{Eq. 1.3}$$

where $\phi_1 = \frac{4\pi(L\nu_1 - l\nu_1 + Lf_1)}{c}$ and $\phi_2 = \frac{4\pi(L\nu_2 - l\nu_2 + Lf_2)}{c}$, L and the l are the target arm and the reference arm of the measurement Michelson interferometer. We can see that both the reference signal and the measurement signal contain two shifted frequencies f_1 and f_2. Therefore, these two frequencies form beat signals. Supposed the phase of the reference beat signal is 0, then the phase of the measurement beat signal is:

$$\varphi = \phi_1 - \phi_2 = \frac{2\pi L}{c}\left(\frac{\nu_2 - \nu_1 + f_2 - f_1}{2}\right) + \frac{2\pi l}{c}(\nu_2 - \nu_1) \qquad \text{Eq. 1.4}$$

So, the distance can be obtained from the phase measurement. The above equation shows that the measurement resolution is proportional to the frequency difference between the lasers for heterodyning, which is $\nu_1 + f_1$ and $\nu_2 + f_2$. So, lasers with appropriate frequency difference should be used. In a work carried out by Lay *et al.* [31], a laser was phase-modulated with a 40 GHz integrated modulator, generating upper and lower side-bands. Different synthetic wavelengths can be obtained by changing the modulation frequency. By unevenly distributing the powers between the interference arm and the measurement arm, Phung *et al.* managed to perform two-wavelength interferometry combining an interferometric optical phase and the synthetic phase measurement of the distance [32].

In 2006, N. Schuhler *et al.* proposed two-wavelength ADM where the wavelengths were stabilized by a frequency comb, as shown in Fig. 1.15. The frequencies of the ECLD and the

Nd:YAG were phase locked to two different comb modes. This was done by heterodyning the two lasers to their nearest comb modes and locking the heterodyne signals to a 20 MHz reference signal. Hence, the synthetic wavelength is given by:

$$\Lambda_s = \frac{c}{\Delta\nu} = \frac{c}{Nf_r} \qquad \text{Eq. 1.5}$$

The exact number of comb line interval N between the two lasers were obtained by measuring the synthetic wavelength using a He-Ne interferometer. For stabilizing the frequency comb, the repetition frequency of the comb was phase locked to a 100 MHz reference frequency with uncertainty $< 10^{-11}$ by changing the pump power, and one of the comb lines was locked to the Nd:YAG laser by controlling the length of the cavity.

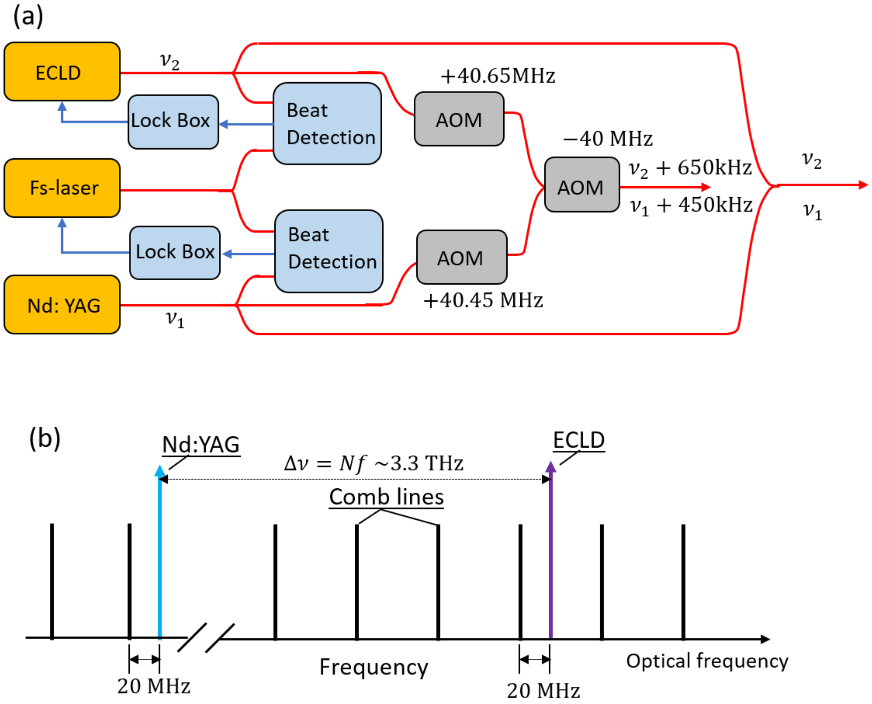

Fig. 1.15. Schematic of the two-wavelength light source referenced to the frequency comb. Adapted from Ref. [16].

In 2016, H. Wu *et al*. utilized the different comb lines of a frequency comb as the multi-wavelength light source [33]. A stabilized single mode c.w. laser, which is referenced to an optical cavity, is used as a tool to increase the power of comb line. Compared to Schuhler's work, only one c.w. laser is required. However, it requires the c.w. laser tuning to different comb lines, thus loses the measurement's parallelism. It reported that a measurement time of 15 minutes was required to perform single measurement, thus is not suitable for dynamic measurement. The schematic based on this concept is shown in Fig. 1.16.

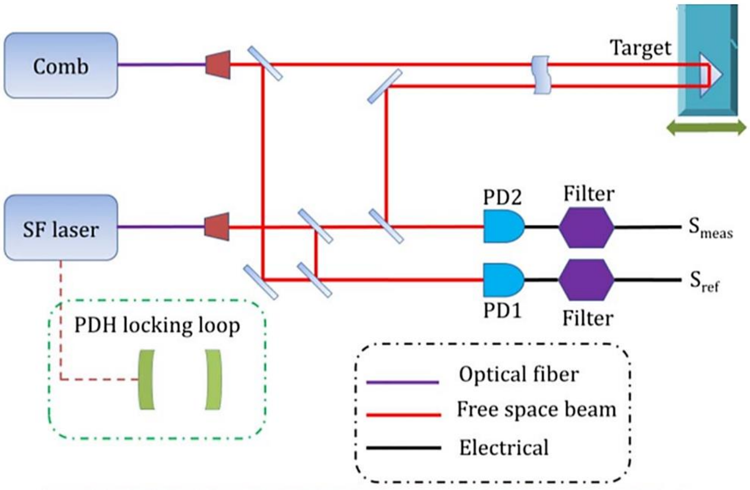

Fig. 1.16. Schematic of ADM system using frequency comb as light source to perform MWI. BS, beam splitter; PD, photodetector; S_{meas}, measurement signal; and S_{ref}, reference signal. SF: single frequency laser. After Ref. [33].

1.2.4 Frequency Sweeping Interferometry (FSI) and Frequency Modulation Continuous Wave (FMCW)

Instead of using multi-wavelength interferometry to increase the NAR, FSI and FMCW use frequency continuously-swept laser sources, as shown in Fig. 1.17. Because the different time delays between the reference arm and the target arm, the optical frequencies from these two paths on the photodetector are differentiated by $v_{SN}\Delta\tau$, where v_{SN} is the sweeping speed and $\Delta\tau$ is the time delay difference. Beat note is generated with a frequency equal to the optical frequency difference. The difference between FSI and FMCW lies in their difference of signal processing. For FMCW, as shown in Fig. 1.17(b), the distance information is retrieved by analyzing the frequencies of the beating signal. To correctly obtain the distance, the tuning laser source should sweep linearly, i.e., v_{SN} should be a constant. Whereas FSI obtains the distance by measuring phase change of beating signal and its corresponding frequency sweeping range.

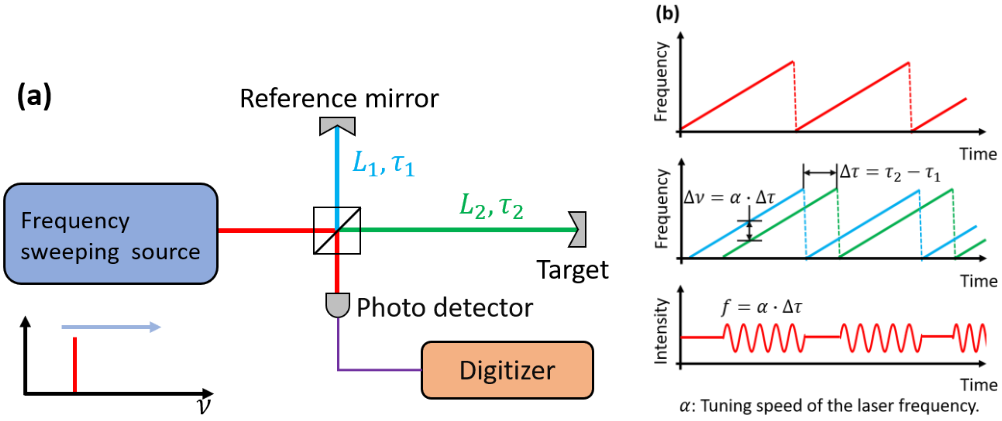

Fig. 1.17. Working principle of FMCW/FSI. (a). Schematic of FMCW/FSI system. (b). Illustration of the interference fringe and frequency tuning.

For wavelength λ, the absolute phase difference between the lightwave reflected from the two arms is $\phi = \frac{2\pi L}{\lambda} = \frac{2\pi L\nu}{c}$. So, when the laser tunes from ν_s to ν_e and the corresponding phase difference changes from ϕ_s to ϕ_e, the distance can be obtained according:

$$L = \frac{c}{2\pi}\frac{\Delta\phi}{\Delta\nu} \qquad \text{Eq. 1.6}$$

where $\Delta\phi = \phi_e - \phi_s$ and $\Delta\nu = \nu_e - \nu_s$. In 1983, Tansey *et al.* did the experiment of optical FSI using dye laser, with tuning range of 24 GHz [34]. It was not until the invention of widely tunable external tunable laser in 1982 that the optical FSI has been widely researched. In 1986 Kikuta used the tunable diode laser [35], of which the frequency is tuned by tuning the inject current, to perform the FSI. The tuning range is 0.05 nm at 800 nm (corresponding 23.4 GHz frequency tuning).

The main problem to solve in the preceding works, as well as in present works, was non-linear tuning speed of the tunable laser source (TLS). There are two methods for frequency tuning speed linearization, i.e. active or passive. For active linearization, the output frequency of the sweeping laser is actively controlled in a feedback loop [36, 37]. It is challenging at large tuning range and high sweeping rate because of rising excess laser noise [38] and rising required feed-back bandwidth. The passive one calibrates the instantaneous frequency of the tunable laser during frequency tuning simultaneously with the recording the interference signal from the measuring interferometer. Thus, the interference signal in time domain can be mapped correctly in frequency domain, and Fourier transform with respect to the frequency is performed. In reported works, to the best of my knowledge, the frequency calibration systems are based on the following three methods.

1.2.4.1 Reference Interferometer

In this method, an auxiliary interferometer which the length is known accurately is illuminated by the same tuning laser source. Since the beating frequencies of the FMCW is proportional to the OPD of interferometers, the distance of the measurement interferometer can be obtained by comparing the beating frequencies with the reference interferometer [39-42]. The reference interferometers should be remained stable and kept in isolated conditions. Even though, the stability is challenging to maintain ppm within a day [43].

1.2.4.2 Fabry-Perot Etalon

In some applications, a Fabry-Perrot etalon is used for frequency tuning range calibration [44], and the system is shown in Fig. 1.18. While the laser sweeps the frequency, the interferometer detector acquires the fringes and a Fabry-Perot interferometer measures the sweep range by counting the resonances of the cavity. The system accuracy depends on the precision of the interference fringe phase measurement, the accuracy of the free spectral range of the FP etalon, and fractional part of the resonance number counting, which is a function of the finesse of the reference interferometer. Such system has been successfully applied in the inter-satellite absolute distance metrology in ESA's DARWIN mission [45], in which three satellites fly together and form a large interferometer.

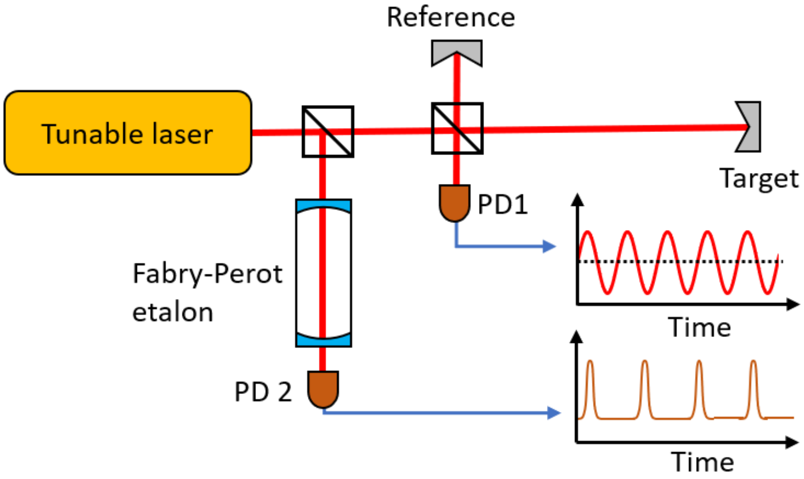

Fig. 1.18. The ADM system setup based on FSI. Adapted from Ref. [44].

1.2.4.3 Transition Lines of Molecules or Atoms

The frequency tuning range was calibrated using the molecular or atomic transition lines, because they are much stable frequency calibration source [46] and the transition lines are well calibrated in some standard metrology laboratories. A typical system used is shown in Fig. 1.19. A gas cell containing low pressure iodine molecule is used for saturation spectroscopy. In the work in 1998, Barwood *et al*. [47] used the similar system with the exception that an auxiliary diode laser was used to heterodyne with a swept laser for precise frequency measurement. Both the diode lasers tuned with the same approximately range of 7 THz. Then one diode laser was locked to the rubidium transition line, and the measuring one is locked to the end resonance of the etalon. The frequency difference is then measured by the beat detector. The proposed system offers THz tuning range and frequency tuning range uncertainty around 100 kHz, corresponding length measurement uncertainty of 2.4×10^{-8}. However, two tunable narrow linewidth lasers are required in such systems.

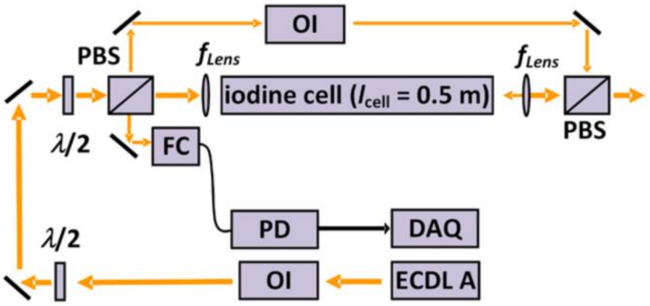

Fig. 1.19. Setup for high-resolution saturation spectroscopy. ECDL A, frequency-scanning external cavity diode laser; OI, optical isolator; FC, fiber coupler; PD, photo detector; λ/2, half-waveplate; PBS, polarizing beamsplitter; DAQ, data acquisition. After Ref. [48].

A comb-calibrated FMCW system has been proposed by Baumann *et al*. [14], the schematic of which is shown as Fig. 1.20. An optical in-phase/quadrature (IQ) allows the heterodyne signal between a tunable laser and a free-running comb be detected as well as the orthogonal version detects. After digitizing both the heterodyne signals, the instantaneous frequency was obtained by offline signal processing.

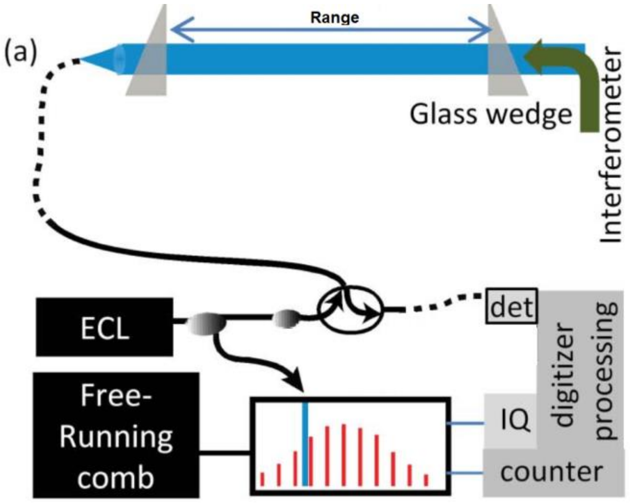

Fig. 1.20. Frequency linearization with a free-running comb in a FMCW system. ECL: external cavity laser. IQ: in-phase/quadrature detection. Det: photodetector. Interferometer shown in the figure is a displacement interferometer used for distance calibration. Adapted from Ref. [14].

1.2.5 ADM Based on Femtosecond Laser

The past decade saw a large number of applications using femtosecond pulse laser or the formed frequency comb in distance metrology. The application of femtosecond pulse laser and the formed frequency comb in ADM has the advantage of unique characteristics both in time and frequency domain. In time domain, the stable pulse train of intensity can be regarded the as the superposition of many intensity-modulated c.w. lasers that the modulation frequencies are the harmonic frequencies of the repetition rate of the femtosecond pulse laser. This provides a wide-range, high modulation frequency of AM light source that can be used in AMCW absolute distance measurement. This was first realized by Minoshima in 2000 [18] and has been introduced in section 1.2.2. Meanwhile, once the repetition rate and the carrier-envelope phase shift are stabilized, stable interference fringe can be built between pulses, and thus a small change of the overlap length between two pulses will cause significant intensity variation. By using cross-correlation technique, this provides a timing method in pulse TOF with high precision. This has been used by Lee *et al.* in 2009 [26] and has been introduced in section 1.2.1.

In frequency domain, the frequency comb is composed of a large number of frequency components that can be stabilized with high accuracy. This provides an elegant tool to measure and stabilize the laser frequencies that can be used in the distance measurement based on MWI and FMCW. This has been introduced in section 1.2.3 and section 1.2.4. In this section, the other methods using femtosecond laser that cannot be categorized in the above-mentioned classes are present.

For the application of the time domain characteristic of a femtosecond laser, J. Ye [49] firstly proposed a method of combing TOF measurement of femtosecond pulses and the interference measurement between these pulses. The working principle is shown in Fig. 1.21. The reflected pulses are detected by a fast detector for TOF measurement, and a cross-correlator to solve the interference fringes. The pulse number within the round-trip travel is determined by measuring the timing offsets correspond to two difference repetition rates. At the first repetition frequency, a timing offset of Δt_1 exists between the two pulse trains traveling through the different arms. When the repetition frequency increases to f_{r2}, pulses c' and d' move closer to a' and b', respectively, with a smaller timing offset of Δt_2. Hence, we have $\frac{2\Delta L}{c} = \frac{n}{f_1} - \Delta t_1 = \frac{n}{f_2} - \Delta t_2$, where c is the speed of light and n is an integer. We can uniquely determine the integer number n by measuring f_1, f_2, Δt_1 and Δt_2, leading to a preliminary estimate of distance to within millimeter uncertainty. Then, the repetition frequency is scanned until cross-correlation fringe can be observed, meaning that the pulses are overlapped. The repetition rate f_3, which produces the fringe that has the maximum envelope in cross-correlation fringe, means the pulses are completely overlapped, and the distance is determined as $\Delta L = \frac{nc\tau_3}{2}$.

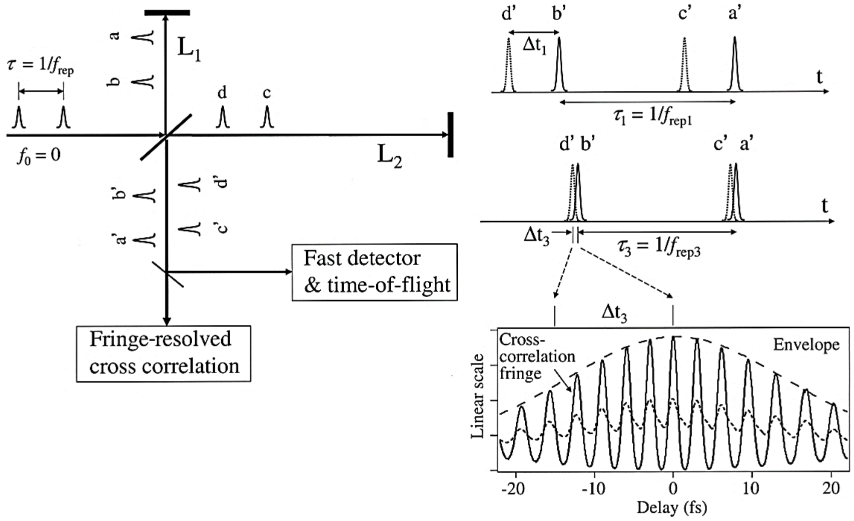

Fig. 1.21. Schematic of ADM combining TOF and interference detection. After Ref. [49].

In 2008, M. Cui *et al.* [50] verified the working principle experimentally by tuning the delay line to introduce the overlap length between the pulses. In 2009, I. Coddington *et al.* [24] realized the optical sampling using two femtosecond lasers that the repetition frequency is slightly different. As for in frequency domain, the dispersive interferometry using frequency comb was studied. Using virtually imaged phase array (VIPA) etalon, the comb lines are resolved in an imaging array [23]. A review of comb-based dimensional metrology can be found in Ref. [51].

1.3. Conclusion

In this chapter, we have reviewed the applications as well as the existing and emerging techniques for absolute distance measurement. Some universal ranging products such as LiDAR and laser trackers can be used in a wide range of applications, such as automatic driving and large-scale assembly in industrial sector. There are many cases where only specific measuring systems can be applied, especially in space missions. In summary, the presented ADM methods can be classified into two categories, i.e., measuring the time-of-flight and the lightwave interference. The former requires the light to be amplitude or frequency modulated so that one can determine the time when the lightwave has been sent and received. Techniques including the pulsed TOF, AMCW and FSI can be categorized into this principle. For the interferometry approach, we have multi-wavelength and dispersive interferometry. From this chapter, we find how the frequency comb impacts on the distance metrology thanks to its highly stable pulses in temporal domain and the large number of evenly spaced comb lines. Indeed, for the past decades, not only the existing distance measurement techniques have been improved, but also new measurement concepts have been proposed based on combs that have higher precision and allow for longer distance measurement. In this thesis, we introduce a frequency comb in the ADM system applying frequency sweeping interferometry. Unlike previous works, where static lasers are locked to the comb, the strategy in the present work will be calibrating the instantaneous frequency tuning range of the sweeping laser with a frequency comb.

Chapter 2. Comb-Referenced Frequency Sweeping Interferometry

In this chapter, the theoretical backgrounds of frequency sweeping interferometry (FSI) and frequency comb are introduced. We start from the basic concept of laser interferometry followed by an introduction on how to use FSI to measure absolute distance. Some considerations relating to the FSI technique will be presented. The schematic of using the optical frequency comb for calibrating the tuning range of the sweeping laser will be introduced.

2.1. Frequency Sweeping Interferometry

Fig. 2.1 shows the interferometry of lightwave from a Michelson type interferometer. A beamsplitter divides the input light into two parts that have different amplitudes but the same initial phases. One of them is directed to a reference mirror M_1 and the other beam is directed to the measurement mirror M_2. After been reflected by the two mirrors, the laser beams are combined again in the beamsplitter, where the two beams interfere.

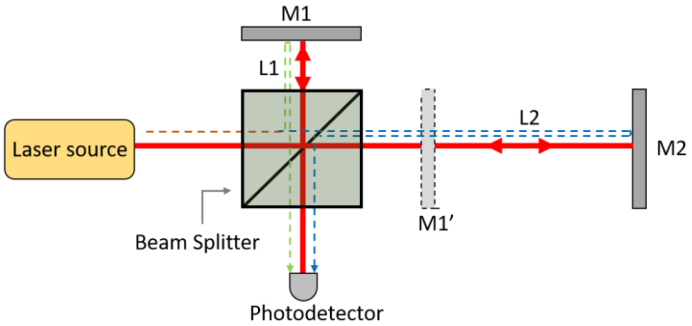

Fig. 2.1. Illustration of Michelson type interferometer. Red solid lines: laser beam. Green and blue dashed lines: light paths of the reference and the measurement. M1, M2: mirrors; L1 and L2: light paths.

For a single frequency laser, the electric field at position $\boldsymbol{r}$ can be written as:

$$E(t) = E_0 \sin(2\pi\nu_0 t - \boldsymbol{k}\cdot\boldsymbol{r} + \phi_0) \quad \text{Eq. 2.1}$$

where E_0 is the amplitude, $\boldsymbol{k}$ is the wave vector and ϕ_0 is the initial optical phase of the laser source at position $\boldsymbol{r}$. In the application of frequency sweeping interferometry (FSI), we are mainly interested in the temporal coherence of the lightwave. The spatial interference of light should be considered when detecting a diffusing surface, where the roughness of the surface will produce speckle noise [52]. In the present work, both the target and reference reflectors of the interferometer are retroreflectors (RRs), which means specular reflection. The spatial interference is also considered in the section 3.1.2, where the alignment of the laser beams for heterodyne detection is analyzed. In this section, we assume that light field is uniform in space in the following analysis. For simplicity of expression, the Eq. 2.1 can be written in complex function form as:

$$E(\mathrm{t}) = E_0 \cdot \exp[i\phi(t)] \qquad \text{Eq. 2.2}$$

where $\phi(t) = 2\pi\nu_0 t + \phi_0$ is the optical phase and the spatial dependence term $\boldsymbol{k} \cdot \boldsymbol{r}$ has been ignored. The instantaneous frequency of this optical field is:

$$\nu(t) = \frac{1}{2\pi}\frac{d\phi(t)}{dt} \qquad \text{Eq. 2.3}$$

For non-dispersive medium, where the phase speed of the lightwave is independent on the frequency, the electric fields of the light reflected from M_1 and M_2 are time-delayed versions of the light source that can be written as:

$$\begin{aligned} E_1(\mathrm{t}) &= E_{01} \cdot \exp\left[\phi\left(t - \frac{L_1}{c}\right)\right] \\ E_2(\mathrm{t}) &= E_{02} \cdot \exp\left[\phi\left(t - \frac{L_2}{c}\right)\right] \end{aligned} \qquad \text{Eq. 2.4}$$

Here $E_{01}$and E_{02} are the amplitude of the electrical fields, c is the speed of light in vacuum, L_1 and L_2 are the optical path lengths of the two arms, which are reflected to the distances D_1 and D_2 between mirrors M1, M2 and beam splitters, as:

$$L_i = 2nD_i, i = 1,2 \qquad \text{Eq. 2.5}$$

where n is the refractive index of the medium. Assume that the polarization of these two electrical fields are parallel, the combined electric field can be written as:

$$E(t) = E_1(t) + E_2(t) \qquad \text{Eq. 2.6}$$

The interference signal detected by the square-law photodetector can be written as:

$$i(t) = RE(t)E^*(t) \qquad \text{Eq. 2.7}$$

$$= RA_1^2 + RA_2^2 + 2RA_1A_2\cos\left[\phi\left(t - \frac{L_1}{c}\right) - \phi\left(t - \frac{L_2}{c}\right)\right]$$

For conventional optical interferometry, the light source is a single fixed frequency laser and the phase can be written as $\phi(t) = 2\pi v_0 t$, where v_0, the optical frequency, is a constant. Substituting to Eq. 2.7, we get:

$$i(t) = RE_{01}^2 + RAE_{02}^2 + 2RE_{01}E_{02}\cos\left(2\pi\frac{v_0}{c}L\right)$$

$$= R_P\left[P_1 + P_2 + 2\sqrt{P_1P_2}\cos\left(2\pi\frac{v_0}{c}L\right)\right] \qquad \text{Eq. 2.8}$$

where P_1 and P_2 are the optical power, R_P is the power-to-current responsivity of the photodetector, and $L = L_2 - L_1$ is the optical path difference (OPD) between the two arms. In displacement measurement, the change in the geometrical distance, and thus the OPD L, causes the photocurrent changes.

In absolute distance measurement using FSI, the distance keeps static, while the frequency of the laser source sweeps. Suppose the frequency is tuned linearly, so that it can be expressed as:

$$v(t) = v_0 + v_S t \qquad \text{Eq. 2.9}$$

where v_S is the frequency tuning speed in Hertz per second (Hz/s). According to Eq. 2.3, the optical phase can be written as:

$$\phi(t) = 2\pi\left(v_0 + \frac{1}{2}v_S t\right)t \qquad \text{Eq. 2.10}$$

Substituting in Eq. 2.7, we obtain the photocurrent of the interference signal as:

$$i(t) = R_P\left[P_1 + P_2 + 2\sqrt{P_1P_2}\cos\left(2\pi\frac{L}{c}v_S t + \phi_0\right)\right] \qquad \text{Eq. 2.11}$$

The above equation shows that when the laser source is tuned with a constant frequency tuning speed v_S, the photocurrent is a beat signal where the beat frequency is:

$$f_b = \frac{L}{c}v_S \qquad \text{Eq. 2.12}$$

The frequency is proportional to the round-trip path length difference and the tuning speed. In practice, the lasers can only be tuned quasi-linearly, which will change the beating frequency. As a result, the spectrum of the interference signal would be spread. The effect of nonlinear tuning has been studied in Ref. [53, 54]. In the work of [53], the nonlinear tuning could be modeled as the summation of a series of polynomials. It pointed out that the spectrum of the interference signal becomes asymmetrical and a large error is introduced. In the work of [54], which used the same tunable laser source as the present work, showed out that the nonlinear tuning can be modeled as the summation of some sinusoidal functions. It turned out that good results can be achieved when the tuning nonlinearity was sinusoidal.

The derivation of Eq. 2.11 in the early works of frequency sweeping interferometry, such as [35, 53, 54], was commonly implemented using the wavelength instead of frequency as the variable. Because at the beginning of optical FSI, the tunable laser sources were laser diodes that were tuned by changing the injection current. It is assumed that it was the wavelength that has a linear function of the injection current. The wavelength tuning range was only a few nanometers, corresponding to hundreds of gigahertz frequency change in 1550 nm. Therefore, first order of the Taylor expansion of the wavelength tuning was responsible for the distance measurement. The Eq. 2.11 can be expressed using the wavelength as variable as:

$$\begin{aligned} i(t) &= R_P\left[P_1 + P_2 + 2\sqrt{P_1P_2}\cos\left(2\pi\frac{L}{\lambda_0 + v_{S_\lambda}t} + \phi_0\right)\right] \\ &\cong R_P\left[P_1 + P_2 + 2\sqrt{P_1P_2}\cos\left(-2\pi\frac{L}{\lambda_0^2}v_{S_\lambda}t + \frac{2\pi L}{\lambda_0} + \phi_0\right)\right] \end{aligned} \qquad \text{Eq. 2.13}$$

where v_{S_λ} is the wavelength tuning speed. The approximately equal sign in the above equation is used because we ignore the higher orders of the Taylor expansion. Nowadays, the tuning range of an ECLD can be tens of nanometers without mode-hopping, so that the higher orders cannot be neglected.

In this thesis, we consider Eq. 2.11, which uses the frequency as the variable. Not only a long tuning range is used, but also the instantaneous frequency is calibrated using a frequency comb, which the comb lines are evenly spaced in frequency domain.

Instead of measuring the beat frequency, we can also obtain the distance from the following equation. The phase change of the beat signal is proportional to the frequency tuning amount according to Eq. 2.7 as:

$$\Delta\varphi = \frac{2\pi L}{c}\Delta\nu \qquad \text{Eq. 2.14}$$

It means that the distance can be obtained by knowing the phase change of the interference signal using a fringe counting and the corresponding optical frequency tuning range, without strict requirement of the linear tuning by:

$$L = \frac{c}{2\pi}\frac{\Delta\varphi}{\Delta\nu} \qquad \text{Eq. 2.15}$$

However, it does introduce error if highly nonlinear chirp is applied to the tuning laser source according to the analysis in Appendix A.

The following section introduces the above-mentioned methods for distance retrieving.

2.2. Signal Processing Methods for Distance Retrieving

From the basic equations of frequency sweeping interferometry Eq. 2.12 and Eq. 2.14, the distance can be retrieved from either the following two methods.

2.2.1 Distance Retrieving by Fourier Transform

The beat frequency of the interferometer Eq. 2.12 is proportional to the sweeping speed of the tunable laser and the distance. Spectrum analysis methods, such as Fourier transform, can thus be used to access the distance [42]. It is similar to the technique called optical frequency domain reflectometry (OFDR) in fiber systems to determine the location of failure in the fiber communication network [55]. Considering the tuning speed of the laser source $v_S(t)$ varies with time, a reference interferometer with known OPD can be used such that the distance under measurement can be obtained using:

$$L = \frac{f_s(t)}{f_R(t)} L_R \qquad \text{Eq. 2.16}$$

where $f_S(t)$ and $f_R(t)$ are the instantaneous frequencies of the measuring signal and the reference beat signal; L_R is the OPD of the reference interferometer. In addition, the measurement resolution and precision with different types of filtering window, i.e. apodization functions, used for the fast Fourier transform has been analyzed in Ref. [53]. It pointed out that with perfect linear tuning and low amplitude and frequency noises, Blackman filtering window gives the highest resolution compared to Hanning or Gaussian windows. As the noises increase, Blackman and Hanning windows produce equivalent precisions, and the Gaussian window was found to produce best precision.

2.2.2 Distance Retrieving by Fringe Counting

The fringe counting method can date back to the early age of Michelson-Morley experiment, in which the phase was estimated visually [56, 57]. With the application of lasers in dimensional metrology, it has been widely applied in displacement measurements [58]. For the absolute distance measurement, this method can be applied according to Eq. 2.14, which states that the phase of the interference signal is proportional to the instantaneous optical frequency shift and to the round-trip path length distance. Modern fringe counting systems rely on electronic detection and signal processing to evaluate the fractional phase with higher precision [59].

Fractional phases of the fringe can be measured by implementing, for example, four detectors in quadrature on the interferometers as shown in Fig. 2.2, which can be used to get down below to the quarter of a fringe [60, 61]. It is capable of real-time measurement of the instantaneous phase of the interference fringe. A heterodyne detecting approach has also been proposed by Stone *et al*. for fringe counting [43]. Signal processing approach deals with sampled fringe data to obtain phase information. In summary, the fringe counting can be implemented using the techniques shown in Fig. 2.2.

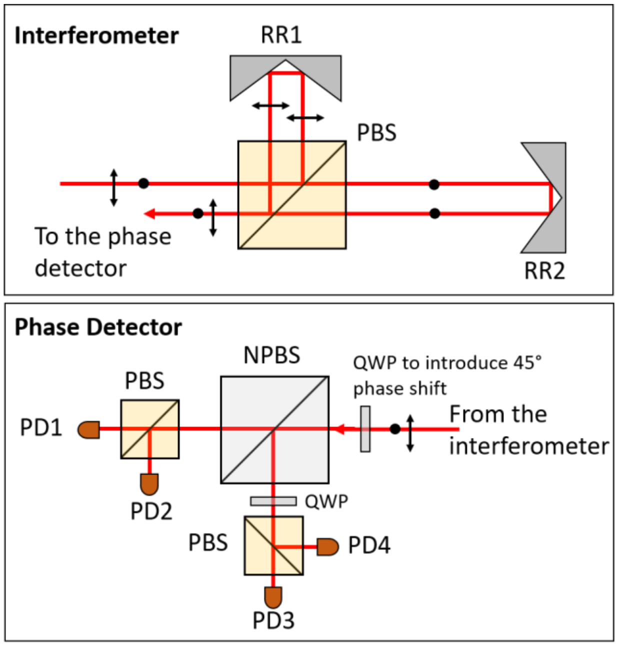

Fig. 2.2. Phase detection methods with four detectors in quadrature detection. RR: retroreflector. PD: photodetector. PBS: polarized beamsplitter. NPBS: non- polarized beamsplitter. QWP: quarter-wave plate.

High distance resolution can be obtained using fringe counting method. The main limitation of this method is that it cannot measure multiple targets, in which the interference signals overlap together.

Note that the integer part of the fringe can always be measured without error, the uncertainty related to this approach can be derived from Eq. 2.15 as:

$$\delta L = \sqrt{\left(\frac{c}{2\pi}\frac{\delta\varepsilon}{\Delta\nu}\right)^2 + \left(\frac{\delta\Delta\nu}{\Delta\nu}\cdot L\right)^2} \qquad \text{Eq. 2.17}$$

where $\delta\varepsilon$ and $\delta\Delta\nu$ are the measurement uncertainty the fractional phase and the frequency tuning range respectively. In terms of relative uncertainty, Eq. 2.17 can be written as:

$$\sigma L = \frac{\delta L}{L} = \sqrt{\left(\frac{c}{2\pi L}\frac{\delta\varepsilon}{\Delta\nu}\right)^2 + \left(\frac{\delta\Delta\nu}{\Delta\nu}\right)^2} \qquad \text{Eq. 2.18}$$

Two points should be noted from this equation. Firstly, the measurement uncertainty will be improved with larger tuning range if the other condition is the same. Secondly, the relative uncertainty introduced by the frequency tuning range uncertainty does not depend on the measured distance, while the fractional phase uncertainty has minor effect on the uncertainty budget for large distance where the uncertainty of frequency tuning range measurement dominates.

In summary, there are two distance retrieving methods of frequency sweeping interferometry: by analyzing the spectrum of the interference beat signal or by measuring the phase change and the sweeping range. Due to nonlinear tuning behavior of practical tunable lasers, as one will see in Chapter 5, the instantaneous frequency of the tunable laser should be obtained along with the beating interference signal (Eq. 2.11). In this thesis, instantaneous frequency of the tunable laser is measured by a frequency comb.

2.3. Several Considerations of FSI

In this section, some unique and important factors affecting the measurement accuracy for FSI, including the distance drift amplification and chromatic dispersion effect, are considered.

2.3.1 Amplification Factor of Distance Drift

The effect of distance drift during the frequency scanning process depends on how the signal is processed. Here we analyze the effect based on the fringe counting method. If the OPD changes from L_s to L_e during the tuning range from frequency of start ν_s to the frequency of end of tuning ν_e, the phase change of the beating signal is:

$$\Delta\varphi = \frac{2\pi}{c}(L_e\nu_e - L_s\nu_s) \qquad \text{Eq. 2.19}$$

By substituting $L_s = \frac{L_e+L_s}{2} + \frac{L_e-L_s}{2}$ and $L_e = \frac{L_e+L_s}{2} - \frac{L_e-L_s}{2}$, Eq. 2.19 can be written as:

$$\Delta\varphi = \frac{2\pi}{c}(\bar{L}\Delta\nu + \Delta L\bar{\nu}) \qquad \text{Eq. 2.20}$$

where $\overline{L}$, $\bar{\nu}$, ΔL and $\Delta\nu$ are the average and difference OPD and frequency, which are defined as follow:

$$\begin{cases} \overline{L} = \dfrac{L_s + L_e}{2} \\ \bar{\nu} = \dfrac{\nu_s + \nu_e}{2} \\ \Delta L = L_e - L_s \\ \Delta\nu = \nu_e - \nu_s \end{cases} \qquad \text{Eq. 2.21}$$

So, the retrieved distance using Eq. 2.15 is:

$$L_{meas} = \overline{L} + \Delta L \cdot \frac{\bar{\nu}}{\Delta\nu} \qquad \text{Eq. 2.22}$$

It can be seen that the distance change during frequency tuning is amplified by $\frac{\bar{\nu}}{\Delta\nu}$. This means that the FSI is sensitive to the distance drift, making it cannot be applied directly to measure dynamic distances. Some methods, such as using two sweeping lasers where the tuning direction is in opposite [10, 39, 62, 63] and using sub-measurement as presented in 5.4 can fix this problem.

2.3.2 Refractive Index of Media

The refractive index of media has two-fold effects on the geometrical distance determination: refractive index compensation and chromatic dispersion due to frequency tuning. The OPD, L, is related to the geometric distance D by:

$$L = 2nD \qquad \text{Eq. 2.23}$$

where n is the phase refractive index. When the medium is air, the refractive index is determined mainly by the temperature, pressure, relative humidity and the content of carbon dioxide. One part per billion of refractive index change may be induced by any of the following change [64]:

- 1°C change of air temperature;
- 333.3 Pa (2.5 mm mercury) change of air pressure;
- 80% change of relative humidity.

So that the air condition should be monitored for compensating the measured OPD and some empirical equations can be used to calculate the refractive index, such as the Ciddor equation in Ref.[64] and the modified Edlén equation in Ref. [65].

On the other hand, the equations Eq. 2.12 and Eq. 2.14 assume that the refractive index is constant during tuning, which is not the case in practice due to the chromatic dispersion of the media along the measuring path. When the refractive index is taken into accounts, Eq. 2.14 can be rewritten as:

$$\Delta\varphi = \frac{4\pi D}{c}\Delta(n\nu) \qquad \text{Eq. 2.24}$$

The measured distance from Eq. 2.15 is:

$$L_{meas} = \frac{c}{2\pi}\frac{\Delta\varphi}{\Delta\nu} = 2D \cdot \frac{n(\nu_e)\nu_e - n(\nu_s)\nu_s}{\Delta\nu} \qquad \text{Eq. 2.25}$$

where ν_s, ν_e, $n(\nu_s)$ and $n(\nu_e)$ are the optical frequencies of start and the end of tuning and the corresponding refractive index. It can be verified that the effect of chromatic dispersion is similar to the distance drift model described in section 2.3.1, in which is the OPD is changed from $2n(\nu_s)D$ to $2n(\nu_e)D$. It means that the error of the measured distance will be $\frac{2[n(\nu_e)-n(\nu_s)]D\bar{\nu}}{\Delta\nu}$ if the chromatic dispersion is not taken into account.

The refractive index of dry air, at temperature 15 °C, pressure 101325 Pa, and 450 ppm CO_2 content, in the visible and near infrared region can be expressed as [64]:

$$n(\lambda) = 1 + \frac{0.05792105}{238.0185 - \lambda^{-2}} + \frac{0.00167917}{57.362 - \lambda^{-2}} \qquad \text{Eq. 2.26}$$

where λ is the wavelength in µm. For comparison, the refractive index of Corning® SMF-28 is [66, 67]:

$$n(\lambda) = N(\lambda_0) + \frac{c}{8}S_0\left(-\lambda^2 + \frac{\lambda_0^4}{3\lambda^2} - 2\lambda_0^2\right) \qquad \text{Eq. 2.27}$$

where $\lambda_0 = 1310\,nm$ is the zero-dispersion wavelength, $N(\lambda_0) = 1.4677$ is the group refractive index at λ_0 and $S_0 = 0.092\frac{ps}{nm^2 \cdot km}$ is the zero dispersion slope. The following figure shows the errors induced by the chromatic dispersion of air and SMF-28 fiber.

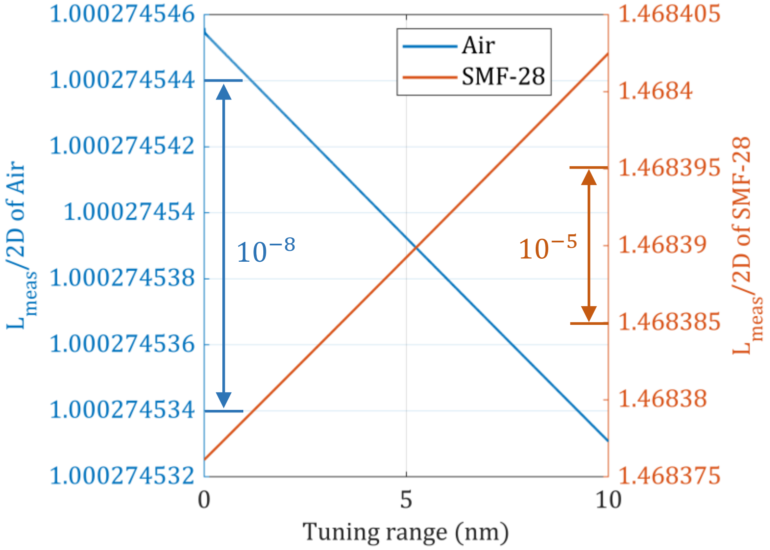

Fig. 2.3. Ratio between the measured OPD and the round-trip geometric length of air (T=15 °C, P=101 325 Pa, relative humidity = 0% and 450 ppm CO2) and SMF-28 fiber.

It can be seen that the errors in a fiber are more severely affected than in open air systems considering the higher chromatic dispersion. As calculated, the error is 1.3×10^{-6} for air and 20×10^{-3} for SMF-28, if the tuning range is 10 nm. If one uses a fiber interferometer as the reference interferometer, one should be careful on this point [48, 68, 69].

2.4. Frequency Calibration Using Frequency Comb

To linearize the tuning speed of the tunable laser, a frequency comb is introduced in the FSI system. The schematic of the proposed ADM system is illustrated in Fig. 2.4. An external cavity laser diode (ECLD, HP 81682A) that can be tuned continuously without mode-hopping from 1460 nm to 1580 nm served as the measuring light source. The linewidth of the laser is around 100 kHz. The tuning speed can be switched within 5 nm/s, 10 nm/s, 20 nm/s and 40 nm/s. A minor portion power of the ECLD was introduced to the distance measuring interferometer by a 90:10 fiber coupler, and the major portion of power was heterodyned with the frequency comb. The frequency comb (FemtoFiber FFS, Toptica Photonics) is an erbium-doped femtosecond fiber laser around 1550 nm wavelength, with repetition rate of about 76 MHz. The output from the frequency comb was filtered by an optical filter of bandwidth 8 nm to avoid undesired power generated by the frequency teeth that are outside of the tuning range.

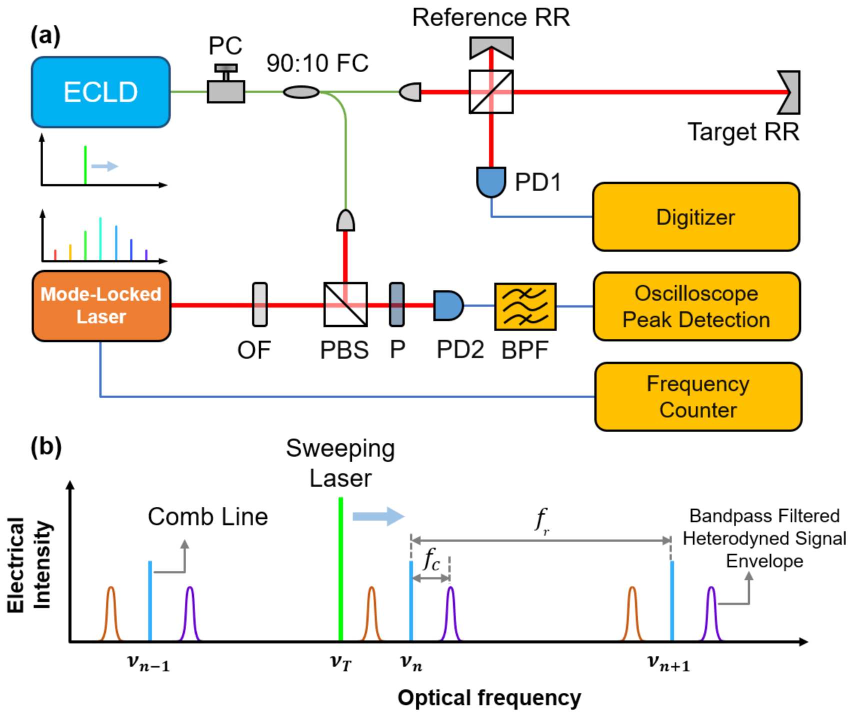

Fig. 2.4. (a). Experimental setup of the proposed ADM system. The tunable external cavity laser diode laser (ECLD) is quasi-linearly swept and is sent to the Michelson interferometer and to heterodyne with a frequency comb, which is formed by mode-locked laser. PD1 and PD2: photodetectors. PC: polarization controller. FC: fiber coupler. RR: retro-reflector. OF: optical filter. P: polarizer. PBS: polarized beam splitter. BPF: bandpass filter. (b). Illustration of the comb line, the sweeping laser and the filtered heterodyne signal envelope. Envelopes with orange color denote the peak is formed by filtering the heterodyne signal when the sweeping laser is approaching the comb line and the purple ones denote the sweeping laser is leaving the comb line. f_r: repetition rate of the comb. : central frequency of the BPF.

The heterodyne signal between the ECLD and the femtosecond laser frequency comb composed the beating signal between the ECLD and near comb lines as well as the beating signal between the comb lines (this will be explain in detail in section 3.1). We are interested in the beating signal between the ECLD and the nearest comb line, because it gives us the information of frequency position of the ECLD. We use a bandpass filter (BPF) to eliminate the high frequency components. Using a bandpass filter has following advantages:

1. An increased SNR of the heterodyne signal detection. The noise power caused by thermal effect and shot noise of the photodetection is proportional to the bandwidth of the detection circuit, so that narrow bandpass filter can effectively limit the noise.
2. Calibration peak signals are generated when the frequency of the heterodyne signal is within the passband of the BPF, as shown in Fig. 2.4(b). Two calibration peak

signals are generated when the tunable laser sweeps across each comb line, which correspond the instantaneous frequency of the tunable laser equaling to:

$$\nu_T = \nu_n \pm \mathrm{F}_{cf} \qquad \text{Eq. 2.28}$$

where ν_n and F_{cf} are the optical frequency of the nearest comb line and the central frequency of the BPF. Using these calibration signals allows us performing sub-measurements describing below, which improves precision within single full-sweep.

3. The calibration peaks signals, which are evenly spaced by f_r, can be used as the triggering signal to sample the interference beat signal. The interference beat signal is then sampled uniformly in the optical frequency domain, therefore corrects the nonlinear sweeping behavior of the tunable laser.

In this thesis, the sub-measurement approach is presented. From the basic equation of frequency sweeping interferometry Eq. 2.14, the distance can be obtained by knowing the frequency tuning range and its corresponding phase shift. As illustrated in Fig. 2.5, any two of calibration peaks can be used to calculate the distance. We call it 'sub-measurement' since it performs distance measurement within a single sweeping.

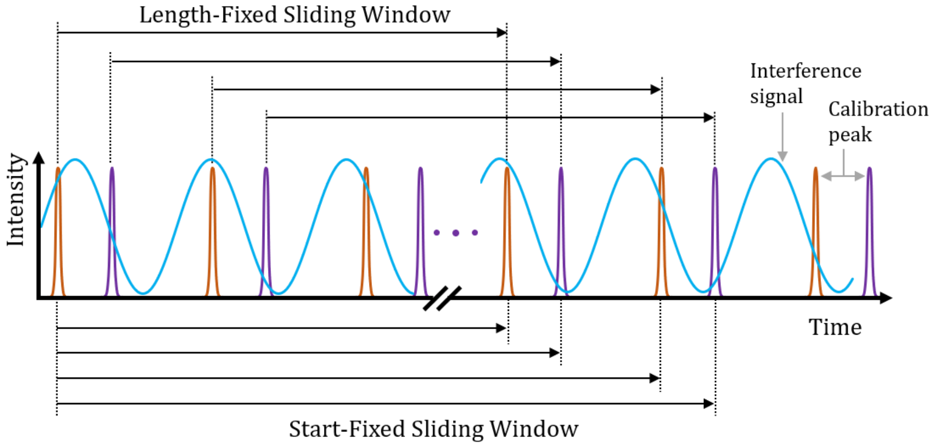

Fig. 2.5. Schematic of sub-measurement in a single sweeping. Blue curve: interference signal. Orange peaks: envelope of the filtered heterodyne signal. One full scan was divided into several sub-sections. The length-fixed sliding window was used for averaging the ADM results. The Start-fixed sliding window was used for vibration measurement.

Two types of sub-measurements were performed. The first one adopted length-fixed sliding window, in which two adjacent sub-measurements are performed in windows where both the start and end peaks are shifted by one peak. Without true distance change between these sub-measurements, their result reflected the same distance. By averaging the results, the accuracy can be improved as averaging the results of multiple sweepings, but faster.

Averaging the sub-measurements increases the resolution only if the sub-measurements are decorrelated. This is the case in our system because the phase noise of the frequency comb is arbitrary. If the envelop frequency or the repetition rate of the femtosecond laser is stabilized this point has to be reconsidered.

The second type of sub-measurement adopted start-fixed sliding window, in which all the sub-measurements have the same start peak and the end peak between two adjacent measurement are shifted by one. The distance change between the sub-measurement can be observed using this method. In this thesis, the vibration of the target has been measured, as detailed in section 5.3.1.

2.5. Optical Frequency Comb

2.5.1 Principle of Frequency Comb Generation

The concept of frequency comb was first given to the frequency structure of phase modulated cw lasers, in which dozens of sideband frequencies with equal intervals were generated [70, 71]. This happened in early 1990s and people then found that the span of the comb is related to the pulse width. Even though it was later found that placing the modulator inside in the laser resonant cavity would increase the span of sidebands, the purpose of these early devices was to improve the temporal characteristics of pulsed lasers, such as to increase the repetition rate and shorter pulses [72]. With the development of ultrafast lasers, especially the development of titanium-doped sapphire laser and Kerr-lens mode locking in 1990s, the pulse width reached down to ~100 fs. At this point, a comb with hundreds of THz was ready for direct optical frequency measurement. Additionally, octave-span comb was generated with supercontinuum generation that allows for self-referencing to measure the offset frequency. Today, the frequency of the comb lines can be stabilized with sub-Hz linewidth [73]. New combs such as Erbium doped fibers laser and microcavity combs [74] have been developed. Because of the simplicity, efficiency and high precision compared to the traditional frequency train, the metrology of the optical frequency are available to performed in laboratories worldwide. In the following section, the generation of frequency comb from a mode-locked laser is introduced.

2.5.2 Mode-Locked Femtosecond Frequency Comb

Fig. 2.6 illustrates a mode-locked femtosecond laser in time and frequency domain. Mode-locked lasers generate short optical pulses by establishing a fixed phase relationship between all the lasing longitudinal modes. To start, we ignore the carrier-envelope phase and assume identical pulses, i.e., ϕ_{ce} is a constant. If we just consider a single pulse, it will have a power spectrum that is the Fourier transform of its envelope function and is centered at the optical frequency of its carrier. Generally, for any pulse shape, the frequency width of the spectrum is inversely proportional to the temporal width of the envelope. For a train of identical pulses, separated by a fixed interval, the spectrum can easily be obtained by a Fourier series expansion, yielding a comb of regularly spaced frequencies, where the comb spacing is inversely proportional to the time between pulses, i.e., proportional to the repetition rate f_r of the laser that is producing the pulses.

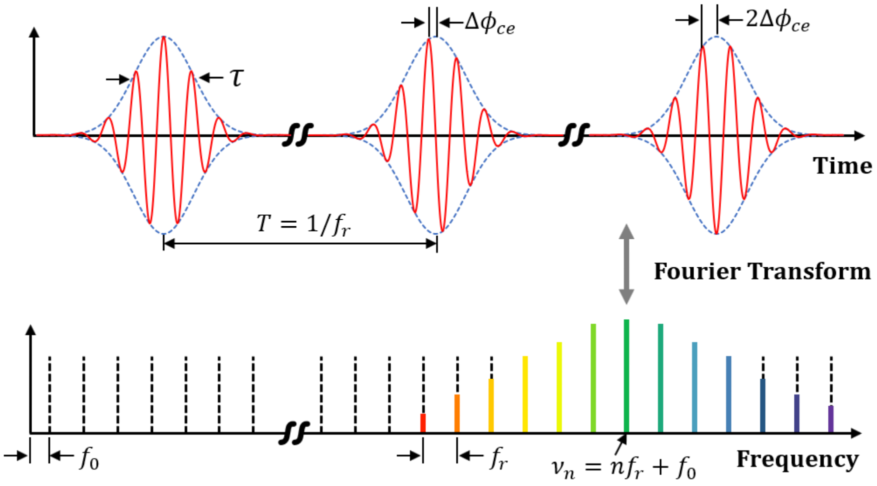

Fig. 2.6. Time and frequency domain of femtosecond laser frequency comb. (a). Time domain of femtosecond pulse laser. (b). Frequency domain frequency comb.

The Fourier relationship between time and frequency resolution guarantees that any spectrometer with sufficient spectral resolution to distinguish the individual comb lines cannot have enough temporal resolution to separate successive pulses. Therefore, the successive pulses interfere with each other inside the spectrometer and the comb spectrum occurs because there are certain discrete frequencies at which the interference is constructive. Using the result from Fourier analysis that a shift in time corresponds to a linear phase change with frequency, we can readily see that the constructive interference occurs at nf_r, where n is an integer.

When ϕ_{ce} is evolving with time, such that from pulse to pulse (at a time separation of $T = 1/f_r$) there is a phase increment by $\Delta\phi_{ce}$, then in the spectral domain, a rigid shift will occur for the frequencies at which the pulses add constructively. This shift is easily determined to be $(\Delta\phi_{ce})/2\pi T$. Thus, the optical frequencies, ν_n, of the comb lines are $\nu_n = nf_r + f_0$, where n is a large integer of the order of 10^6 that indexes the comb line, and f_0 is the comb offset due to the pulse-to-pulse phase shift. The comb offset is connected to the pulse-to-pulse phase shift by $f_0 = (\Delta\phi_{ce}\, f_r)/2\pi$. The pulse-to-pulse change in the phase for the train of pulses emitted by a mode-locked laser occurs because the phase and group velocities inside the cavity are different. The pulse-to-pulse change in the phase for the train of pulses emitted by a mode-locked laser can be expressed in terms of the average phase v_p and group v_g velocities inside the cavity. Specifically, $\Delta\phi_{ce} = \left(\frac{1}{v_g} - \frac{1}{v_p}\right) l_c \omega_c$, where l_c is the round-trip length of the laser cavity and ω_c is the "carrier" frequency.

2.5.3 Stability of the Repetition Rate

The stability of the pulse repetition rate in the time domain was measured and characterized by Allan deviation [75, 76], which is a two-sample deviation, so that it is convergent even if flicker noises is presented in the oscillators.

We have measured the long-term frequency change and the Allan deviation of our femtosecond laser, as shown in Fig. 2.7.

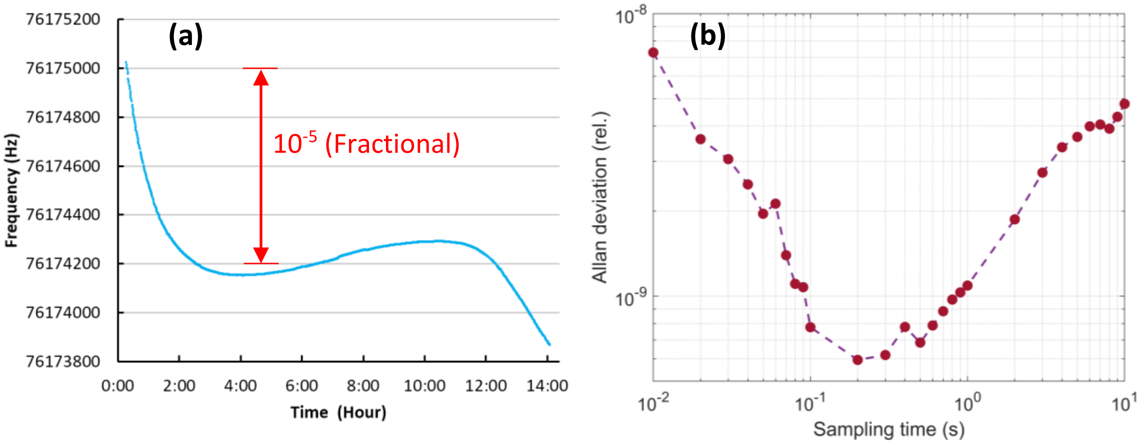

Fig. 2.7. Stability of the repetition frequency of the femtosecond laser. (a) Frequency drift in long term. (b) Measured Allan deviation in short term.

Within 14 hours, the repetition rate has changed by 1.2 kHz from a central frequency of around 76 174 kHz, corresponding to 10^{-5} of fractional frequency change. Since the tuning range is measured by multiplying f_r with the number of calibration peaks, the repetition rate uncertainty will cause large error considering the large number of the comb lines, normally in order of 5×10^3 (see Chapter 5 Measurement Results). From Eq. 2.18, the fractional error of the distance measurement caused by frequency measurement is proportional to the relative error of the frequency measurement, i.e. $\delta\Delta\nu/\Delta\nu = r\Delta f_r/rf_r \sim 10^{-5}$, where r is the number of calibration peak signal. To increase the accuracy, we measure the repetition rate each time when the tunable laser sweeps. Hence, the accuracy is then determined by the repetition rate change during the sweeping time, which is around 100 ms. From Fig. 2.7(b), this corresponds to an uncertainty of 8×10^{-10}, which is much smaller than the other error sources.

2.6. Conclusion

To overcome the problem of nonlinear tuning of the sweeping laser, we proposed using a frequency comb to calibrate the instantaneous frequency tuning range. The large number of the comb lines allows us to perform sub-measurements, which can increase the precision as we perform thousands of independent measurements in a single sweep. Using the sub-measurement, vibration of the target can also be monitored. In this chapter the theory backgrounds of frequency sweeping interferometry and frequency comb were presented separately. The presented two methods, i.e. using fringe counting and Fourier transformation, for absolute distance measurement were used in the experiment described in Chapter 5.

Chapter 3. Frequency Calibration of the Tunable Laser Source

3.1. Heterodyne between Tunable Laser and Frequency Comb

The frequency calibration of the TLS is achieved by analyzing the heterodyne signal between the TLS and the comb lines. In the following, we introduce the optical heterodyne realization and its characteristics. Heterodyne detection in radio wave and microwave dates back to early 20th century, in which the weak signal is mixed with a strong reference signal called 'local oscillator' on nonlinear devices such as a rectifier [77]. The mixed wave contains their sum and difference frequencies. In a report in 1962 [78], the optical heterodyne was realized by mixing the signal and the local oscillator on a square-law detector, which responds in proportion to the square of the interfering fields or currents as the case may be. All photo detectors are square-law in this sense.

3.1.1 Optical Heterodyne

Optical heterodyne is an interference detection that involves two laser inputs, $E_s(t)$ and $E_L(t)$, with a slightly different frequencies that can be written in complex function as:

$$\begin{aligned} E_s(t) &= E_{s0}\exp(i2\pi\nu_s t + i\phi_s) \\ E_L(t) &= E_{L0}\exp(i2\pi\nu_L t + i\phi_L) \end{aligned} \qquad \text{Eq. 3.1}$$

Using a beam splitter, the signal and the local oscillator laser beams are combined in a photodetector. The resulting electric field can be written as following assuming the polarization direction of the input light is the same:

$$E(t) = E_s(t) + E_L(t) \qquad \text{Eq. 3.2}$$

The photodetector responds to the envelope of the oscillating electric field, that can be expressed as the multiplication of the complex functions and their conjugation:

$$i(t) = E(t)E^*(t) = R_i[E_s(t) + E_t(t)][E_s^*(t) + E_L^*(t)] \qquad \text{Eq. 3.3}$$

where R_i is the response of the photodetector. Substituting Eq. 3.1 into Eq. 3.3 and ignoring the DC component, we have the heterodyned intermediate frequency (IF) signal as:

$$i_{IF}(t) = R_i E_{s0} E_{L0}\cos[2\pi(\nu_s - \nu_L)t + (\phi_s - \phi_L)] \qquad \text{Eq. 3.4}$$

The beating frequency equals to the frequency difference of the signal and the local oscillator laser. To detect the beat signal, the bandwidth of photo detection circuit should be larger than the beating frequency. In addition, the following conditions should be satisfied for optical heterodyne with high SNR.

3.1.2 Conditions of Alignment for Optical Heterodyne

The photocurrent in the basic equation of optical heterodyne Eq. 3.4 is derived by assuming the wave fronts of the signal and the local oscillator fields keep the same phase difference over the entire activate area of the photodetector. Since the optical wavelengths are much smaller than the dimension of the photodetector, the wave mixing photocurrent in essence is the integration of the differential photocurrent over the photodetector surface. Only when the signal and the local oscillator laser beams have the same phase difference over the entire photodetector surface, the mixed intermediate frequency current is maximum. Effective mixing requires the following conditions should be satisfied:

(1). Both the signal and the local oscillator are coherent light sources, such that phase difference in time domain can be kept.

(2). The beams of the signal and the local oscillator should be overlapped, and to generate maximum SNR, the two beams should have the same radius. The area where two fields are not overlapped cannot produce mixing current but produces noise.

(3). The electric fields of the signal and the local oscillator have the same directions of energy flux. This means the two laser beams should be aligned in parallel.

(4). Under the condition of (3), the wavefronts should also have the same curvature, both are planar or curved.

(5). The polarization directions of the signal and the local oscillator should be in parallel because the resulted field is the vector summation of the two input fields.

By selecting proper laser sources and optics for laser beam collimation, the conditions of (1) (2) (4) and (5) are relatively easy to satisfy. In the following, we focus on the condition (3).

3.1.2.1 Situation Where Two Beams are not Paralleled

For simplicity, we assume that one of the laser beams is perpendicular to the surface of the detector, which is modeled as a square with side length d. The phase distributions along y axis are assumed to be identical. As the coordinates illustrated in Fig. 3.1, we can write the electric fields of the signal and local oscillator as:

$$E_s(\boldsymbol{r}, t) = E_{s0}\cos(2\pi\nu_s t - \boldsymbol{k}_s \cdot \boldsymbol{r}) \quad \text{Eq. 3.5}$$

$$E_L(\boldsymbol{r},t) = E_{L0}\cos(2\pi\nu_L t - \boldsymbol{k}_L \cdot \boldsymbol{r})$$

where $\boldsymbol{k}_s$ and $\boldsymbol{k}_L$ are the wave vectors of the signal and the local oscillator. The position vector $\boldsymbol{r}$ on the detector surface can be expressed as:

$$\boldsymbol{r} = x\boldsymbol{i} + y\boldsymbol{j} \qquad \text{Eq. 3.6}$$

Thus Eq. 3.5 can be written as:

$$\begin{gathered} E_s(\boldsymbol{r},t) = E_{s0}\cos(2\pi\nu_s t) \\ E_L(\boldsymbol{r},t) = E_{L0}\cos(2\pi\nu_L t - k_L x\sin\theta) \end{gathered} \qquad \text{Eq. 3.7}$$

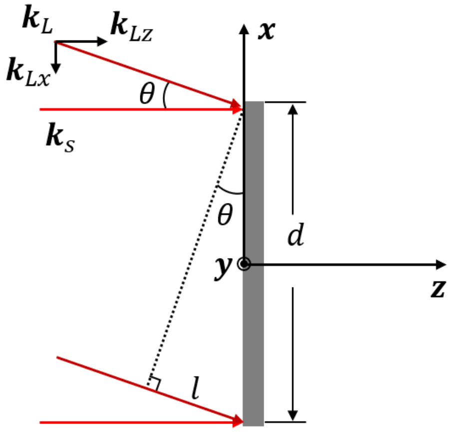

Fig. 3.1. Illustration of laser beam alignment for optical heterodyne detection.

Substituting Eq. 3.7 into Eq. 3.4, the generated IF photocurrent at $\boldsymbol{r}$ is:

$$i_{IF}(\boldsymbol{r},t) = R_i E_{s0} E_{L0}\cos[2\pi(\nu_s - \nu_L)t + k_L x\sin\theta] \qquad \text{Eq. 3.8}$$

The overall photocurrent can be written as:

$$\begin{aligned} i_{IF}(t) &= \frac{1}{d}\int_{-\frac{d}{2}}^{\frac{d}{2}} i_{IF}(\boldsymbol{r},t)dx \\ &= \frac{R_i E_{s0} E_{L0}}{d}\int_{-\frac{d}{2}}^{\frac{d}{2}} \cos[2\pi(\nu_s - \nu_L)t + k_L x\sin\theta]\,dx \end{aligned} \qquad \text{Eq. 3.9}$$

Considering θ is small, so that $\sin\theta \approx \theta$. The integral of Eq. 3.9 is:

$$i_{IF}(t) = R_i E_{s0} E_{L0} \sin\left(\frac{k_L d\theta}{2}\right) \cdot \cos[2\pi(\nu_s - \nu_L)t] \qquad \text{Eq. 3.10}$$

Hence, the amplitude of the mixed IF photocurrent is modulated by the relative angle of the laser beams. When

$$\frac{k_L d\theta}{2} = \pi \qquad \text{Eq. 3.11}$$

the amplitude becomes 0. At this point, the maximum acceptable angle equals:

$$\theta_{max} = \frac{\lambda}{d} \qquad \text{Eq. 3.12}$$

This indicates that the heterodyne amplitude is greatly affected by the parallelism of the two beams. Since θ_{max} wavelength λ_L, it is easier to realize heterodyne detection with infrared light than with visible light. In our case, the wavelengths used are around 1550 nm. If we take a detector with 0.5 mm diameter, the maximum angle is calculated as θ_{max} = 3.11 mrad diverge by 3.11 mm at a distance of 1 m. This precision of alignment is relatively easy to be realized by manually adjusting the positioning stages.

3.1.2.2 Situation Where Detector Surface is not Perpendicular to Paralleled Beams

This section discusses the situation when the two laser beams are paralleled but are not perpendicular to the photodetector surface. As the coordinate shown in Fig. 3.2, the electric fields of the signal and the local oscillator on the surface of detector can be written as:

$$\begin{aligned} E_s(\boldsymbol{r}, t) &= E_{s0} \cos(2\pi\nu_s t - k_s x \sin\theta) \\ E_L(\boldsymbol{r}, t) &= E_{L0} \cos(2\pi\nu_L t - k_L x \sin\theta) \end{aligned} \qquad \text{Eq. 3.13}$$

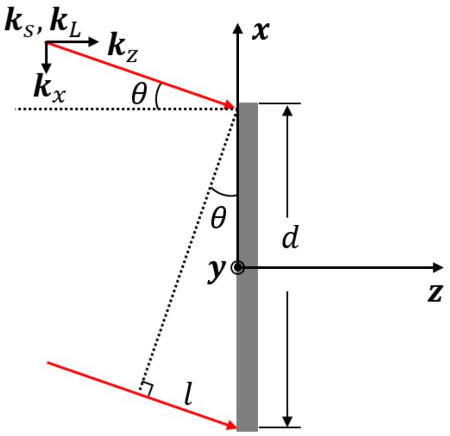

Fig. 3.2. Illustration of the detector surface is not perpendicular to the paralleled two beams in heterodyne detection.

Considering $\sin\theta \approx \theta$, the IF photocurrent at point $\boldsymbol{r}$ can be written as:

$$i_{IF}(\boldsymbol{r}, t) = R_i E_{s0} E_{L0} \cos[2\pi(\nu_s - \nu_L)t + \Delta k \cdot x\theta] \qquad \text{Eq. 3.14}$$

where:

$$\Delta k = k_s - k_L = \frac{2\pi(\nu_s - \nu_L)}{c} \qquad \text{Eq. 3.15}$$

The overall IF photocurrent is:

$$i_{IF}(t) = R_i E_{s0} E_{L0} \sin\left(\frac{\Delta k \cdot d\theta}{2}\right) \cdot \cos[2\pi(\nu_s - \nu_L)t] \qquad \text{Eq. 3.16}$$

When $\frac{\Delta k d\theta}{2} = \pi$, we have:

$$\theta_{max} = \frac{\Lambda}{d} \qquad \text{Eq. 3.17}$$

where $\Lambda = \frac{c}{\Delta\nu}$ is the synthetic wavelength, which is much larger than the wavelengths of the heterodyne lasers. In our case, $\Delta\nu = 25$ MHz and $d = 0.5$ mm, we have $\theta_{max} = 2.4 \times 10^4$ at the direction alignment of the photodetector is not a critical problem.

3.1.3 Heterodyne Signal of Frequency Comb with a sweeping Laser

The schematic of heterodyne detection between a signal frequency laser and a comb is shown in Fig. 3.3.

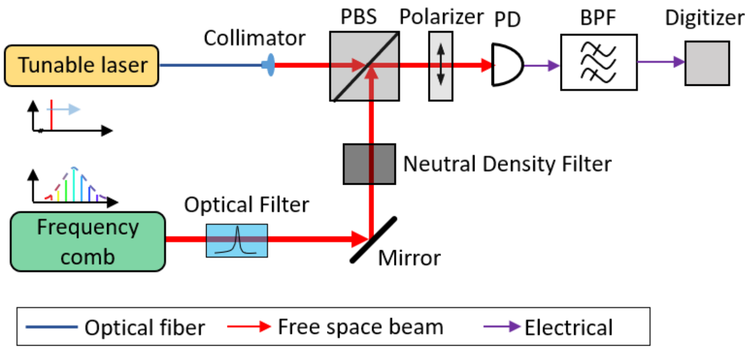

Fig. 3.3. Schematic of heterodyne detection between a single frequency laser and a comb. PD: photodetector. BPF: bandpass filter. PBS: polarized beam splitter.

It should be noticed that due to large number of comb lines, the optical power of an individual comb line is weak. E.g., for our system, it is estimated to be about 4 nW. On the other hand, the power of the beat signal at nf_r is strong. In order to detect such weak signal, we use the following methods. First, we use an optical bandpass filter to increase the ratio between the power of the individual comb line and the total power of the femtosecond laser. The −3dB bandwidth of the optical bandpass filter is 8 nm. Compared to the original spectral width of 80 nm, the ratio is increased by a factor of about 10. Secondly, we used a high gain photodetector and using the highest power of the tunable laser source. Thirdly, we selected a narrow bandpass filter (-3dB bandwidth 2.5 MHz) centered at 25 MHz which attenuates the repetition frequency by 60 dB. So that the strong power of the repetition rate can be sufficiently attenuated. It is also important to well align the light beams of the TLS and the femtosecond laser, and make sure that the polarization directions are identical.

A frequency comb can be regarded as the superposition of large number of lasers, whose frequencies are separated by the repetition rate f_r. As illustrated in Fig. 3.4(a), the heterodyne signal between a tuning laser source and a frequency comb is superposition of the beating signal between these lasers:

$$i(t) = R\left\{\begin{array}{c} P_{TLS} + P_{FC} + \sum_{n=0}^{N} P_n \cos[2\pi n f_r t \ + \phi_{In}] \\ + \sum_{n=-N}^{N} \sqrt{P_{TLS}P_M} \cos[2\pi(\nu_T - \nu_n + nf_r)t + \phi_{Tn}] \end{array}\right\} \qquad \text{Eq. 3.18}$$

Here, P_{TLS}, P_{FC} and P_M are the power of the TLS, frequency comb, and a single comb line respectively. ν_T and ν_n are optical frequencies of the tunable laser and its nearest comb line. Eq. 3.18 contains frequency components produced by the beat notes between comb lines (nf_r) and the chirped heterodyne frequencies between the tunable laser and the comb lines ($\nu_T - \nu_n + nf_r$). The highest frequency of the detected signal is limited by the detector bandwidth. These frequencies repeat as the tunable laser sweeps across the comb lines. The spectrogram of the heterodyne signal is shown in Fig. 3.4(b), in which we can see the multiple frequencies at a given time and the repeating structure. It should be noted that the different frequency components at a given time have the same chirp rate. In addition, the components with the same chirp direction, up or down, are just offset by integer times of the comb line interval, i.e., the repetition rate. Hence, it is sufficient to have the components less than half of the repetition rate for instantaneous frequency retrieving.

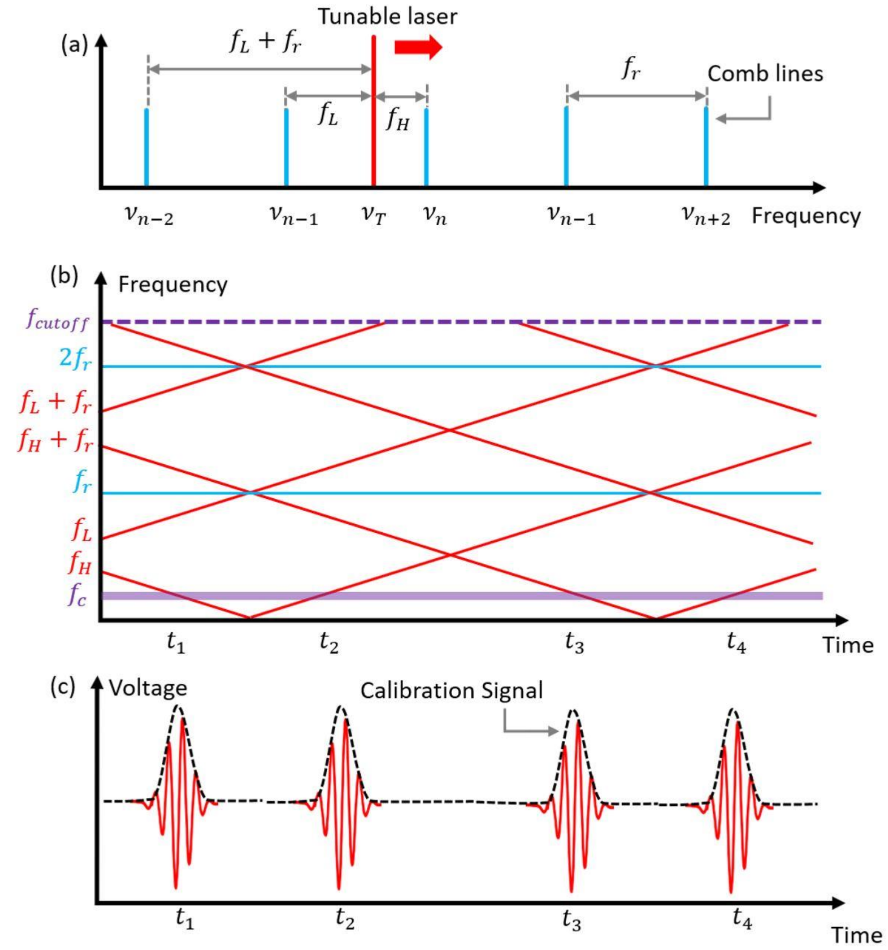

Fig. 3.4. Illustration of frequency calibration of the tunable laser using frequency comb and filtering. (a). Illustration of the frequencies of the tunable laser and the comb lines. (b). Spectrogram of the heterodyne signal during frequency tuning. Red skew lines represent the chirped heterodyne signal between the tuning laser and the comb lines, and the solid purple line represents the passband of NBF. (c). The calibration peaks generated by filtering the heterodyne signal. These peaks correspond to the frequency of TLS equaling to $\nu_n \pm$, where ν_n is the frequency of the comb lines, and is the passband of the NBF.

Using a broadband photodetector with a bandwidth of about 200 MHz, we have recorded the heterodyne signal with tuning speed of 5 nm/s and 10 nm/s. The spectrogram is shown in

Fig. 3.5. The spectrograms were obtained using short-time Fourier transform with 1 µs temporal resolution and 1 MHz spectral resolution.

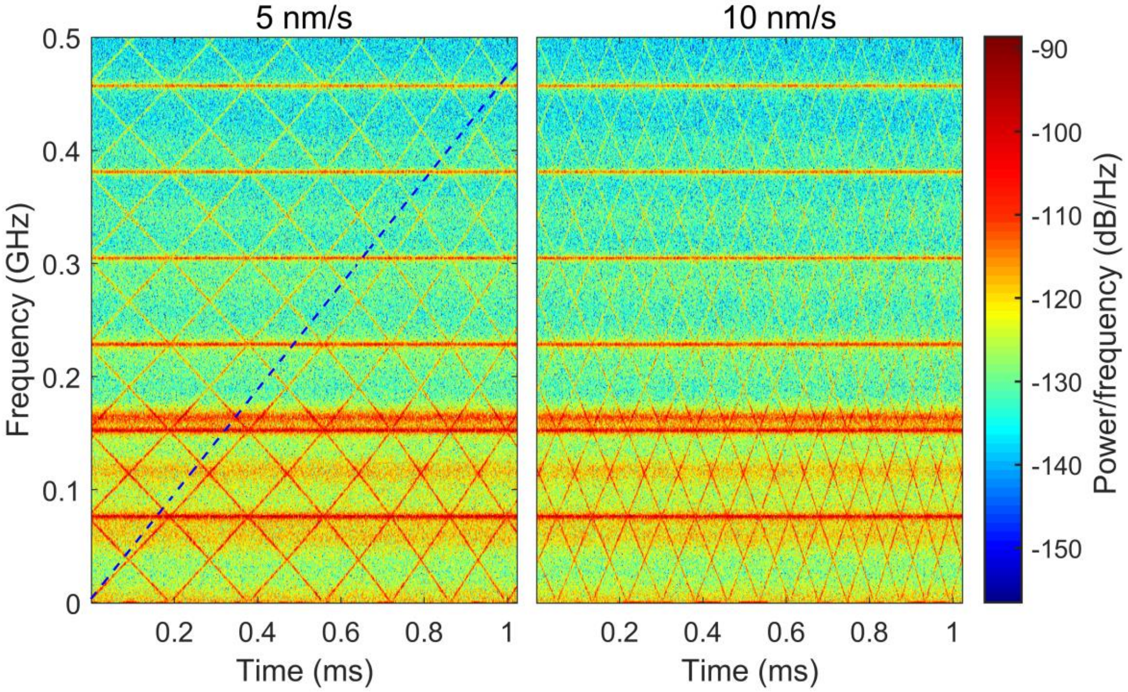

Fig. 3.5. Experimental result of the spectrogram of the raw heterodyne signal. The straight blue dashed line as a reference allows to appreciate the nonlinear tuning behavior of the tunable laser.

It clearly shows that within the recorded 1 ms, the tunable laser has swept by 6 comb lines for 5 nm/s and 14 comb lines for 10 nm/s tuning speed. The blue dashed line as a reference shows the nonlinear tuning behavior of the tunable laser within 1 ms. The average tuning speed is calculated as:

$$\bar{v}_{5\mathrm{nm}/s} = \frac{6 \times 76.174\mathrm{MHz}}{1\mathrm{ms}} = 457.044\ \mathrm{GHz/s} \rightarrow 3.66\ \mathrm{nm/s\ at\ 1550\ nm}$$

$$\bar{v}_{10\mathrm{nm/s}} = \frac{14 \times 76.174\mathrm{MHz}}{1\mathrm{ms}} = 1066.436\ \mathrm{GHz/s} \rightarrow 8.54\ \mathrm{nm/s\ at\ 1550\ nm}$$

The instantaneous frequency can be calibrated using this method. However, there are several drawbacks restricting the application for distance metrology system.

- As the general problem of using off-line signal processing, high speed sampling and large memory is required, and cannot be realized in real-time.

- To fully record the heterodyne signal, which has largest frequency as half of the repetition rate, the sampling rate should be at least f_r (typically around 100 MHz). Expensive high-speed digitizer is required, e.g. about $8,000 for NI5112 from National Instrument (100

MS/s sampling rate but with 8 bits limited resolution). In our experiment, the fast digitizing was performed using an oscilloscope, which has a maximal memory depth of 2 million points. This means that, if we fully record the heterodyne signal, the sampling time will be limited to about 26 ms, which corresponds to 0.1 nm tuning range for the highest tuning speed of 40 nm/s.

- The signal-to-noise ratio of the heterodyne signal is low because of the weak power in each comb line (several nanowatt). The electrical narrow bandpass filter in our work makes the heterodyne detection easier by confining the bandwidth.

In our system, a narrow bandpass filter (NBF) is used to select these frequency components. The NBF filters out the frequency components other than the heterodyne signal between the TLS and its nearest comb line. When the frequency of the TLS tunes to positions that are equal to $\nu_n \pm$, where ν_n is the frequency of the comb lines, and $\mathrm{F_{cf}}$ is the passband of the NBF, peak signals will be produced. Thus, these peaks are the time markers that the frequency of the TLS is equal to $\nu_n \pm$. The result of using filter approach for large tuning range calibration is presented in Chapter 3.

3.2. Simulations of Heterodyne Signal Filtering

As the core component of the frequency calibration system, the narrow bandpass filter (NBF) affects the spectral resolution and signal-to-noise-ratio (SNR) of the calibration peaks. In this section, the optimization of the NBF is discussed. From the heterodyne signal between the tunable laser and the frequency comb Eq. 3.18, we can see that the heterodyne signal has the same chirp rate as the quasi-linearly tuned laser. We consider the response of the NBF to an ideal linearly chirped signal by giving the analytic expression and simulations. The effect of the phase noise in the chirped signal that is introduced by the lasers will be discussed in Chapter 4.

3.2.1 Response of Linear Time-Invariant (LTI) Systems Under Dynamic Input

From the heterodyne signal between the linearly tuned laser and the comb in Eq. 3.18, we can see that the heterodyne signal has the same chirp rate as the tuning speed of the laser. The NBF behaves as a frequency-voltage discriminator, through which the filtered amplitude of the heterodyne signal is a function of the input frequency. When a linearly chirped signal enters the NBF, ideally, the filtered calibration signal follows the amplitude response characteristic of the NBF, so that we can determine the instantaneous frequency of the input chirping signal from the envelope of the calibration peaks, and design very narrow filters for better frequency resolution. However, as discussed in the following section, the output of the NBF under dynamic input deviates from the static response characteristic of an LTI system, and is a function of the filter type and the chirping rate of the input signal. To characterize the output signal, first we write the heterodyne signal between the linearly tuned laser and one of the comb lines in complex function as:

$$S_i(t) = \exp\left[i2\pi\left(+\frac{v_S t}{2}\right)t + i\phi_0\right] \qquad \text{Eq. 3.19}$$

where v_S is the frequency tuning speed. The output of the LTI system can be written as the convolution between the impulse response of the LTI system and the input:

$$S_o(t) = \int_{-\infty}^{+\infty} h(\tau)S_i(t-\tau)d\tau \qquad \text{Eq. 3.20}$$

where $h(t)$ is the impulse response of the LTI system that satisfies $h(t) = 0$, when $t < 0$ and t approaches infinity. Substituting Eq. 3.19 into Eq. 2.20 we have:

$$\begin{aligned} S_o(t) &= \int_{-\infty}^{+\infty} h(\tau)\exp\left[i2\pi\left(+\frac{1}{2}v_S(t-\tau)\right)(t-\tau) + i\phi_0\right]d\tau \\ &= \int_{-\infty}^{+\infty} h(\tau)\exp[-i2\pi(+v_S t)\tau]\exp[i\pi v_S\tau^2]\,d\tau \qquad \text{Eq. 3.21} \\ &\cdot \exp\left[i2\pi\left(+\frac{1}{2}v_S t\right)t + i\phi_0\right] = H_d(t)S_i(t) \end{aligned}$$

where $H_d(t)$ is the voltage transfer function that corresponds to the instantaneous frequency of the input signal *f*, which can be written as:

$$f = +v_S t \qquad \text{Eq. 3.22}$$

Here, F_{cf} is the central frequency of the bandpass filter. As can be seen from Eq. 3.21, if we consider the response of the filter to a signal frequency f, we can also write the output of that frequency as:

$$S_o(i2\pi f) = H_d(i2\pi f) \bullet S_i(i2\pi f) \qquad \text{Eq. 3.23}$$

with:

$$H_d(i2\pi f) = \int_{-\infty}^{+\infty} h(\tau)\exp[-i2\pi f\tau]\exp[i\pi v_S\tau^2]\,d\tau \qquad \text{Eq. 3.24}$$

Eq. 3.23 shows the output of an LTI system when the frequency of input changes with time. The system responds the input frequency f with a manner indicated by the dynamic transfer function $H_d(2\pi f)$, rather than static transfer function of the system. Taking the Taylor expansion of $\exp[i\pi v_S \tau^2]$ and exchanging the order of the integration and summation, we have:

$$H_d(i2\pi f) = \sum_{n=0}^{+\infty} \frac{(i\pi v_S)^n}{n!} \int_{-\infty}^{+\infty} h(\tau) \exp[-i2\pi f\tau]\, (-\tau)^{2n} d\tau \qquad \text{Eq. 3.25}$$

which equals:

$$H_d(i2\pi f) = H(i2\pi f) + \sum_{n=1}^{\infty} \frac{(i\pi v_S)^n}{n!} \frac{d^{2n} H(j2\pi f)}{d(j2\pi f)^{2n}} \qquad \text{Eq. 3.26}$$

where $H(i2\pi f)$ is the static transfer function that is the Fourier transform of the impulse response $h(t)$:

$$H(i2\pi f) = \int_{-\infty}^{+\infty} h(\tau) \exp[-i2\pi f\tau]\, d\tau \qquad \text{Eq. 3.27}$$

Eq. 3.26 clearly shows that when the tuning speed v_S is small, the dynamic transfer function approximates to the static response. By defining the normalized detuning frequency f_N instead of the natural frequency f:

$$f_N = \frac{f -}{\frac{BW}{2}} \qquad \text{Eq. 3.28}$$

where BW is bandwidth of the NBF, so that we have:

$$\left| \frac{H\left[i2\pi\left(+\frac{BW}{2}\right)\right]}{H(i2\pi)} \right| = \frac{1}{\sqrt{2}} \qquad \text{Eq. 3.29}$$

We can rewrite Eq. 3.26 in the ‘prototype’[2] form, which the bandwidth BW of the NBF is normalized, as :

$$H_d(if_N) = H(if_N) + \sum_{n=1}^{N} \frac{(i\pi v_{SN})^n}{n!} \frac{d^{2n} H(if_N)}{d(if_N)^{2n}} + o(if_N) \qquad \text{Eq. 3.30}$$

where v_{SN} is the normalized dimension-less tuning speed, which is defined as:

---

[2]. Note that the property that all other filters that belongs the same class and order as the prototype filter can be derived from it by applying a scaling factor to the components of the prototype. Where the cut-off angular frequency is normalized to 1 rad/s.

$$v_{SN} = \frac{v_S}{BW^2} \qquad \text{Eq. 3.31}$$

and $o(if_N)$ is the remainder of the Taylor expansion, which equals to:

$$o(if_N) = \frac{(i\pi v_{SN})^{N+1}}{(N+1)!} \frac{d^{2(N+1)}H(ix)}{d(ix)^{2(N+1)}}\bigg|_{x=\theta(x)} \qquad \text{Eq. 3.32}$$

with $\theta(x) \in (0, f_N)$ and the error of Eq. 3.32 is not greater than the modulus of the residual:

$$\Delta \leq \frac{(i\pi v_{SN})^{N+1}}{(N+1)!} \left|\frac{d^{2(N+1)}H(ix)}{d(ix)^{2(N+1)}}\right|_{x=\theta(x)} \qquad \text{Eq. 3.33}$$

Eq. 3.33 can serve for the estimation of the admissibility of the analysis of Eq. 3.30 for a given chirp rate v_{SN}.

Theoretical analysis of the filtered output of Eq. 3.30 at small chirp rate v_{SN} ($v_{SN} < 0.1$) has been presented in [79]. It shows that the amplitude is attenuated, the passband is broadened, and the central frequency position is shifted (the maximum output does not occur at the input of F_{cf}). The more rapid the signal frequency variation, the more strongly distorted is the amplitude frequency characteristic.

3.2.2 Performance Parameters

From Eq. 3.30 we can see that the filtering process can be expressed in the normalized form, which is a function of the type and the order of the NBF and the normalized chirp rate v_{SN}. This gives us the convenience of selecting the desired bandwidth by frequency scaling. This is shown in Fig. 3.6, in which the filtered envelopes in (a) and (b) have different width in time domain. After frequency normalization, the filtered signals have the same envelope with respect to the normalized frequency. The following simulations and discussions are based on the normalized parameters. In the simulation, a linearly chirped signal was firstly generated as the heterodyne signal between the swept laser and one of the comb lines; different types of bandpass filters were then used to filter the linear chirped signal.

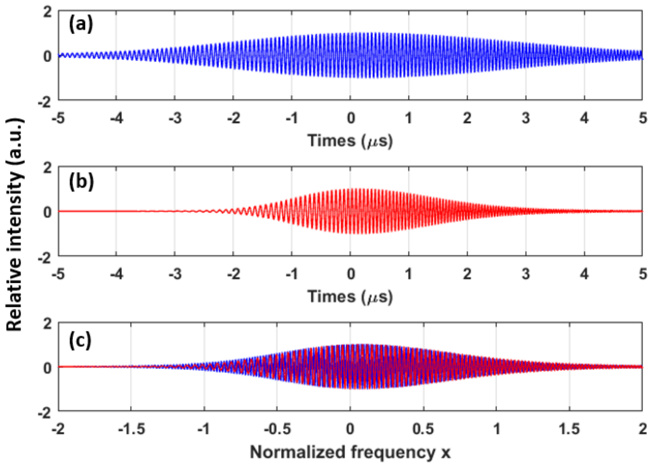

Fig. 3.6. The filtered signal at different chirp rate. (a) v=624GHz/s, BW=2.5MHz, 5th Gaussian filter. (b) v=2.5 THz/s, BW=5.0 MHz, 5th Gaussian filter. (c) The filtered signal as a function of the normalized frequency $x = \frac{2(f-)}{BW}$, where and BW are the central frequency and the bandwidth of the NBF respectively.

In general, the filtered signal deviates from the transfer function of the NBF, as shown in Fig. 3.7. The maximum amplitude is attenuated, the bandwidth is widened, and the central frequency is shifted compared with the transfer function or the ideal static response. We defined these distortion parameters as following:

- Amplitude attenuation A_p: the ratio of the maximum amplitude of the filtered signal to the maximum amplitude of the transfer function.
- Bandwidth of the transfer function (BW) and the filtered signal (BW'): the full width corresponding to the amplitude drop down to 0.707 of the maxima of the transfer function and the filtered signal.
- Bandwidth broadening BW/BW': the ratio between the bandwidth of the transfer function and that of the filtered signal.
- Central frequency shift Δf: the distance from the central frequency of the transfer function and the frequency, at which the maximum amplitude locates, of the filtered signal.

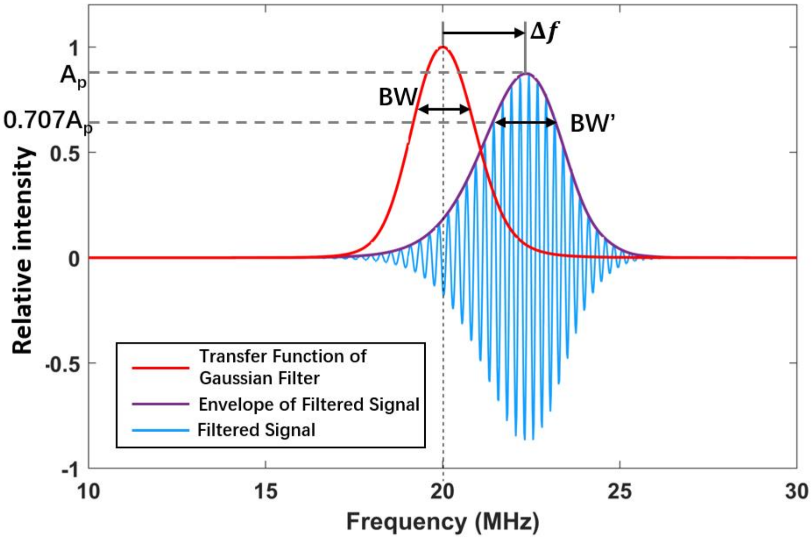

Fig. 3.7. Distortion Illustration of the filtered signal under linear chirp input. BW and BW' are the -3 dB bandwidths of the filter and the filtered chirp signal. Δf is the central frequency shift of the filtered signal. Here, a 5th-order Gaussian bandpass filter with a bandwidth of $BW = 1.5$ MHz centered at 20 MHz was used to filter a chirp signal with chirping rate 5 THz/s (normalized tuning speed $v_{SN} = 2.22$). Ap $= 0.86$, BW' $= 1.92$ MHz and $\Delta f = 2.5$ MHz.

In the following simulations, the Gaussian and Butterworth filters of 2nd and 5th order are used to present the above distortion parameters. These two types of filter are chosen based on the fact that, the Gaussian filters process high frequency selectivity but with relatively poor phase linearity and respectively, and Butterworth filters are on the contrary.

3.2.3 Simulation Results

The frequency resolution is related to the peak width of the filtered signal BW', which is defined in Fig. 3.7. and Eq. 3.30. Fig. 3.7 shows that, at small normalized chirp rate, the filtered signal follows the amplitude-frequency response curve, so that $BW' = BW$. The ratio between BW' and BW is shown in Fig. 3.8. It can be seen that the width of the filtered signal becomes larger when the normalized chirp rate v_{SN} increases. The actual width of BW' for 624 GHz/s chirp rate (corresponds to 5 nm/s at 1550 nm tuning speed) using different bandwidth NBF is shown in Fig. 3.8(b). There exists an optimal bandwidth around 0.5 MHz for the Gaussian filters and the 2nd order Butterworth filter, and 1.25 MHz for 5th Butterworth filter, that produce narrowest filtered bandwidth that are little larger than 0.5 MHz. However, the normalized chirp rate v_{SN} reaches 2.5 when taking 0.5 MHz filter, meaning that the filtered peak is strongly attenuated according to Fig. 3.10. When taking 1.25 MHz for the 5th order Butterworth filter, the normalized chirp rate is 0.4, which produces high peak value.

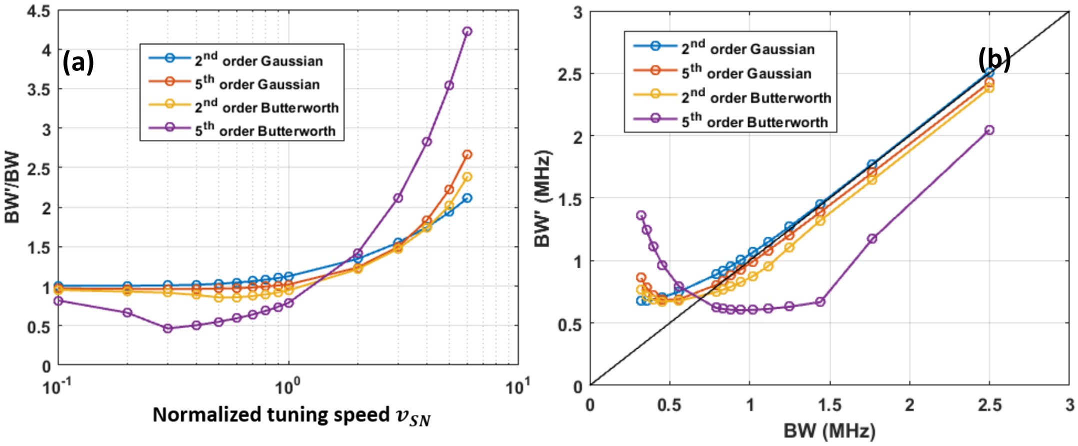

Fig. 3.8. The bandwidth of the filtered signal at different chirp rates. (a) Ratio between BW and BW'; (b) The bandwidth of the filtered signal. Chirp rate $v_S = 624$ GHz/s. v_{SN}: normalized chirp rate defined in Eq. 3.31.

The central frequency of the filtered signal is deviated from the central frequency of the filter under static condition. Refer to Fig. 3.7, the normalized central frequency shift is defined as:

$$\Delta = \frac{2\Delta f}{BW} \qquad \text{Eq. 3.34}$$

Fig. 3.9 shows that when the normalized chirp rate becomes large, the central frequency has larger deviation. Considering that the tuning speed of the tunable laser in the frequency calibration system is not constant, it is important to examine the variation of Δf when the chirp rate fluctuates.

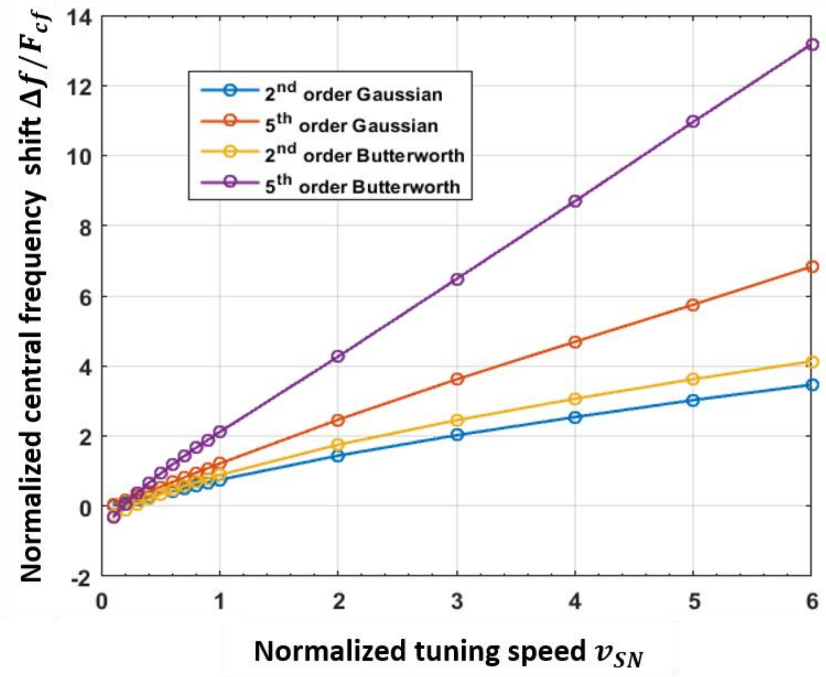

Fig. 3.9. Central frequency position at different chirp rates. v_{SN}: normalized chirp rate defined in Eq. 3.31.

The attenuation of the filtered signal compared to the static amplitude-frequency response is related to the normalized chirp rate, as shown in Fig. 3.10. The peak values drop to around 0.8 at chirp rate $v_{SN} = 2$ for the filters. And at smaller chirp rate, the peak of the Butterworth filters has gain caused by overshoot, especially for the higher order one.

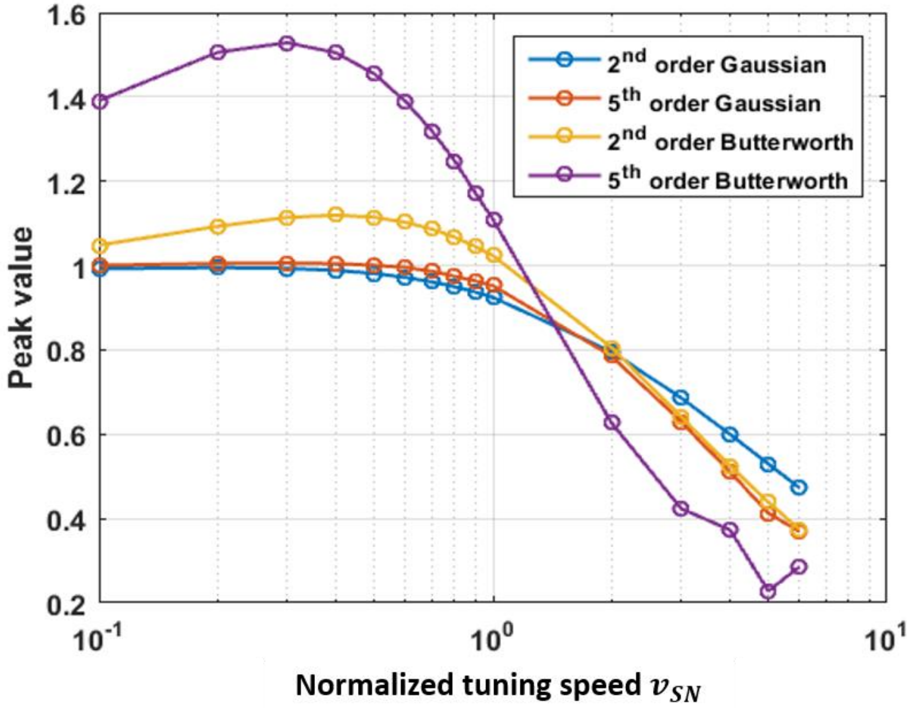

Fig. 3.10. Peak value attenuation at different chirp rates. v_{SN}: normalized chirp rate defined in Eq. 3.31.

In summary, smaller normalized chirp rate $v_{SN} = \frac{v_S}{BW^2}$, where v_S is the tuning speed and BW is the bandwidth of the filter, means less deviation of the peak envelope from the transfer function of filter. In this sense, we should design filters with larger bandwidth and using lower tuning speed of the sweeping laser. However, to obtain sharper peaks for better spectral resolution, a compromise of the bandwidth should be made. From the results in figures from Fig. 3.8 to Fig. 3.10, a bandwidth satisfies the normalized tuning speed $v_{SN} \approx 1$ is a good choice. This result is in coincidence with a thumb of rule adopted in Ref. [80] and [81] for bandwidth selection of the NBF, which stated that the bandwidth of the NBF should be chosen that its rise time $(1/BW)$ is smaller than the time required for the chirping frequency to pass through the bandwidth of the NBF (BW/v_S).

3.3. Filter Design

We have considered different approaches for constructing the filter: surface mount filter on an electronic board, a ceramic filter and a surface acoustic wave filter. Whereas the latter are on the shelf products and having non-optimal specifications for our application we optimized a surface mount component filter. We designed a filter having a bandwidth near 2.5 MHz at -3 dB and a central frequency around 25 MHz. Increasing the order of the filter allows us narrowing the bandwidth, but under 2 MHz the attenuation increases drastically. As the filter needs high attenuation in the stop band to skip of the repetition frequency, we have split the problem in two by cascading a third order Butterworth filter and a third order Gaussian filter. The Gaussian filter has a larger bandwidth and mainly attenuates the repetition frequency. The Butterworth filter has the narrow bandwidth. Both filters have attenuation respectively 2 dB and 6 dB. Attenuation was compensated with amplifiers with 12 dB gain and the amplifiers achieve also impedance matching between the photodiode transimpedance amplifier (TIA), the filters themselves and the 50 Ohms load circuit of the oscilloscope. Fig. 3.11 shows the filter chain.

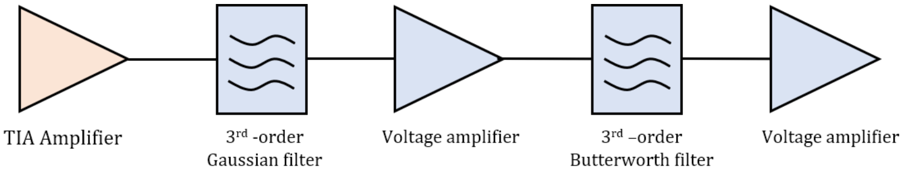

Fig. 3.11. Schematic of narrow bandpass filtering chain with the amplifiers.

The frequency response of the filter can be seen in Fig. 3.12. The filter has a 3 dB bandwidth of 2.6 MHz and an attenuation of 65 dB in the stop band around the repetition frequency. One can see that the global shape of the filter is rather Gaussian.

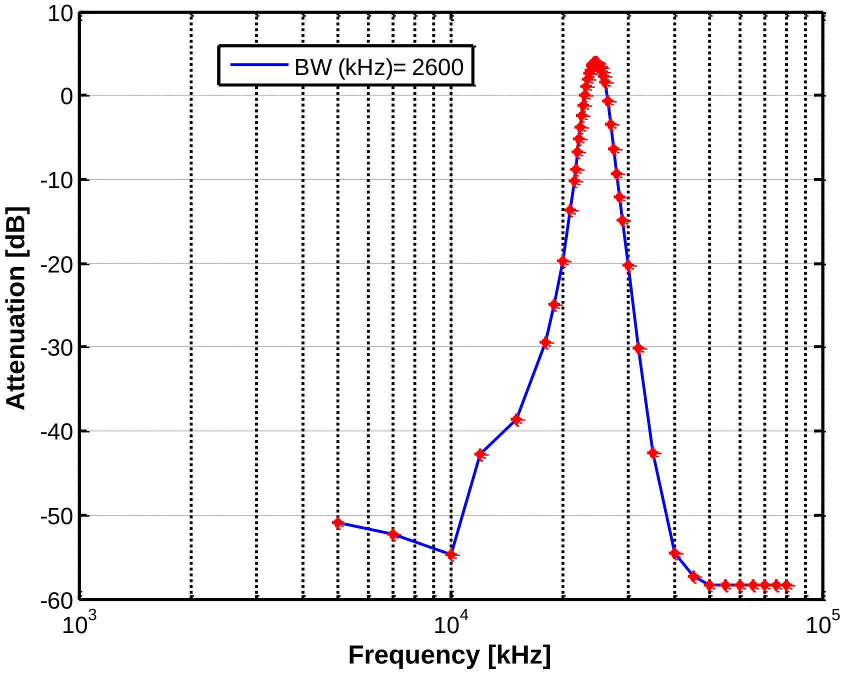

Fig. 3.12. Frequency response of the filter used for filtering the heterodyne signal between the comb and the tunable laser. Red points are the measured data.

We have also tested the ceramic filter and the Surface Acoustic Wave filters (SAW). More information on these filters can be seen in Appendix C. The ceramic filter has a central frequency of 10.7 MHz with an insertion loss of 6 dB. The 3 dB bandwidth is around 280 kHz with an attenuation of 50 dB in the lower stop band and a spurious attenuation greater than 40 dB in the higher stopband. This filter has sharp edges.

The SAW filter has a central frequency of 62 MHz. As it is near the repetition frequency, a notch filter was implemented in serial. The SAW filter has insertion loss of 18 dB a stopband attenuation of 42 dB.

With both of these filters we could not observe any heterodyne signal even we used the smallest tuning speed (5 nm/s at 1550 nm). These two filters have very sharp edges and a small bandwidth but exhibit high insertion loss and thus can difficultly fulfill the requirements of the ideal filter, even if their specifications are not far away from the ideal prototype.

3.4. Experimental Results

The filter used for filtering the heterodyne signal has a bandwidth near 2.5 MHz at -3 dB and a central frequency around 25 MHz. This corresponds to a normalized chirp rate for 40 nm/s of:

$$v_{SN} = \frac{\frac{40\text{nm/s}}{(1550\text{nm})^2} c}{(2.5\text{MHz})^2} = 0.7984$$

At this normalized chirp rate, the bandwidth broadening is less than 10% while the attenuation is less than 5% for the Gaussian filters and 2nd order Butterworth filter. The experimental setup for calibrating the instantaneous frequency of the tuning laser is similar to Fig. 3.3. Using peak detection sampling mode of an oscilloscope, we recorded the envelope of the generated peaks. Data were squared to obtain better SNR and the result is shown in Fig. 3.13. From figure (b) we can see different pairs of peaks that their central position corresponds to the comb lines. To illustrate the achieved frequency precision, the time scale was transformed to frequency scale in Fig. 3.13 by interpolating the frequency intervals between the calibration peaks. The FWHM of the filtered heterodyne signal was measured to be about 1 MHz.

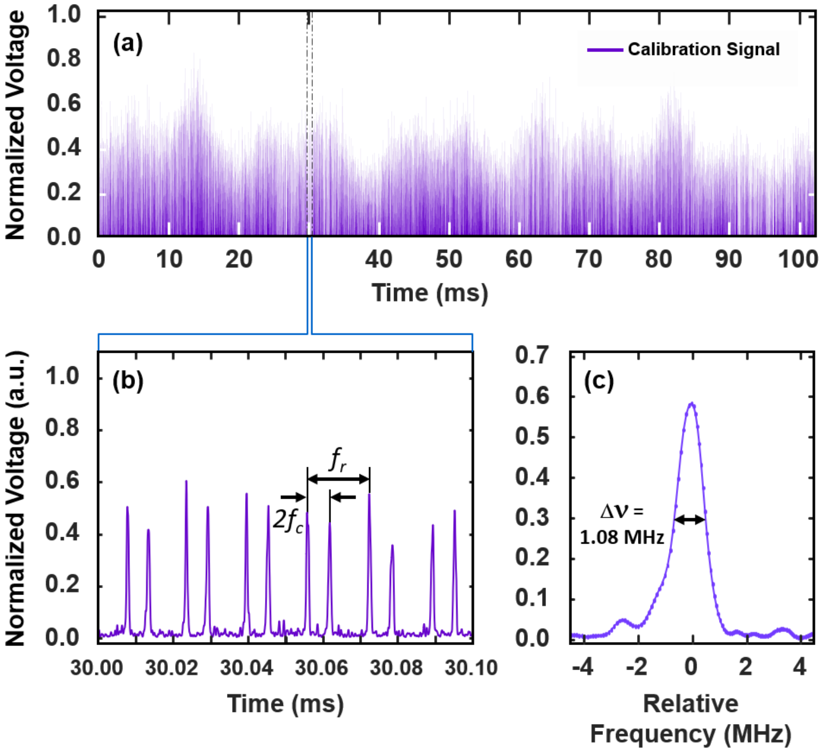

Fig. 3.13. (a). Calibration peaks referenced to the frequency comb. (b). Zoom-in view of the highlighted section of (a). Each pair of closer peaks is produced when the tuning laser frequency approaches and leaves the comb lines. (c). A further zoom-in view of (b) shows the peak spectral width, indicating the high resolution of the calibration peak. The characteristic of the filter used here is shown in Fig. 3.12. Tuning speed 40 nm/s.

The m^{th} pair of calibration peaks corresponds to the frequency sweeping amount of $\Delta\nu = mf_r$. Taking the instances corresponding to the maximum value of each calibration peak as the mark that the frequency of the heterodyne signal equals to the center of the NBF, we mapped the peaks to the instantaneous frequency tuning range, as shown in Fig. 3.14(a).

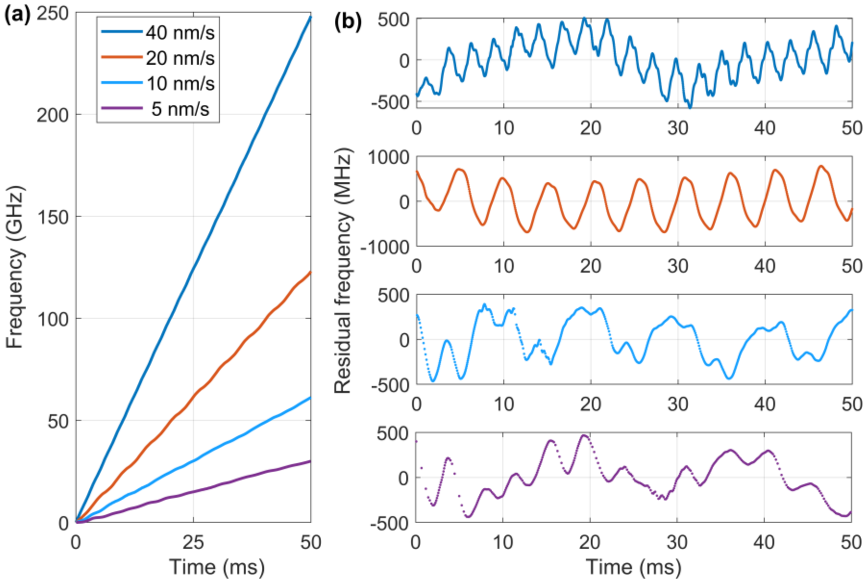

Fig. 3.14. (a). Instantaneous swept frequency of the quasi-linearly tuned laser source. (b). Residual frequencies of linear fits to (a).

Linear fits were then applied to these calibration peaks and the residual of the fit is shown in Fig. 3.14(b), illustrating quasi-periodic nonlinearity sweeping behavior of the sweeping laser with different sweeping speeds. The actual tuning speed is calculated by:

$$v_{s_{meas}} = \frac{f_r}{\Delta t} \qquad \text{Eq. 3.35}$$

where Δt is the time interval between two adjacent calibration peaks. The results are shown in Fig. 3.15.

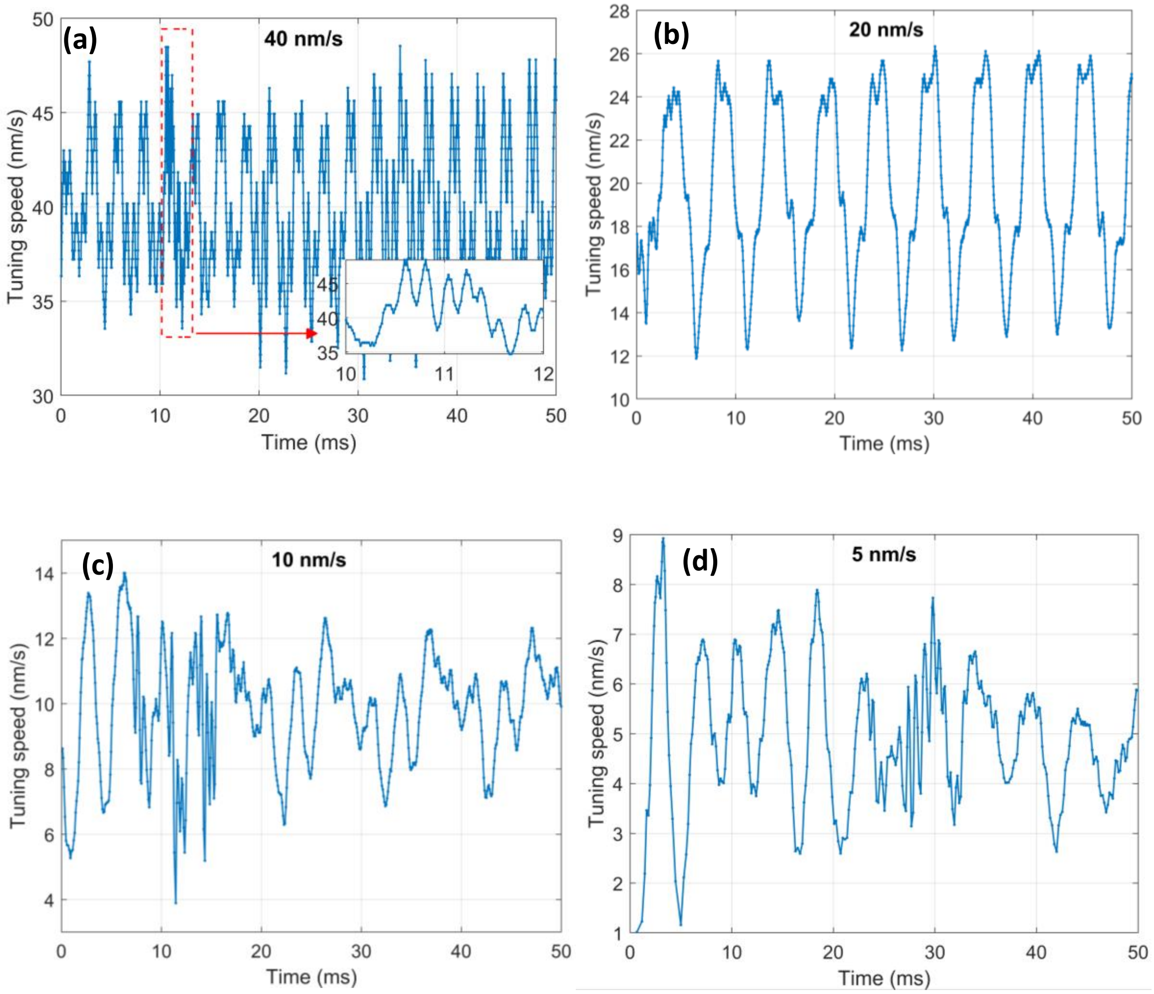

Fig. 3.15. Experimentally retrieved tuning speed for different nominal tuning speeds: (a) 40 nm/s, (b) 20 nm/s, (c) 10 nm/s and (d) 5 nm/s.

The quasi-periodic tuning behavior is highly reproduceable for different tuning speeds that we assumed it is caused by the tuning control mechanism of the ECLD tunable laser source. Since the plotted signals in Fig. 3.14 is uniformly sampled in the optical frequency domain, as described in the previous paragraph, it is easier to analyze the periodicity using optical frequency as the variable instead of time. Using Fourier transformation, the 'spectra' is shown in Fig. 3.16. It shows that the maximum period happens near 0.08 cycle/GHz for all cases, but they have different minor components.

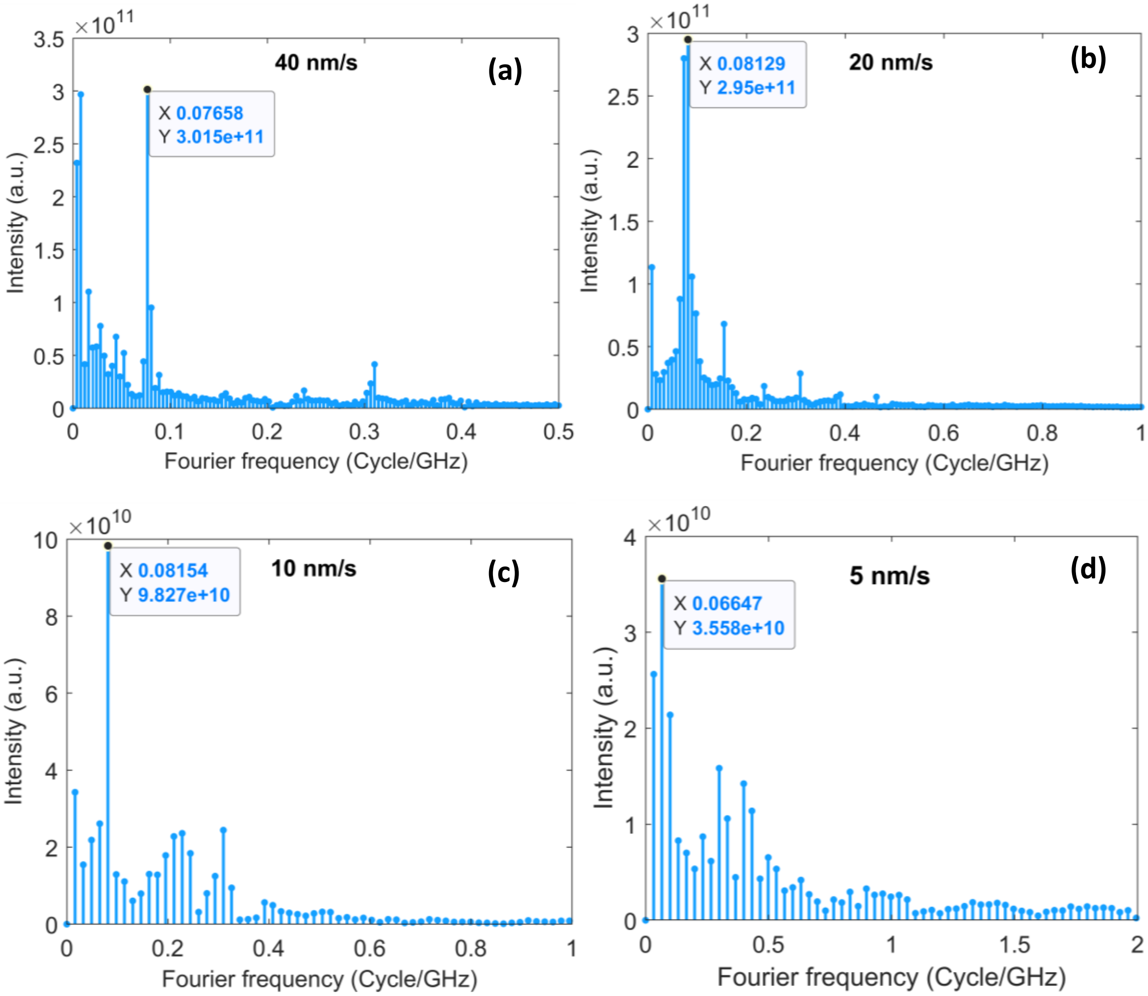

Fig. 3.16. Spectra of the nonlinear tuning of the tunable laser for different nominal tuning speeds: (a) 40 nm/s, (b) 20 nm/s, (c) 10 nm/s and (d) 5 nm/s

3.5. Conclusion

In this chapter, the proposed calibration scheme of the frequency tuning range of a sweeping laser has been presented. We firstly analyzed the spectral structure of the heterodyne signal during frequency sweeping. Different frequency components are generated between the comb lines as well as between the sweeping laser and each comb line.

The calibration is performed using filtering the heterodyne signal between a frequency comb and the sweeping laser. We characterized the filter optimized for generating high spectral resolution calibration peaks. Through theoretical analysis and simulation, we found that the selection of the filter type and bandwidth can be described in the normalized form, which is related to the bandwidth and chirp rate of the heterodyne signal. In general, filters with slow roll-off characteristic in transition band are preferable to avoid envelope distortion from the filter transfer function.

Chapter 4. Effect of Frequency Instability of Comb Lines on the Calibration Peak Envelope

As described in Chapter 2, the instantaneous frequency of the tunable laser is referenced to the comb lines by filtering the heterodyne signal. In Chapter 3, the relation between the filtered peak and the characteristic of the narrow bandpass filter (NBF) is discussed. In the previous chapters, the input signal is assumed to be an ideal linearly chirped signal. However, the phase noise of the tunable laser and the comb lines make the peak deviate from the ideal situation. In this chapter, the effect of the phase noise of the comb line on the peak shape is discussed. The Gaussian noise is studied because it forms the fundamental quantum noise of lasers. For most of lasers, the $1/f$ noise dominates at lower frequency region (i.e. longer observation time), while quantum noise is the limit at higher frequency region (i.e. shorter observation time). In the discussed frequency calibration using a frequency comb, the time for the tunable laser going through the comb lines is short (in the range of microseconds). In such short time, the $1/f$ frequency noise can be regarded as negligible. This indicates that the envelope distortion of each individual calibration peak is mainly caused by the quantum noise. Besides, the simple relation between the laser linewidth $\Delta\nu$ and the white Gaussian noise variance $2\pi\Delta\nu^2$ allows us establishing a concise relation between the laser linewidth and the calibration envelope in normalized form. Hence, as the first approach, the Gaussian noise is considered.

4.1. Model

In this section, the model for obtaining the probability density function (PDF) of the envelope of the calibration signal is built. For a linearly tuned sweeping laser, the heterodyne signal between the linear tuned laser and one of the comb lines in Eq. 3.18 can be rewritten as a linearly chirped signal:

$$S_i(t) = S_0 \exp\left[i2\pi\left(+\frac{\nu_S\, t}{2}\right)t + i\theta(t)\right] \qquad \text{Eq. 4.1}$$

where F_{cf} is the heterodyne frequency at $t = 0$, ν_S is the frequency tuning speed of the tunable laser, and $\theta(t)$ is the phase noise of the frequency comb line. For convenience of expression, let F_{cf} be the central frequency of the NBF. The impulse response of the NBF in complex form can be written as:

$$\tilde{h}(t) = h(t)\exp[i2\pi\, t] \qquad \text{Eq. 4.2}$$

where $h(t)$ is the envelope of the impulse response of the NBF. The filtered output at time t is the convolution between the input signal and the impulse response of the filter:

$$\tilde{S}(t) = \left(\int_{-\infty}^{T} + \int_{T}^{+\infty}\right)\tilde{h}(t_0)\tilde{S}_i(t - t_0)dt_0 \qquad \text{Eq. 4.3}$$

where T is a positive number that is several times larger than the rise time of the NBF and divides the integral into two sections. Since the envelope of the impulse response $h(t)$ of a stable and causal linear time-invariant (LTI) system satisfies: (1) tends to be 0 when t approaches to infinity, and (2) equals to 0 for $t < 0$, we can approximate the result of Eq. 4.3 by limiting the integral from 0 to T, and rewrite Eq. 4.3 as:

$$\tilde{S}(t) \simeq \int_0^T \tilde{h}(t_0)\tilde{S}_i(t - t_0)dt_0 \qquad \text{Eq. 4.4}$$

The effect of truncating the integral limit from Eq. 4.3 to Eq. 4.4 is analyzed in the next section. Substituting Eq. 4.1 and Eq. 4.2 into Eq. 4.5, we obtained the amplitude of the signal filtered by the NBF:

$$S(t) = S_0\left|\int_0^T h(t_0)\exp[i\pi v_S(t_0 - t)^2 + i\theta(t - t_0)]\,dt_0\right| \qquad \text{Eq. 4.5}$$

For white Gaussian phase noise, the reversal of time integration direction does not change the statistics of $\theta(t)$, so we can replace $\theta(t_0 - t)$ by $\theta(t_0 + t)$, and rewrite Eq. 4.5 as:

$$S(t) = S_0\left|\int_0^T h(t_0)\exp[i\pi v_S(t_0 - t)^2 + i\theta(t_0 + t)]\,dt_0\right| \qquad \text{Eq. 4.6}$$

The phase term in Eq. 4.7 is composed of two parts. The first phase term is the quadratic phase change due to linear tuning of the sweeping laser. The second phase term is the phase noise from the LO. It can be seen from Eq. 4.6 that the calculated envelope at given time t is only determined by the value of the integrands in the time interval from 0 to T. For Gaussian noise, the phase noise term $\theta(t + t_0)$ undergoes the same random process as $\theta(t)$ in this time interval. Thus, when we consider the statistical characteristics of the envelope distribution at given frequency position, Eq. 4.6 can be reduced to be:

$$S(t) = S_0 \left| \int_0^T h(t_0) \exp[i\pi v_S (t_0 - t)^2 + i\theta(t_0)]\, dt_0 \right| \qquad \text{Eq. 4.7}$$

However, when considering the envelope evolution, Eq. 4.6 should be used, since there exists the same integration part between two adjacent time. In the following sections, the parameters in Eq. 4.6 and Eq. 4.7 are discussed.

4.1.1 Phase Noise of the LO

For a free-running optical frequency combs, only intracavity noises are present, since there is no phase-lock-loop for stabilizing the comb lines. The fundamental origin of phase noise is quantum noise that arises from amplified spontaneous emission of the gain medium [82]. For this type of noise, the frequency fluctuation $f(t) = \frac{1}{2\pi}\frac{d\theta(t)}{dt}$ is a white Gaussian noise process $f(t) \sim N(0,2\pi\Delta v^2)$, where Δv is the 3 dB linewidth of the LO. We can simulate the evolution of the phase noise $\theta(t)$ by integrating independent Gaussian noise, which results a Brownian motion of the phase:

$$\theta(t) = \sqrt{2\pi\Delta v}\psi(t) \qquad \text{Eq. 4.8}$$

where $\psi(t)$ is a normalized Brownian motion process with zero-mean and variance $E[\psi^2(t)] = t$.

4.1.2 Narrow Bandpass Filter

Without considering the phase noise of the LO, the characteristics of the envelope of the calibration peak is related to the type of the NBF and the normalized chirp rate, which is defined in Eq. 3.31. Chapter 3 shows that the bandwidth selection is a trade-off between the width of the calibration peak and large intensity attenuation of its amplitude. Too large normalized tuning speed causes large attenuation and distortion of the calibration peak. For correct frequency-intensity converting without distortion, the bandwidth of the NBF should be chosen that its rise time is smaller than the time required for the chirping frequency to pass through the bandwidth of the NBF. In the present work, we limit the normalized tuning speed $v_{SN} \leq 1$ in order to conform the correct frequency-intensity transform condition.

For convenience of expressing the impulse response function of the NBF, we use the noise-equivalent bandwidth, which is defined as:

$$B = \frac{\int_0^{+\infty} |h(t)|^2 dt}{\left|\int_0^{+\infty} h(t) dt\right|^2} \qquad \text{Eq. 4.9}$$

It can be shown that using Eq. 4.9, the envelope of the impulse response $h(t)$ can be express as $h(t) = Bg(Bt)$, where $\int_0^{+\infty} g(x)dx = \int_0^{+\infty} |g(x)|^2 dx = 1$. Three analog filters are used in the simulation: single tuned filter (RC filter), two-stage decoupled resonant filter (RC-2 filter), and maximally flat filter (Butterworth filter). The envelopes of the impulse response of these filters are shown in Fig. 4.1.

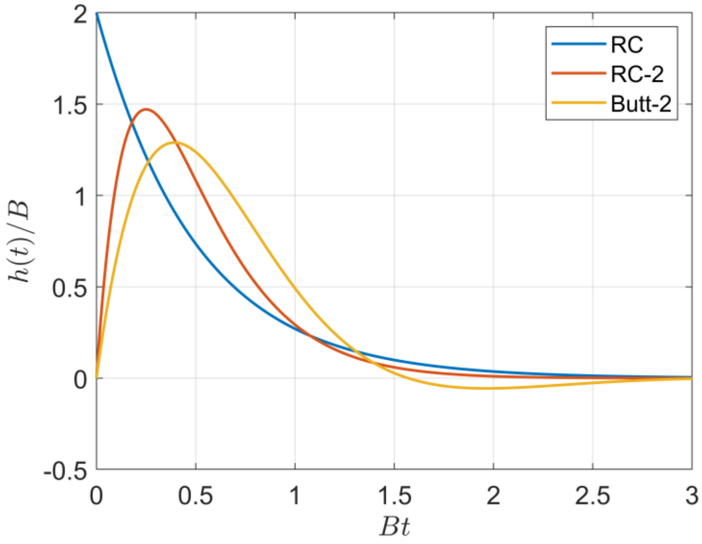

Fig. 4.1. Envelope $h(t)$ of the impulse response of NBF $\tilde{h}(t)$ used in the present work.

4.1.3 Parameterized Expression

For generality, we normalize the frequency parameters in Eq. 4.6 and Eq. 4.7, such as the linewidth of the LO, to the bandwidth of the narrow bandpass filter B. Meanwhile, we normalize the time parameters, such as the truncation time T, to the rise time of the NBF, which is proportional to $\frac{1}{B}$. By taking $T = \frac{\tau}{B}$ and introducing a normalized time scale $u = \frac{t}{T}$, we rewrite the amplitude of the filtered calibration peak in the form that is integrated within the unit time interval from 0 to 1 as:

$$S_N(u) = \left|\frac{\tau}{B} \int_0^1 h\left(\frac{u_0 \tau}{B}\right) \exp\left[\frac{i v_S (u_0 - u)^2 \tau^2}{2B^2}\right] \exp\left[i\theta\left(\frac{\tau(u + u_0)}{B}\right)\right] du_0\right| \qquad \text{Eq. 4.10}$$

Here, $S_N = S(t)/S_0$ is the normalized amplitude. Substituting the phase noise expression Eq. 4.8 into Eq. 4.10, and normalizing the linewidth of the LO and the tuning speed by taking $\Delta\nu_N = \frac{\Delta\nu}{B}$ and $v_{SN} = \frac{v_S}{B^2}$ respectively, we get:

$$S_N(u) = \tau \left| \int_0^1 g(\tau u_0) \exp\left[\frac{i v_{SN}(u_0 - u)^2 \tau^2}{2}\right] \exp\left[i\sqrt{2\pi\tau\Delta\nu_N}\psi(u + u_0)\right] du_0 \right| \quad \text{Eq. 4.11}$$

From Eq. 4.10 to Eq. 4.11, we use the property of Brownian motion that $\psi\left(\frac{\tau(u+u_0)}{B}\right) = \sqrt{\frac{\tau}{B}}\psi(u + u_0)$. It is better to use the normalized input instantaneous frequency, which is defined as $f_N = (v_S\, t)/B = v_{SN}\tau u$, instead of using time as the independent variable:

$$S_N(f_N) = \tau \left| \int_0^1 g(\tau u_0) \exp\left[\frac{i(f_N - v_{SN}\tau u_0)^2}{2v_{SN}}\right] \exp\left[i\sqrt{2\pi\tau\Delta\nu_N}\psi\left(u_0 + \frac{f_N}{v_{SN}\tau}\right)\right] du_0 \right| \quad \text{Eq. 4.12}$$

By this substitution, the shape of the calibration peak and the amplitude response of the NBF have the same independent variable, facilitating to analyze the distortion of the peak shape. For example, $f_N = 0$ and $f_N = 1$ correspond to the passband central and the bandwidth B of the NBF respectively. Similarly, the parameterized form of Eq. 4.7 can be written as:

$$S_N(f_N) = \tau \left| \int_0^1 g(\tau u_0) \exp\left[\frac{i(f_N - v_{SN}\tau u_0)^2}{2v_{SN}}\right] \exp\left[i\sqrt{2\pi\tau\Delta\nu_N}\psi(u_0)\right] du_0 \right| \quad \text{Eq. 4.13}$$

At this point, the effect of the phase noise of the LO in calibration of a tunable laser using heterodyne and narrow bandpass filter can be estimated using Eq. 4.12 and Eq. 4.13.

4.1.4 Error Sources in the Simulation

Simulations were carried out using numerical integration of Eq. 4.13 to estimate the PDF of the amplitude of the calibration signal at given frequency positions, and using Eq. 4.12 for observing the envelope evolution with respect to frequency position. The error sources in the simulation are mainly introduced by the following two aspects.

(1). The error induced by discrete time integration. In the simulation, the continuous integration was estimated by numerical integration at times $u_n = \{nT_{samping}\}_{n=1,2,\ldots,N}$, where $T_{samping} = \frac{1}{N}$ with N being the number of intervals. Eq. 4.12 and Eq. 4.13 show that when any of the parameters τ, v_{SN} and $\Delta\nu_N$ becomes larger, the numerical estimation deviates more from the continuous time integration when the time interval $T_{samping}$ is the same. This gives us a conservative estimation of $T_{samping}$ by setting τ, v_{SN} and Δv_N at the largest values that we want to observe and see the acceptable value of $T_{samping}$ that the PDF has an acceptable accuracy.

(2). The error induced by truncation of the integration time τ, i.e. the error introduced by using Eq. 4.4 to estimate Eq. 4.3. Similar to (1), we selected the value of the truncation time by setting v_{SN} and Δv_N at the largest values and select a value that produce acceptable accuracy.

Considering physical meaningful values, we observed the values in the following range: τ in [1, 5], v_{SN} in [0, 1], and Δv_N in [0, 0.5]. Taking $\tau = 5$, v_{SN}=1 and $\Delta v_N = 0.5$, the estimated PDF of the peak amplitude S_N with different integration interval d is shown in Fig. 4.2, in which an RC filter is used. We can see that when $T_{samping} < 0.01$, the error induced by numerical integration becomes negligible. The following simulations results are based on $T_{samping} = 0.005$.

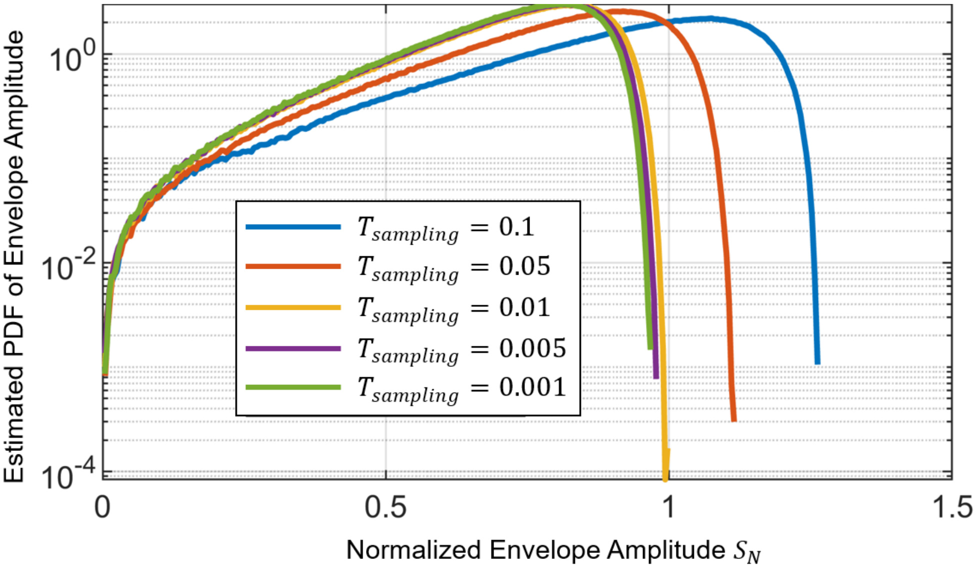

Fig. 4.2. Effect of sampling time interval $T_{samping}$. The estimated PDFs are generated by setting the parameters at the largest value required: $\tau = 5$, $v_{SN} = 1$ and $\Delta v_N = 0.5$, where the definition of the parameters is summarized in Appendix D.

Fig. 4.3 shows the simulation result with different truncation time τ and the same parameters in Fig. 4.2. We can see that when $\tau > 2$, the error induced by the time truncation can be neglected, and in the following simulation results, $\tau = 5$ is adopted.

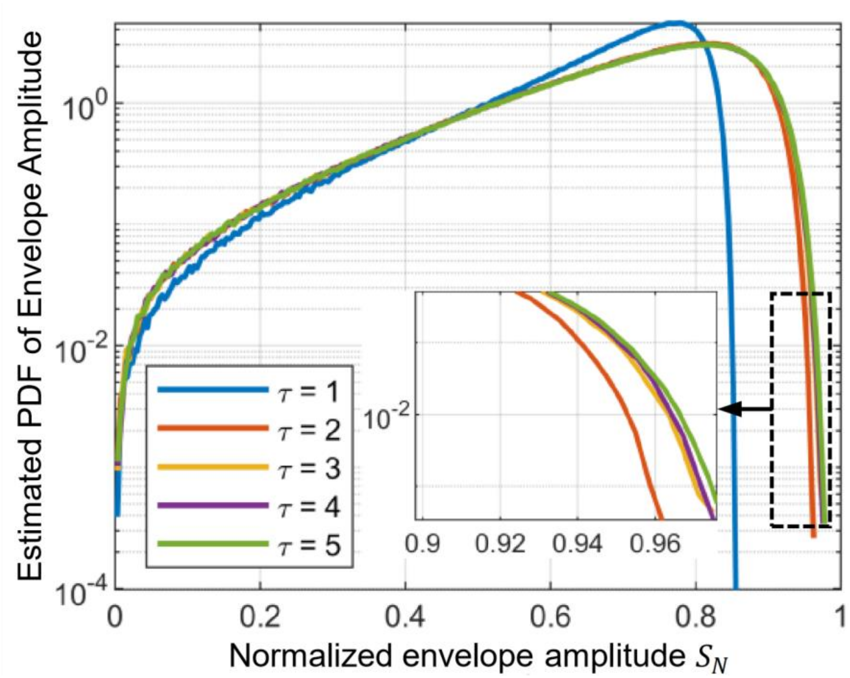

Fig. 4.3. Effect of the integration time truncation, τ. The parameters here $f_N = 0, v_{SN} = 1$ and $\Delta v_N = 0.5$, where the definition of the parameters is summarized in Appendix D.

4.2. Simulation Results

The PDF and the center of mass distribution of the peak envelope was obtained by Monte-Carlo simulations of equations Eq. 4.12 and Eq. 4.13 with 3×10^6 trials. In each trial, the phase noise $\psi(u)$ is calculated by integrating a series of Gaussian random numbers, resulting in a Brownian motion random process.

4.2.1 Probability Density Function of the Envelope

Fig. 4.4 shows the estimated PDF of the calibration peak envelope with different phase noise levels at the passband center ($f_N = 0$). The parameters were set as $\tau = 5$, $v_{SN} = 0.1$, $f_N = 0$, and a RC filter was used. When the phase noise is getting larger, the distribution is spread into a wider range, becoming more like a uniform distribution. The normalized laser line width $\Delta v_N = \frac{\Delta v}{B}$, where Δv is the laser linewidth and B is the bandwidth of the filter; the white Gaussian noise variance of the laser equals to $2\pi\Delta v^2$.

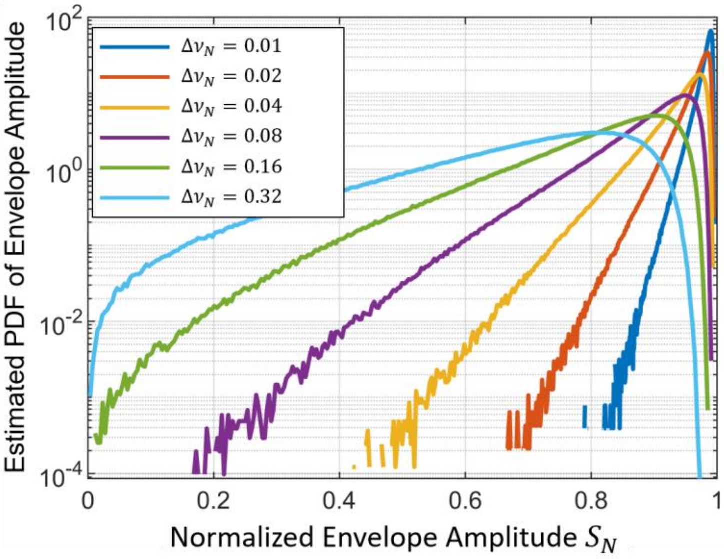

Fig. 4.4. Estimated PDF of envelope amplitude S_N at the passband central frequency ($f_N = 0$) for different phase noise levels $\Delta\nu_N$. ($\tau = 5$, $\nu_{SN} = 0.1$. The definition of the parameters is summarized in Appendix D.)

Fig. 4.5 shows the estimated PDF at different frequency positions (f_N are different). From the center to the edge of the passband, the amplitude that has the maximum PDF is decreasing. This is in accordance with the amplitude-frequency transfer function of the NBF. However, the amplitude is more uniformly distributed at the edge of the passband. Comparing Fig. 4.5 (a), (b) and (c), we can see that at smaller chirp rate, the distributions of the envelope at symmetric positions of the passband, e.g. $f_N = 2$ and $f_N = -2$, are the same. When the chirp rate becomes larger, the distribution becomes more asymmetric.

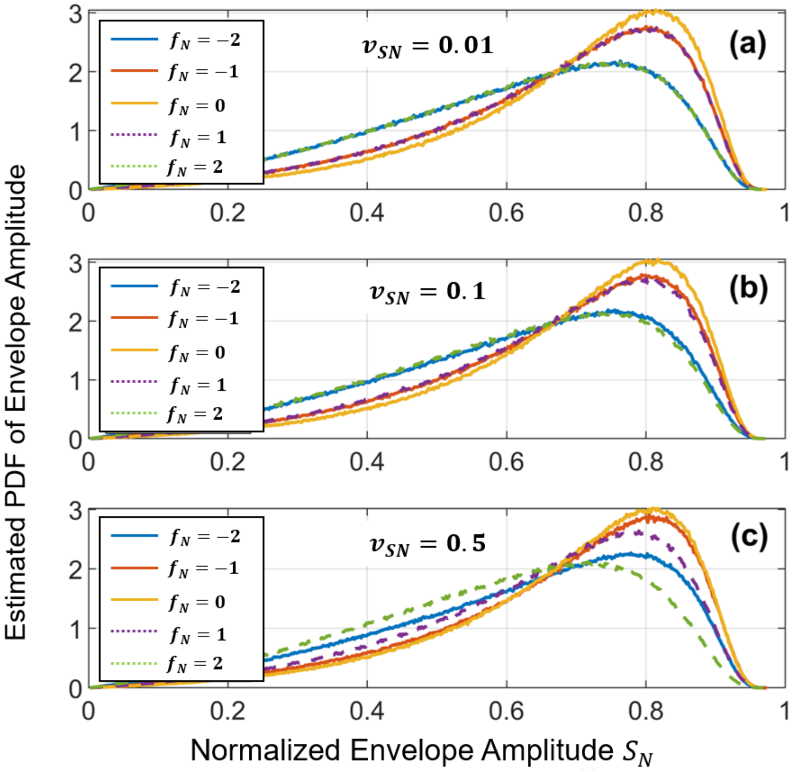

Fig. 4.5. Estimated PDF at different frequency positions f_N with different normalized tuning speed v_{SN}. (a) $v_{SN} = 0.01$. (b) $v_{SN} = 0.1$. (c) $v_{SN} = 0.5$. Parameters used are $\tau = 5$, $\Delta v_N = 0.32$ with RC filter.

The distributions by using different filters are shown in Fig. 4.6. Small difference can be seen between the RC filter and RC-2 filter. For the 2nd order Butterworth filter, it has large possibility of having values larger than 1. This result is in accordance with the analytic result in Chapter 3 that filters having sharper transition and will produce overshoot under dynamic input signal.

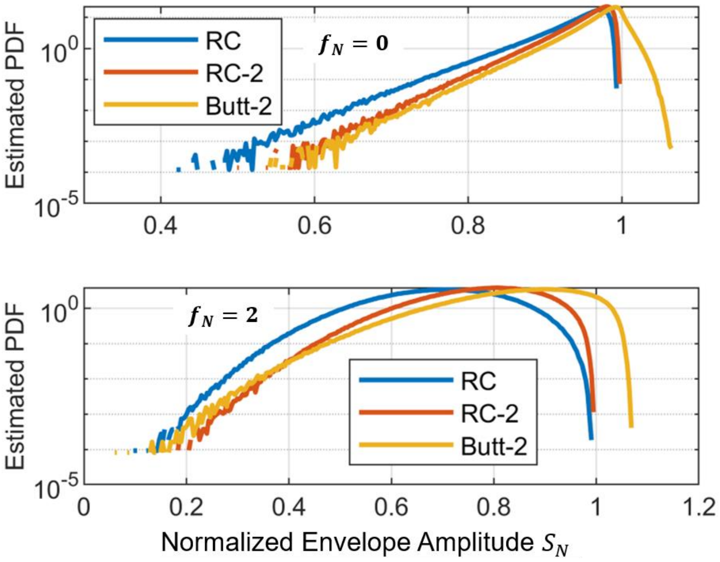

Fig. 4.6. Estimated PDF with different filters. (a) PDF in frequency position $f_N = 0$. (b) PDF in frequency position $f_N = 2$. Parameters used are $\tau = 5$, $v_{SN} = 0.1$ and $\Delta\nu_N = 0.04$.

4.2.2 Distribution of Center of Mass of the Peak

The statistical properties of the amplitude at different normalized frequency has been shown in the previous section. In this section we characterize the overall property of the filtered peak. The centroid of the peak is used to determine the instantaneous frequency of the sweeping laser in Ref. [80]. Here we define the centroid as the center of mass of the filtered calibration peak, which is fined as:

$$f_{N_c} = \frac{\int_{-\infty}^{+\infty} f_N S_N(f_N)\, df_N}{\int_{-\infty}^{+\infty} S_N(f_N)\, df_N} \qquad \text{Eq. 4.14}$$

A typical envelope of the calibration peak is shown in Fig. 4.7 showing the amplitude fluctuations.

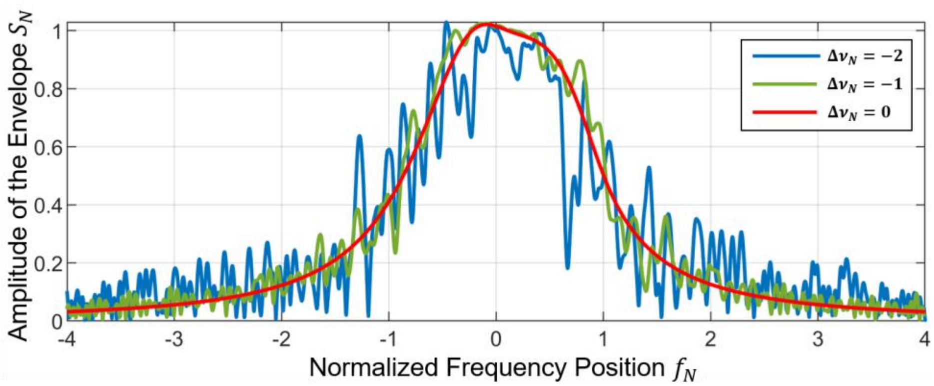

Fig. 4.7. The envelope of the filtered calibration signal with different phase noise level. Parameters used are $\tau = 5$, $v_{SN} = 0.5$ with RC-2 filter. The asymmetry profile generated without phase noise $\Delta v_N = 0$ is caused by the linear chirp of the input signal. The definition of the parameters is summarized in Appendix D.

The distribution of the center of mass of the envelope is shown in Fig. 4.8. It can be seen that both the chirp rate and phase noise affect the uncertainty. Comparing Fig. 4.8 (a) and (b), we see that at small chirp rate, the mean value of the center of mass is at the central frequency of the NBF ($f_N = 0$), while the mean value deviates from the central frequency of the filter at large chirp rate, even when the phase noise is small. This result is in accordance with the analysis in Chapter 3, that the deviation of maximum response under dynamic condition is proportional to normalized chirp rate.

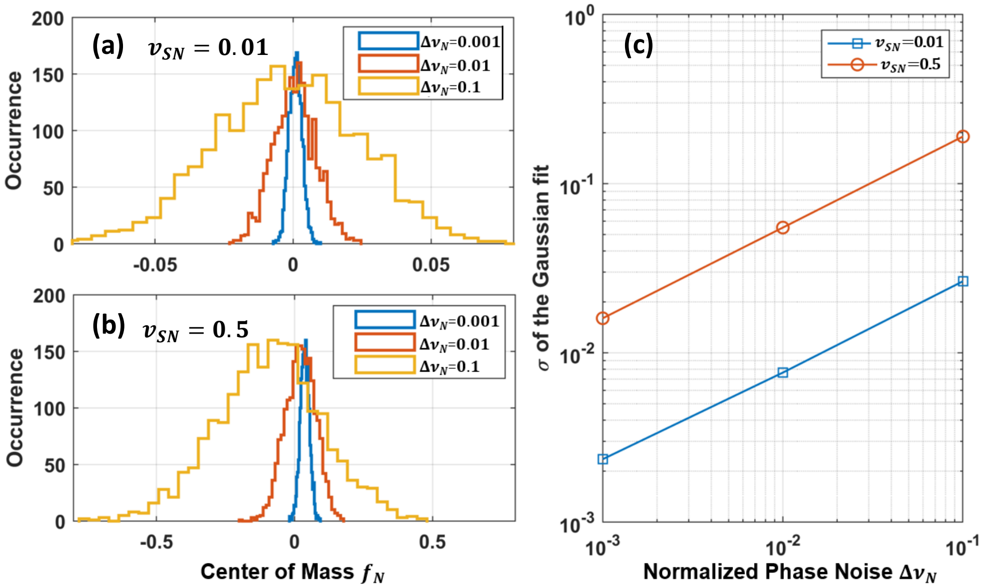

Fig. 4.8. Distribution of the center of mass of filtered calibration peak with different chirp rate. (a) and (b). Histograms of simulation result with $v_{SN} = 0.01$ and $v_{SN} = 0.5$

respectively using $\tau = 5$ and RC-2 filter. (c). The standard deviation of the Gaussian fit of (a) and (b).

Using normal distribution to fit the histogram in Fig. 4.8 (a) and (b), the standard deviation of the Gaussian fit of the distribution is shown in Fig. 4.8 (c). We find that the standard deviation of the distribution has power relationship with the normalized phase noise $\Delta\nu_N$. For $\nu_{SN} = 0.01$ it gives $\sigma = 0.088 \times \Delta\nu_N^{0.53}$, and for $\nu_{SN} = 0.5$ it gives $\sigma = 0.065 \times \Delta\nu_N^{0.54}$.

4.3. Discussion

In this modeling work, the tuning speed of the tunable laser, the phase noise level of the LO and the type of the narrow passband filter are considered. As shown in the model, the effect of these parameters is closely related to the bandwidth of the NBF, that can be expressed in normalized form. It shows that the PDF of the envelope amplitude tends to be a uniformly distributed when the phase noise is larger. At low tuning speed, the PDF distributions have little difference at symmetric frequency positions of the passband of the NBF. When tuning speed increase, these distributions become different. It shows that both the tuning speed and the phase noise level of the LO laser contribute to the center of mass distributions. For example, Gaussian fit of the center of mass distribution shows the standard deviation of $\sigma = 0.016$ and $\sigma = 0.19$ for the normalized noise level $\Delta\nu_N = 10^{-3}$ and $\Delta\nu_N = 10^{-1}$ respectively at normalized tuning speed $\nu_{SN} = 0.5$ for RC filter.

Considering the use of an RC filter with noise-equivalent bandwidth $B = 1.58$ MHz in the calibration of a tuning laser with tuning speed 10 nm/s at 1550 nm (α = 0.5), the standard deviation of the center of mass is 300 kHz for linewidth $\Delta\nu = 158$ kHz ($\Delta\nu_N = 0.1$) comb linewidth. According to Eq. 2.17, this value of frequency tuning range measurement uncertainty (300kHz) will introduce a distance relative uncertainty of 300kHz/δν, where $\delta\nu$ is the tuning range, e.g. 0.5 ppm for a tuning range of 600 GHz.

Although the analyses described above are based on analog filters, it is easy to be applied in digital filtering, especially for finite impulse response (FIR) filters, the impulse response of which are finite. This means that there is no truncation error if we take the whole impulse response as the analysis interval in (5) and (5a). For digital infinite impulse response (IIR) filters, the impulse response of the filter is truncated similarly to the analog filters.

4.4. Conclusion

We have presented in this chapter the modeling of the effect of the Gaussian phase noise of the non-stabilized comb on the filtered calibration peak envelope. The work was motivated by our experimental observation that the envelope of the filtered peak had some oscillations similar to Fig. 4.7, which would introduce uncertainty for frequency calibration. A parameterized expression of the amplitude for different frequency positions of the filter is obtained (Eq. 4.12 and Eq. 4.13). It shows that the amplitude of the envelope is a function of the normalized chirping rate of the heterodyne signal v_{SN}, the normalized phase noise level Δv_N and the type of filter used. According to the parameterized expression, the probability density function (PDF) of the amplitude and of the center of mass has been obtained through Monte-Carlo simulation method. It has showed that the probability density function of the envelope amplitude tends to be uniformly distributed when the phase noise is larger. Highly chirping rate of the heterodyne signal makes the PDFs at symmetric frequency positions of the passband of the NBF become different, even though the filter transfer function is symmetric. The deviation of the center of mass of the envelope is affected by the normalized chirping rate and phase noise level.

Chapter 5. Measurement Results

This chapter deals with the experimental system and results of absolute distance measurement. The experimental system is firstly introduced with a detailed description of individual components. The control topology and the signal processing flow that are used for the measuring system is given. At the final part, the results of absolute distance and vibration measurements using the proposed FSI scheme are presented.

5.1. Absolute Distance Measurement System

The experimental setup of the distance measurement system shown in Fig. 5.1 is based on the schematic described in Chapter 2.

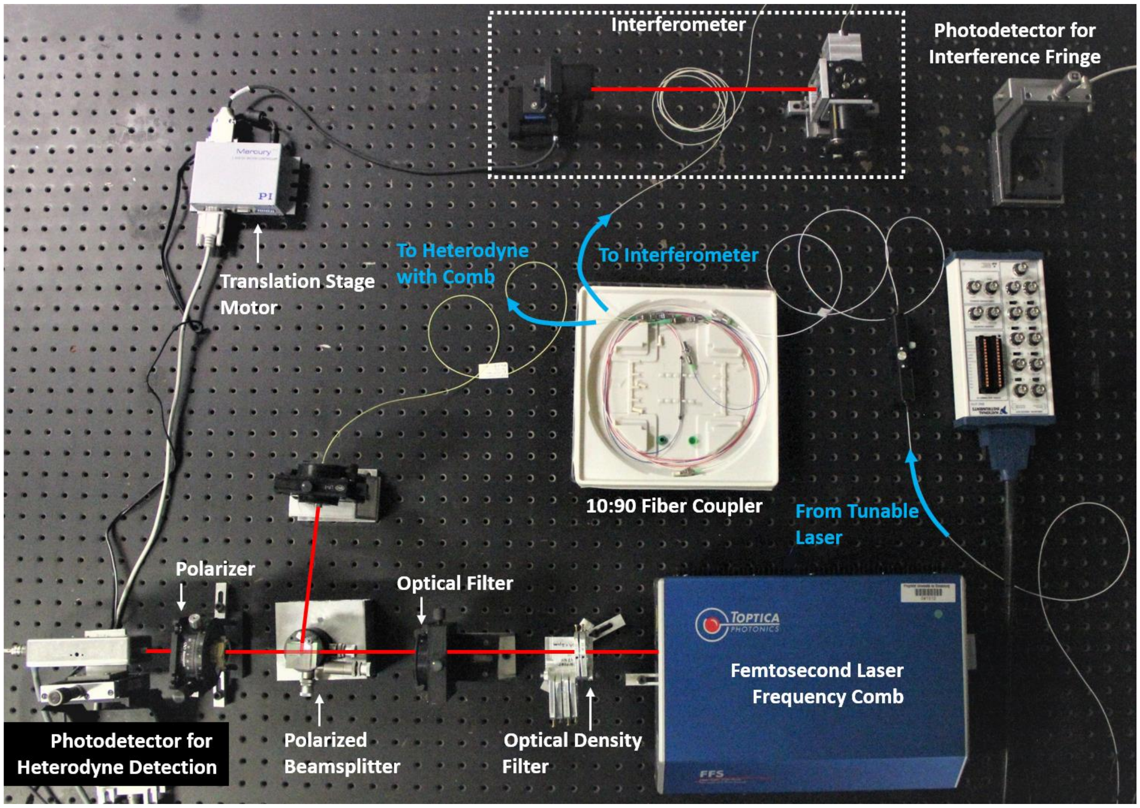

Fig. 5.1. Photograph of the comb-referenced ADM system.

The tunable laser source is an external cavity laser diode (ECLD, HP81682A) that can be continuously tuned from 1460 nm to 1580 nm without mode-hoping. The output power in the interesting wavelength range from 1520 nm to 1570 nm is 6 dBm. As measured, the polarization of the output beam does not change during frequency tuning. So that it can readily be used to heterodyne with the femtosecond laser. The output was connected to a single mode fiber (Corning SMF-28) to a fiber coupler with a power distribution ratio of 90:10. The polarization direction from the output of the fiber changes about 2π radian approximately within a day due to temperature drift. It is a slow process compared to our measurement time (in tens of minutes), even though it is better to use a polarization maintaining fiber. The polarization changes introduced by the SMF was adjusted by a polarization controller (Newport F-POL-APC).

The erbium-doped femtosecond fiber laser (FemtoFiber FFS, Toptica Photonics) has a wide spectral width around 1550 nm, with pulse repetition rate of about 76.2 MHz. The indicated average output power was 320 mW without attenuation. Such a high power was attenuated downward to tens of mW by a neutral-density filter placed just in front of the laser to avoid saturating the photodetector. To further increase the ratio of the individual comb line to the overall power, an optical filter (Semrock NIR01-1550/3) was placed followed the density filter to eliminate large number of comb lines. The 3dB passband of the optical filter was measured to be 1546 nm to 1554 nm, which is one of the limits of the tuning range in the experiments.

The frequency stability of the repetition rate of the femtosecond laser can be found in Fig. 2.7. It shows that the relative statistical uncertainty is 8×10^{-10} at the sweeping time of about 100 milliseconds, which is well below the measured distance uncertainty of 10^{-8}. The repetition frequency drifted by 1.2 kHz within the monitored 14 hours. This indicates that we can measure the repetition frequency during a short time before the laser sweeping. A frequency counter (HP 53131A) is used to record the real-time repetition frequency and sent to the control computer.

It is important to control the power from the femtosecond laser considering the weak power of individual comb lines and the overall power. A large portion of light power from the tunable laser was directed to combine with the femtosecond laser through a polarized beam splitter followed by a polarizer. Since the light from the femtosecond laser and the tunable laser are both polarized, their power for heterodyne can be finely controlled by the direction of the polarizer. A home-made circuit was used for heterodyne detection and filtering. The electronic bandpass filter therein was centered at 25 MHz with a bandwidth of 2.5 MHz.

If we want to record the entire oscillations of the filtered peaks, the sampling rate should be at least 60 MS/s in order to conform the Nyquist sampling rate. However, since we are interested in the peak envelopes, the oscillation detail should not be sampled so that we can reduce the data and ease the following signal processing. The filtered heterodyne signal was recorded by a fast digital-oscilloscope (Agilent Infiniium 54830B). The sampling mode of the oscilloscope was selected as the peak detection. This configures the oscilloscope sampling in highest speed, which in our case is 4 GS/s, as well as record the peak data in relative low rate. In this working mode, the envelope of the filtered peaks was recorded, ignoring the carrier wave under the envelope. The data recording rate was selected to be 5 MS/s to properly record the envelopes. The largest memory depth of 512 500 sampling points was used. In fact, in our setup, the memory size limits the effective tuning range of the tunable laser. The highest tuning speed of 40 nm/s was used in order to obtain as larger tuning range as possible. The above settings allow the system record data corresponding to approximate 4 nm tuning range.

The fringe signal from the interferometer was digitized by a data acquisition board (DAQ, National Instruments NI81624). The beat frequency calculated from $f_b = \frac{2nDv_S}{c}$ (Eq. 2.12) was about 33 kHz for measuring a distance of 1 m. The sampling rate of the DAQ was set to be the highest of 4 MS/s, which will generate 410 kilo-sampling-points.

The measurement distance was the length of the target arm relative to the reference arm of a Michelson type interferometer. Two retroreflectors (RRs) were used to reflect the laser beam parallel to the incoming direction. The reflected two beams then were interfered on a relative slow photodetector.

5.2. Instruments Control Flow

The control flow for the distance measurement system is illustrated in Fig. 5.2. The measurement begins from a start tuning command sent to the ECLD, meanwhile a frequency measurement command is sent to the frequency counter to measure the repetition rate of the femtosecond laser. The instruments were connected by GPIB (General Purpose Interface Bus) cables and communicate using SCPI (Standard Commands for Programmable Instruments) commands in a LabView program. When the ECLD started to tune, it delivered a TTL signal to trigger the oscilloscope and the DAQ to start sampling.

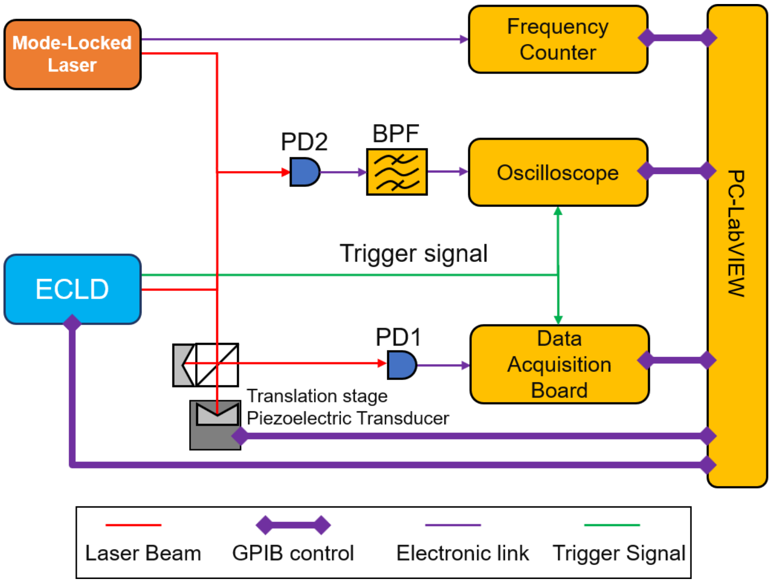

Fig. 5.2. Control flow of the ADM system. PD1 and PD2: photodetectors. ECLD: tunable external cavity laser diode. BPF: electronic bandpass filter.

All the data from the oscilloscope, the DAQ and the frequency counter were saved and then processed in the signal processing progress as described in the following section.

5.3. Absolute Distance Measurement

In the distance measurement experiment, the interferometer was placed on a vibration isolated optical table, shown in Fig. 5.3. A motorized translation stage (M-110.1DG, Physik Instrumente) was used to change the length of the measuring arm.

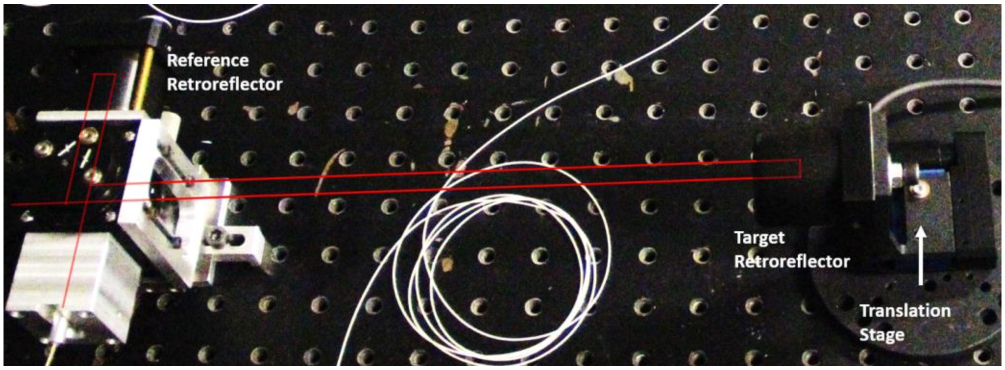

Fig. 5.3. Photography of the Michelson interferometer for the absolute distance measurement.

The accuracy of the ADM system was evaluated by comparing the displacement value of the precision translation stage with the measurement results. Monitored by a rotary encoder, the positioning stage gives a displacement accuracy better than 5 nm. The following two subsections present the measurement results using fringe counting and Fourier transform methods.

5.3.1 Results of Fringe Counting Approach

The saved data were processed in a Matlab program that follows the flow chart illustrated in Fig. 5.4. After prefiltered, both the interference signal and the calibration signal underwent peak detection. Sub-measurement was performed by selecting two calibration peaks separated by r times of the repetition rate as the beginning and the end of frequency sweeping. Therefore, the frequency tuning range for each sub-measurement was rf_r. The number of interference signal peaks within these two calibration peaks, N, was found as the integer of fringe counting. The fractional fringes, ε, of the interference signal at the beginning and the end of sub-measurement was obtained using Hilbert transform. Then the distance of the sub-measurement was obtained as:

$$D_i = \frac{c(N+\varepsilon)}{2nrf_r} \quad \text{Eq. 5.1}$$

The sub-measurement method, described in section 2.4, takes the advantage of the large number of calibration peaks (equals to the number of comb lines).

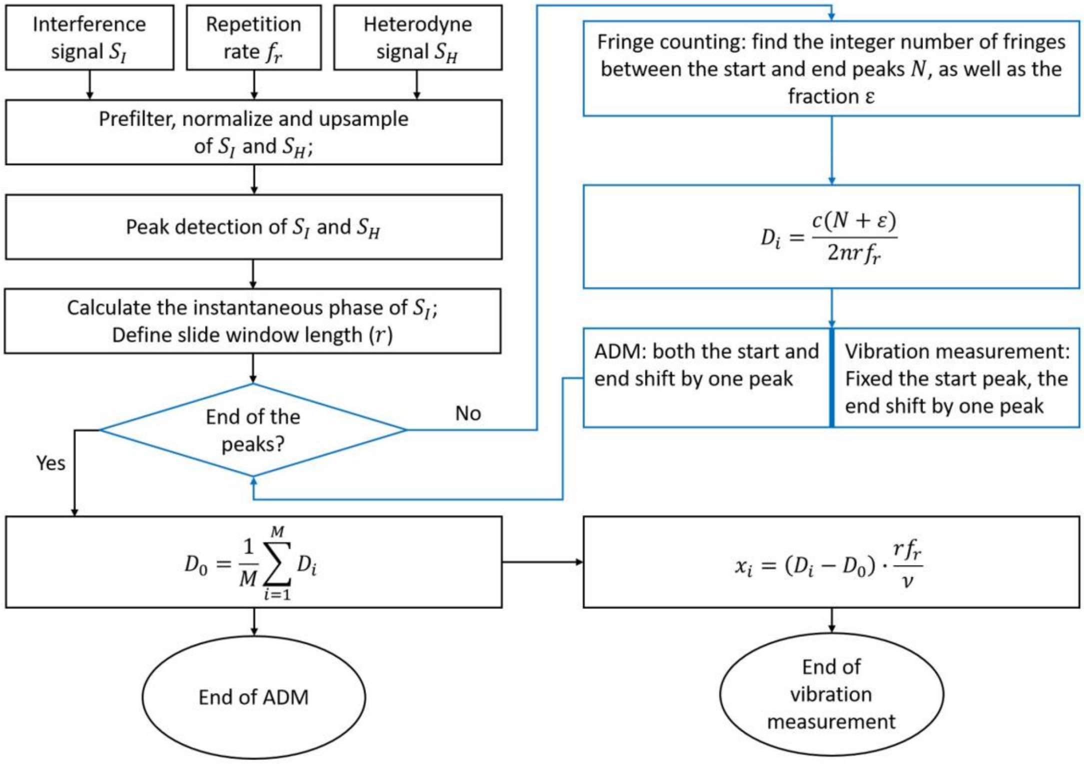

Fig. 5.4. Flow chart of signal processing using fringe counting and sub-measurement (see Fig. 2.5). The loop highlighted in blue line performs the sub-measurement.

Both the beginning and the end of calibration peaks were shifted by one peak for next sub-measurement, leading to a result of $N - r$ sub-measurements, where N is the total number of the calibration peaks. As shown in Eq. 2.18, larger r, and hence a larger tuning range, will introduce less error to the obtained distance. On the other hand, however, larger r will decrease the number of sub-measurements. Hence, a compromised number of calibration peaks in one sub-measurement should be found. Considering the frequency tuning range was determined by referencing to the calibration peaks, we can rewrite Eq. 2.18 as:

$$\sigma_D = \sqrt{\left(\frac{c\delta\varepsilon}{2nDrf_r}\right)^2 + \left(\frac{\delta r}{r}\right)^2 + \left(\frac{\delta f_r}{f_r}\right)^2} \qquad \text{Eq. 5.2}$$

The measured Allan deviation of the repetition rate f_r, as shown in Fig. 2.7, indicates that the relative uncertainty is 8×10^{-10} at the sweeping time of about 100 milliseconds. This is well below the measured distance uncertainty of 10^{-8}. Hence, the term $\frac{\delta f_r}{f_r}$ in Eq. (2) can be neglected such that the uncertainty could be expressed as:

$$\log \sigma_D = -\log r + \frac{1}{2} \log \left[\left(\frac{c\delta\varepsilon}{2nDf_r} \right)^2 + \delta^2 r \right] \qquad \text{Eq. 5.3}$$

The linear relation between the logarithmic relative statistical uncertainty of the sub-measurements and the logarithmic number of calibration peaks is shown in Fig. 5.5. The intersection of the linear regression of the data allows for the estimation of the uncertainties in the fractional phase and fractional calibration peak. As calculated, the uncertainty introduced by the fractional phase error $\delta\varepsilon$ should be less than 1.6×10^{-3} or less than 4×10^{-3} by the fractional calibration peak δr. The estimation result on our experimental setup was consistent with this calculation. The interference fringe was recorded with a sampling rate of 4 mega samples/second and 8 times of upsampling in signal processing. This corresponds to a fractional phase uncertainty of 4×10^{-4}. The FWHM (1.08 MHz) of the calibration peak (see Fig. 3.13) corresponds to a fractional peak of 0.014, in which about 15 samples were recorded.

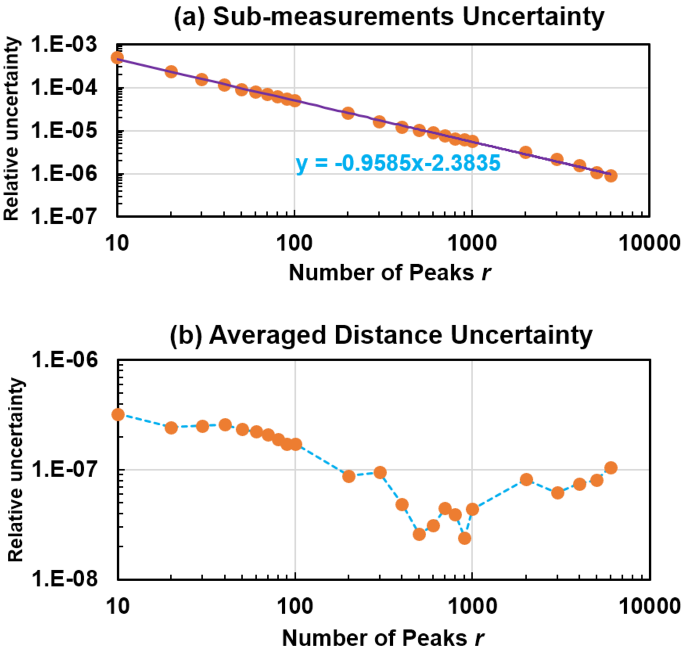

Fig. 5.5. (a). Relative uncertainty of the sub-measurements of a full scan versus the number of peaks in one sub-measurement. Orange points: experiment data. Purple line: linear fit function. (b). Relative statistical uncertainty of 7 consecutive ADM measurements versus the number of peaks r.

Figure 5(b) shows the uncertainty of 7 consecutive ADM measurements with respect to the number of calibration peaks in sub-measurement r. As r increases, the relative uncertainty firstly decreases due to the uncertainty decrease of the sub-measurements by increasing the tuning range. The uncertainty then increases at larger r, around $r = 1000$, due to the decreasing number of sub-measurements for averaging.

In a typical measurement, $N = 6629$ calibration peaks were generated corresponding to around 4 nm (~505 GHz at 1550 nm) full sweeping range. Using a sub-measurement sequence of 61 GHz (number of calibration peaks $r = 800$) and by averaging the 5829 sub-measurement results, the deviation of 5 consecutive measurements was less than ±80 nm as shown in Fig. 5.6. This leads to a relative uncertainty of 37 part per billion (ppb) at one sigma confidence level for measuring the distance of 763 mm.

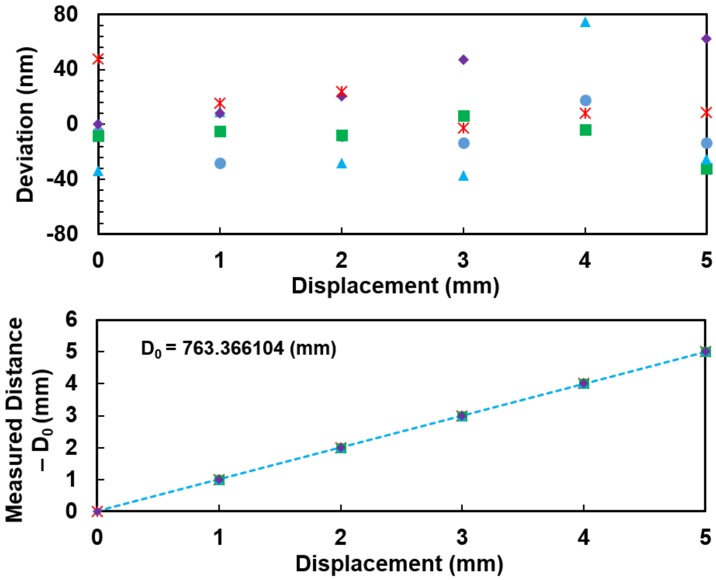

Fig. 5.6. Measurement result of 6 displacements by 1 mm from D_0. The deviation of 5 consecutive measurements is less than 80 nm.

At such high precision, a displacement of 1 μm of the target retroreflector can be well resolved, as shown in Fig. 5.7.

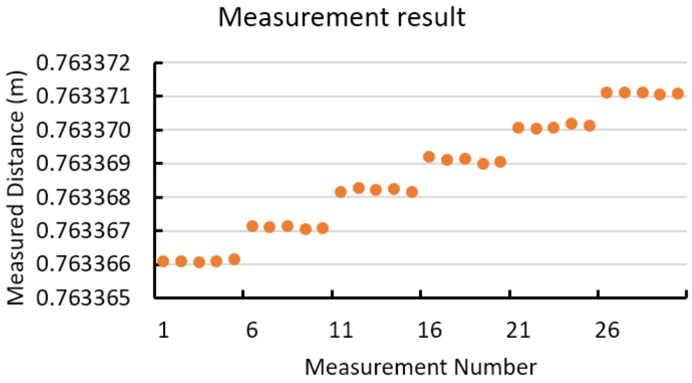

Fig. 5.7. Measurement results of displacements of the target by 1 μm up to 5 μm from absolute distance $D_0 = 0.763366104$ m.

The results show the best performance, to the best of our knowledge, among different FSI systems in terms of the relative uncertainty, as shown in Table 5.1.

Table 5.1. Results of FSI-based ADM in literature research

Absolute distance (m)	Standard deviation (±μm)	Relative uncertainty (10^{-9})	Source of reference	Tuning range (nm)	Author [Reference]
0.763	**0.028**	**37**	**Free-running comb**	**4@1550**	**Present work**
5	205	41 000	FP etalon	10@670	Medhat [83]
50	20	400	Gas cell	0.25@637	Prellinger [84]
20	4	200	Gas cell	38@1540	Dale [85]
1	0.1	100	Free-running comb	8@1560	Baumann [14]
1, 20	10, 100	5 000	Fabry-Perot etalon	0.17@633	Cabral [44]
1.195	0.25	210	Interferometer	8@836	Coe [86]
4.7	200	40 000	Fiber Interferometer	3.2@1522	Mokdad [87]
5	0.25	50	Interferometer	8@670	Stone [43]
0.8, 40	0.2, 100	250	Interferometer	10@1550	Thiel [88]

5.3.2 Results of Fourier Transform Approach

In this section, the ADM was analyzed using a Fourier transform technique described in section 2.2.1. The distance information can be obtained from the beating frequencies of the interference signal, as indicated in Eq. 2.12. The variation of the tuning speed expands the spectrum of the beat note. This can be seen in Fig. 5.8(a), which is the direct Fourier transform of the interference signal. Interpreting this spectrum in terms of OPD by scaling the frequency domain with a factor $\frac{c}{v_S}$ (v_S is the estimated averaged tuning speed) shows about 0.2 meters wide of its flat top, as shown in Fig. 5.8(b). It is a large error compared to the nominal OPD of 0.763 meters.

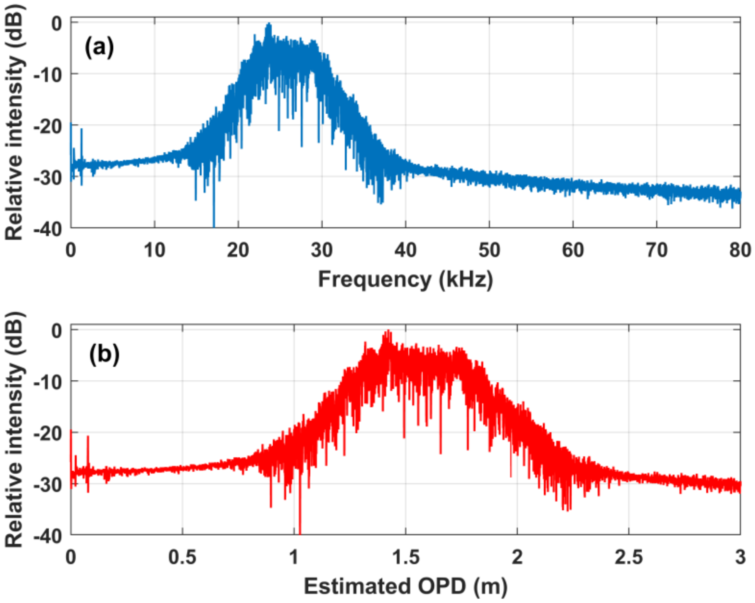

Fig. 5.8. Spectrum of the interference signal. (a). Direct Fourier transform of the interference signal. (b). Estimated OPD by scaling the frequency domain in (a) to OPD domain.

Linearization of the tuning speed was performed by resampling the interference signal at times corresponding to the calibration signal peaks. Hence, the resampled signal was uniformly sampled in the optical frequency domain where the peaks correspond to the comb lines, which is evenly spaced. Rewriting the interference signal equation Eq. 2.8 using the optical frequency as the variable and ignoring the DC components, we have:

$$i(\nu) = 2RA_1A_2\cos\left[2\pi\frac{2nD}{c}\nu\right] \qquad \text{Eq. 5.4}$$

It is indicated that if we sample the interference signal at uniform optical frequencies, its frequency is the OPD divided by the speed of light. The obtained distance (round trip) resolution is:

$$d = \frac{c}{\Delta\nu} \qquad \text{Eq. 5.5}$$

where $\Delta\nu$ is the sweeping range. Fig. 5.9 shows the spectra of the linearized interference signal. The SNR was increased to 34 dB. Without additional window function was used to apodised the recorded signal, we can see the spectral leakage of the desired point to its neighbors. The distance (in terms of OPD) resolution is about 594 μm, corresponding to the tuning range of $\Delta\nu = 504.88$ GHz (≈ 4.1 nm at 1550 nm).

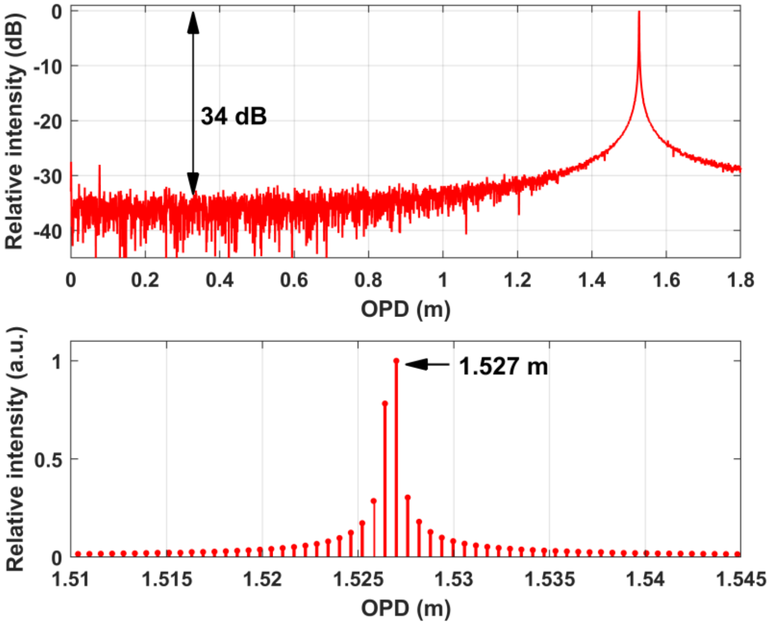

Fig. 5.9. (a). Spectra of linearized interference signal. (b). Stem plot of the interesting part of (a) to show the resolution of distance measurement.

The same raw data in

Fig. 5.7 is analyzed using FFT method, in which the OPDs was obtained from the maximal value of the spectra. Fig. 5.10 shows the result of seven positions displaced by 0.5 μm. Compared to Fig. 5.6 using fringe counting method, which can clearly resolve the distances, the measurement results here cannot be resolved because of the low resolution of FFT method. To have a resolution of 1 μm, the frequency tuning range should be larger than 300 THz!

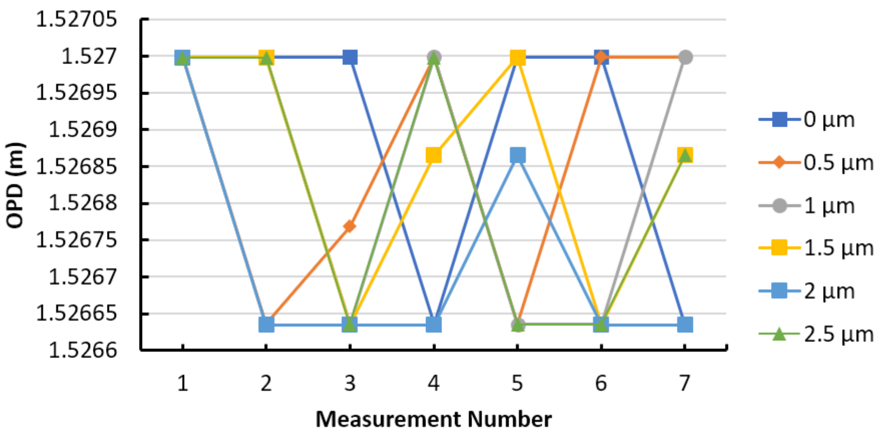

Fig. 5.10. Measurement result using direct Fourier transform method. The different series correspond to displacements of the target by 0.5 µm, 1 µm, 1.5 µm, 2 µm and

However, through zero-padding of the linearized fringe signal, the digital resolution can be increased. Figure 5.11 shows the result of using zero-padding method. Here, 386 939 zeros were added so that the overall digital resolution was 1 µm.

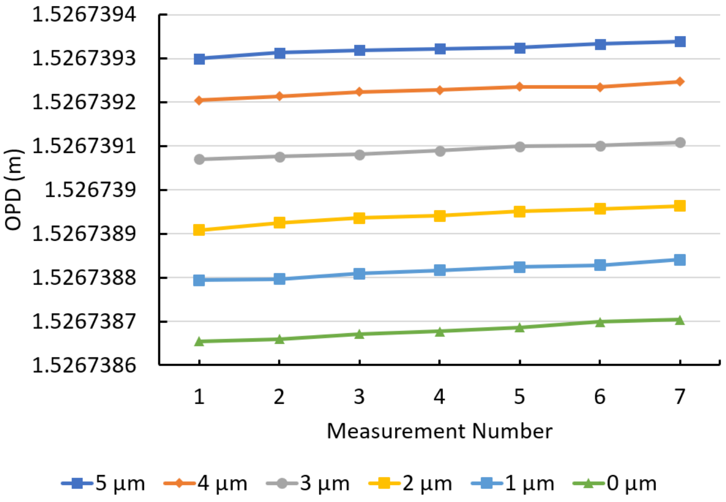

Fig. 5.11. Measurement result using zero-padding to the linearized fringe signal. Xx zeros were added so that the overall digital resolution was 1 µm.

5.4. Vibration Measurement

In section 2.3.1, we have shown that FSI-based absolute distance measurement is susceptible to the target vibration during frequency sweeping. The measured distance will be amplified by a factor of $\frac{\bar{\nu}}{\Delta\nu}$, where $\bar{\nu}$ and $\Delta\nu$ are the average frequency during sweeping and the sweeping range respectively. However, once we know the amplification factor, the drift can be compensated. In the proposed measurement scheme using comb lines as reference, since the phase change and the frequency tuning range are measured in a series of very short time intervals, it is possible to retrieve the instantaneous position of the vibrating target. Suppose in the sub-measurement shown in Fig. 5.4, the first as well as the m^{th} calibration peaks are selected. Meanwhile, the target moves from D to D+ΔD during this tuning range. The measured distance is $D' = D_0 + \Delta D \frac{\bar{\nu}}{mf_r}$, where D_0 is the central position of the vibration and $\frac{\bar{\nu}}{mf_r}$ is the amplification factor. Hence, the instantaneous distance can be retrieved by:

$$D = D_0 + \frac{mf_r}{\bar{\nu}(D^{\prime} - D_0)} \qquad \text{Eq. 5.6}$$

Where D_0 is the measured distance using the previously described method. In the vibration measurement experiment, a piezoelectric transducer (PZT) driven by a function generator was applied to introduce vibration of the target. The measurement result is shown in Fig. 5.12 (a) and (b).

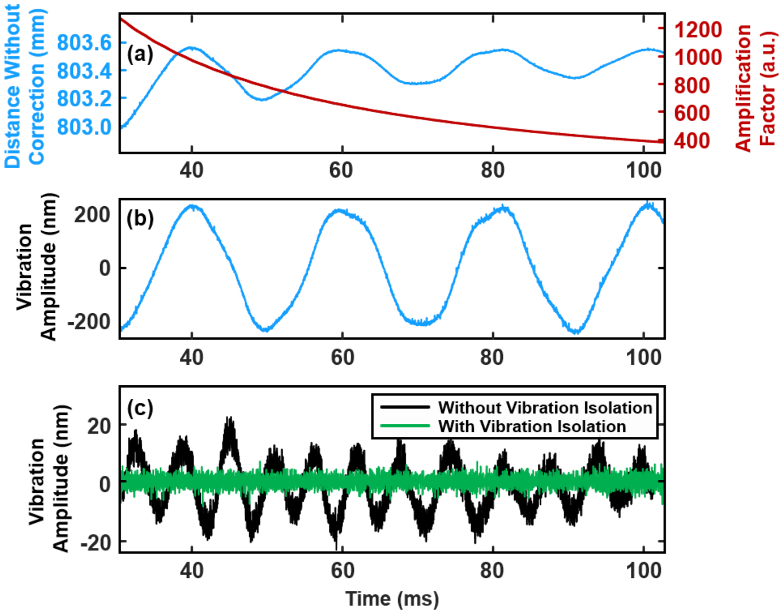

Fig. 5.12. Vibration measurement result. (a). Measured distance of a PZT-driven vibrating source and the amplification factor. As the end points of the sub-measurement shift by one calibration peak, the frequency tuning range increases by f_r, resulting in decreasing the amplification factor. (b). Retrieved vibration from (a). (c). Retrieved vibration of a target with and without vibration isolation.

The frequency of the measured vibration was 50 Hz and was in coincidence with the driving signal. In the experiment, we have tested the results of different frequencies and amplitudes available for the PZT. Results showed that we obtained the same frequency as the signal generator and the amplitude was decreased when the driving frequency increase. We assumed that the translation stage holding the retroreflector (RR) cannot response to the high frequency vibration.

We have found that when the measurement devices, such as the oscilloscope and the tunable laser benchtop, were placed on the same optical table with the measurement interferometer, a vibration of the target could be observed, as shown in Fig. 5.12(c). The measured vibration frequency was about 160 Hz. After removing all the devices generating mechanical vibration, we obtained a result that is shown as the green curve in Fig. 5.12(c).

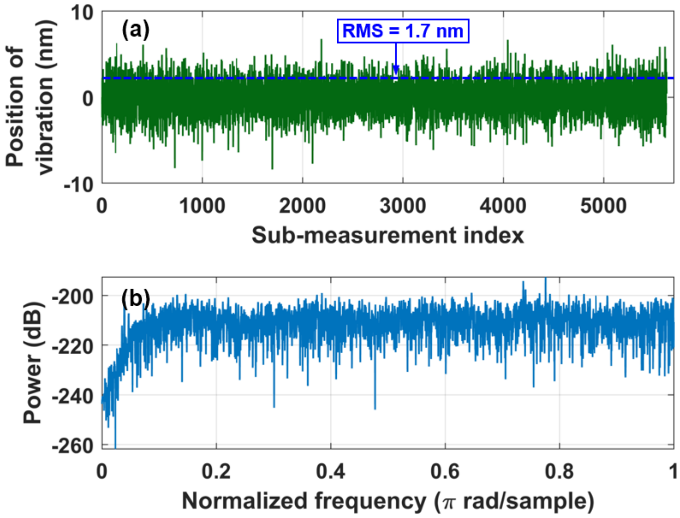

Fig. 5.13. (a) Measurement result of a vibration isolated target. (b) The PSD of (a). It shows that the measured vibration is almost white noise, which is the noise floor limiting the sensitivity.

To identify the measurement limit of vibration, the power spectral of the obtained data of a vibration isolated target has been calculated as shown in Fig. 5.13(b). White noise can be seen, expect for the relative low power in lower frequency region. Since the data are sampled corresponding to the calibration peaks, which is uniform in optical frequency domain instead of in time domain, the normalized frequency (π rad/sample) is used in Fig. 5.13(b). The RMS of the white noise was calculated as 1.7 nm, which is assumed mainly comes from the error of determining the phase of the fringe signal.

The measurable vibration frequency would be limited by the repetition rate of the comb and the sweeping speed of the tunable laser. Because we sample the position of the target by referencing the calibration peaks, which are generated in every $\frac{f_r}{v_S}$ time interval, where f_r is the petition rate and v_S is the tuning speed. Hence, the highest frequency can be measured would be $\frac{v_S}{2f_r}$. In our case, $v_S = 5THz/s$ and $f_r = 76.2$ MHz, which gives the highest measurable frequency of about 33 kHz.

5.5. Conclusion

In this chapter, we have presented the experimental results of absolute distance measurement using comb-referenced frequency sweeping interferometry. We have achieved a statistical precision of 30 nm for distances around 0.8 m, corresponding to 37×10^{-9} in relative terms based on the fringe counting signal processing method. To achieve this, a large number of the frequency calibration peaks from filtering the heterodyne signal between the sweeping laser and the comb have been derived in sub-measurements, namely length-fixed sliding window. Using sub-measurement called start-fixed sliding window, we have performed vibration measurement. A 1.7 nm sensitivity, in terms of RMS of the noise, has been achieved.

Chapter 6. Conclusions and Outlook

6.1. Conclusions

The objective of this PhD thesis was to design and implement an absolute distance metrology system with improved measuring accuracy and precision compared to the existing systems working with the similar principle. To achieve this, a frequency comb from a mode-locked femtosecond fiber laser has been employed as the frequency ruler to measure the instantaneous frequency tuning range of the sweeping laser. The modeling part of the work was described in Chapter 3 and Chapter 4. The Chapter 5 was devoted to the experimental aspects.

For the modeling work, firstly I have analyzed the design conditions of an electronic bandpass filter that is optimal for generating calibration peaks. Theoretical derivation of the output of an electronic bandpass filter, which can be modeled as a linear time-invariant system under a linearly chirped heterodyne signal, has been presented. It shows that the problem can be generalized in a normalized form, in which the parameters such as the transfer function of the filter and the sweeping speed of the tunable laser are normalized. Based on the normalized expression, simulations of various parametric values were presented. This simulation shows that filters with slow rolloff transition band outperforms filters with sharp transition band when the chirping rate of the input signal is large. Therefore, we choose Gaussian filters, which we found better for filtering the frequency calibration peaks.

Secondly, the effect of phase noise of a free-running comb lines on the frequency calibration has been modeled. This work has been carried out since the combs used in the present work are not fully stabilized. Hence, the envelope of the calibration peaks deviates from its ideal shape. The parameters such as the chirping rate, bandwidth of the filter and the Gaussian noise level were normalized similarly to the previous modeling work. Considering the short time for the tunable laser to sweep through the comb lines (in the range of microseconds), only white Gaussian noise was considered for analyzing the envelope. The reason was that the white Gaussian noise dominates the noise of the comb line at short observation time. The probability density function (PDF) of the amplitude at different positions of the calibration peaks and their center of mass have been considered. The results show that the PDF of the envelope amplitude tends to be uniformly distributed when the phase noise is larger. At low tuning speed, the PDF distributions have little difference at symmetric frequency positions of the passband of the NBF. When the tuning speed increases, these distributions become different. The simulation also shows that both the tuning speed and the phase noise level of the comb lines contribute to the distribution of the centers of mass of the calibration peaks envelope.

Based on our modeling work, we built the heterodyne detection electronics containing chirped signal filtering circuit. It has been used in the frequency calibration of the sweep laser in the absolute distance measurement system. In one of the distance measurements, we have obtained a precision of 30 nm for distances around 0.8 m, which corresponds to 37×10^{-9} relative uncertainty. The high precision is obtained thanks to the large number of the comb lines and the stability of the evenly spaced comb lines. The results well satisfy our expectation that shows the minimum relative uncertainty, to the best of my knowledge, among different works, as shown in Table 5.1.

Besides, we have found that vibration measurement of the target can be also performed taking the advantage of the dense comb lines. A high sensitivity, limited by 1.7 nm noise RMS, of vibration measurement has been achieved. This result allows us to monitor the vibration of the target, which can be a limitation for the precision of frequency sweeping interferometry.

6.2. Outlook

In this work, we have demonstrated the working principle of using a frequency comb for measuring the tuning range of the frequency sweeping laser. However, there are still some issues that need to be considered.

- The frequency comb used in this thesis is a free-running femtosecond fiber laser, with a repetition rate and offset frequency not phase locked. The measured instability of the repetition rate has shown slow drift compared to the sweeping time of the tunable laser. Therefore, we measured the repetition rate using a frequency counter before each measurement. This is not only time consuming but also the phase noise of the comb line deteriorates the calibration envelope. A stabilized frequency comb should solve this issue.
- A longer frequency tuning range of the tunable laser source should improve the measurement precision. However, in our work, the frequency tuning range was limited to about 4 nm by two factors. Firstly, we confined the spectral width of the comb using an optical bandpass filter with FWHM of 8 nm. This was necessary to increase the portion of each comb line relative to the total power input on the heterodyne detector. We did this because have obtained low signal-to-noise ratio when we used longer spectral width of the comb. Higher sensitivity and larger dynamic range of photodetector would be desired to solve this problem. Secondly, the memory of the oscilloscope we used for sampling the calibration peaks allows only

512 500 sampling points, which corresponds to about 100 ms sampling time for 5 megasamples per second sampling speed and about 4 nm for the highest tuning speed of 40 nm/s. An oscilloscope with larger memory or a high-speed data acquisition device working on continuous sampling mode would allow longer tuning range.

- In this work, both the interference signal from the measurement interferometer and the heterodyne signal for calibration were processed offline. An improvement for the future work would be using the calibration peaks as the trigger signal to directly sample the interference signal. Since the calibration peaks are evenly distributed, the interference signal would be uniformly sampled in frequency domain. This approach would automatically correct the nonlinearity tuning behavior of the tunable laser source, thus ease the burden of the data recording and processing processor and make the system faster. To measure longer distance, more filters should be used in order to sample the interference that has higher frequency.
- The fringe counting and the fractional phase measurement of the interference signal in the work was performed using offline signal processing. Hardware approaches would increase the speed.

At the end of my PhD work, all the optical components are arranged on an optical table and all the control units are individual benches instruments. There is still a long way before making the system applicable in practical applications. We have to say that depending on different applications, such as using the system in large-scale metrology, for high precision manufacturing or even in space missions, the ultimate systems will differ greatly. There are, however, some parameters that all the system shared as a metrology system, such as the volume, the mass and the measuring speed of the system. The biggest problem of the present system is its bulky volume and heavy weight coming from the individual devices. For the future potential applications, system integration and miniaturization would be the priority.

It is particularly true for one of potential application, the space scientific missions, such as satellite formation flying. Fortunately, we have seen this miniaturization becomes more and more practical. The factor limiting the size of traditional tunable external cavity laser diode (ECLD) is its tuning mechanics, especially when mode-hops free tuning over a large tuning range is required. Recently, ECLD tuned with micro-electro-mechanical systems (MEMS) are available [89], in which the external reflecting mirror is driven by MEMS. The MEMS-ECLD was thus can be assembled in a chip with butterfly package. Micro frequency combs based on whispering gallery mode are more and more mutual. These chip-scale combs have dimensions only as large as thumb nails. Looking into the future, we are optimistic to see an integrated Micro-Electro-Opto-Mechanical Systems (MEOMS) be applied in various space missions.

Appendix A. Linearity Requirement for Frequency Sweeping Interferometry

In this section, the feasibility of using Eq. 2.14 is analyzed theoretically. A model based on Mach-Zehnder interferometer is shown in Fig. A1. The frequency calibration tool can be a FP etalon, a gas cell, a frequency comb or the others that can calibrate the instantaneous frequency of the sweeping laser.

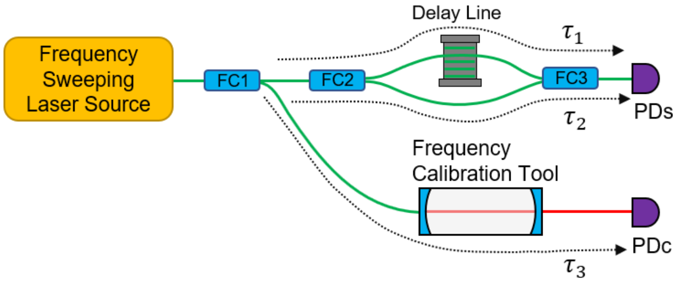

Fig. A1. Model of frequency FSI based on Mach-Zehnder interferometer. FC: Fiber coupler. PDs and PDc: Photodetector for receiving the interference signal and the calibration signal. τ_1, $\tau_2$and τ_3 are the time delays of the light paths as marked.

The instantaneous phase of the quasi-linearly swept laser can be expressed as:

$$\phi(t) = 2\pi\left(\nu_0 + \frac{1}{2}\nu_S t\right)t + \theta(t) \qquad \text{Eq. A1}$$

where ν_S is the frequency sweeping speed and $\theta(t)$ is the non-linear tuning. Denote t_0 and t_e as the start and the end time of sweeping. The difference of detected phases on the interference photodetector PDs between the end and start times is:

$$\begin{aligned}\Delta\varphi(t) &= \varphi(t_e) - \varphi(t_0) \\ &= [\phi(t_e - \tau_1) - \phi(t_e - \tau_2)] - [\phi(t_0 - \tau_1) - \phi(t_0 - \tau_2)]\end{aligned} \qquad \text{Eq. A2}$$

Substituting the optical phase Eq. A1 to Eq. A2, we have:

$$\Delta\varphi(t) = 2\pi\nu_S \cdot \Delta t \cdot \Delta\tau + [\delta\theta(t_e) - \delta\theta(t_0)] \qquad \text{Eq. A3}$$

Where $\Delta t = t_e - t_0$ is the tuning time; $\Delta\tau = \tau_1 - \tau_2$ is the difference of time delay between the two arms of the interferometer; $\delta\theta(t_e) = \theta(t_e - \tau_1) - \theta(t_e - \tau_2)$ and $\delta\theta(t_0) = \theta(t_0 - \tau_1) - \theta(t_0 - \tau_2)$ are the optical phase differences at the start and the end of sweeping.

The measured frequencies at the start and end of tuning by the calibration unit can be written as:

$$\Delta\nu_m = \nu(t_e - \tau_3) - \nu(t_0 - \tau_3) \qquad \text{Eq. A4}$$

In which the optical frequency ν is the derivative of the Eq. A1 with respect to time:

$$\nu(t) = \frac{1}{2\pi}\frac{d\phi(t)}{dt} = \nu_0 + \nu_S t + \frac{1}{2\pi}\dot{\theta}(t) = \nu_0 + \nu_S t + f_n(t) \qquad \text{Eq. A5}$$

Substitute Eq. A5 into Eq. A4 we have:

$$\Delta\nu_m = \nu_S \cdot \Delta t + [f_n(t_e - \tau_3) - f_n(t_0 - \tau_3)] \qquad \text{Eq. A6}$$

Now we can check the feasibility of the using Eq. 2.14. Substituting Eq. A3 and Eq. A6 into Eq. 2.14, the measured distance is:

$$D_m = \frac{c}{2n}\frac{\nu_S \cdot \Delta t \cdot \Delta\tau + \frac{1}{2\pi[\delta\theta(t_e) - \delta\theta(t_0)]}}{\nu_S \cdot \Delta t + [f_n(t_e - \tau_3) - f_n(t_0 - \tau_3)]} \qquad \text{Eq. A7}$$

Note that the true value of distance is $D = \frac{c\Delta\tau}{2n}$. From the above equation, we see that the error of using Eq. 2.14 is related to the nonlinear tuning behavior at the start and the end of tuning and the time delay difference between the interferometer and the frequency calibration unit.

(1). Perfectly linear tuning ($\theta(t) \equiv 0$).

In this situation, both $\delta\theta(t)$ and $f_n(t)$ equal to 0. Eq. A7 can be simplified as: $D_m = \frac{c\Delta\tau}{2n}$, which is the true value.

(2). The tuning behavior in the period of time $[t, t + \tau_1 - \tau_2]$ can be well approximated by its first order approximation.

In this situation, $\delta\theta(t_e) = \theta(t_e - \tau_1) - \theta(t_e - \tau_2) \cong \theta(t_e - \tau_2) + \dot{\theta}(t_e - \tau_2) \cdot \Delta\tau - \theta(t_e - \tau_2) = \dot{\theta}(t_e - \tau_2) \cdot \Delta\tau$ and similarly, $\delta\theta(t_0) = \dot{\theta}(t_0 - \tau_2) \cdot \Delta\tau$. So, we have:

$$\begin{aligned} \delta\theta(t_e) - \delta\theta(t_0) &= \left[\dot{\theta}(t_e - \tau_2) - \dot{\theta}(t_0 - \tau_2)\right] \cdot \Delta\tau \\ &= 2\pi[f_n(t_e - \tau_2) - f_n(t_0 - \tau_2)] \cdot \Delta\tau \end{aligned} \qquad \text{Eq. A8}$$

If the optical length of frequency calibration path is equal to the reference arm, which is true in most cases, we have:

$$f_n(t_e-\tau_3)-f_n(t_0-\tau_3)=f_n(t_e-\tau_2)-f_n(t_0-\tau_2) \qquad \text{Eq. A9}$$

Substituting Eq. A8 and Eq. A9 into Eq. A7, we obtain the measured distance as $D_m=\frac{c\Delta\tau}{2n}$. This indicates that in this situation, the distance can be obtained using Eq. 2.14 without error. All the previous work, as well as in this thesis, are in fact satisfy the conditions required of this situation.

(3). Highly nonlinear tuning. According to the Taylor expansion theory, the error of the approximation in Eq. A8 is:

$$\sigma=\frac{1}{2}\left[\ddot{\theta}(t_2)-\ddot{\theta}(t_1)\right]\Delta\tau^2=\pi\left[\dot{f}_n(t_2)-\dot{f}_n(t_1)\right]\Delta\tau^2 \qquad \text{Eq. A10}$$

where $t_1\in(t_0,t_0+\tau_1-\tau_2)$ and $t_2\in(t_e,t_e+\tau_1-\tau_2)$. Substitute Eq. A9 into Eq. A7, the error of distance is obtained as:

$$\begin{aligned}\epsilon D&=\frac{c}{4n}\frac{\left[\dot{f}_n(t_2)-\dot{f}_n(t_1)\right]\Delta\tau^2}{v_S\cdot\Delta t+[f_n(t_e-\tau_3)-f_n(t_0-\tau_3)]}\\&=D\frac{\frac{\left[\dot{f}_n(t_2)-\dot{f}_n(t_1)\right]\Delta\tau}{2}}{v_S\cdot\Delta t+[f_n(t_e-\tau_3)-f_n(t_0-\tau_3)]}\end{aligned} \qquad \text{Eq. A11}$$

Here, we take the tuning behavior of the tunable laser source used in the current work as an example to estimate the error. The tuning behavior of the tunable laser source can be found in Ref. [66], in which the wavelength sweeping can be written as the summation of some sinusoidal functions:

$$\lambda(t)=\lambda_0+v_{SN_0}\left[t-m_f\sum_{k=1}^{4}A_k\sin(2\pi f_k t+\varphi_k)\right] \qquad \text{Eq. A12}$$

where the modulation parameters are listed in Table A1.

Table A1. Characteristics of tuning parameters of 40 nm/s. $\lambda_0=1550\ nm$.

$m_f=0.15\times10^{-4}$, initial phase = $\frac{\pi}{2}$ rad.

components k	A_k	f_k (Hz)	φ_k (rad)
1	1	1512	0
2	3.6456	378	-13π/16
3	0.1671	756	-π
4	0.1418	25	-π/8

Acorrding to the above parameters, the simulation result of the instantaneous frequency and the first and second order derivatives of phase is shown in Fig. A2. According to Eq. A9 and Fig. A2(d) and (e), both the errors at the start and end of tuning is less than $\pi \times 1.5 \times 10^{12} \times \Delta\tau^2$.

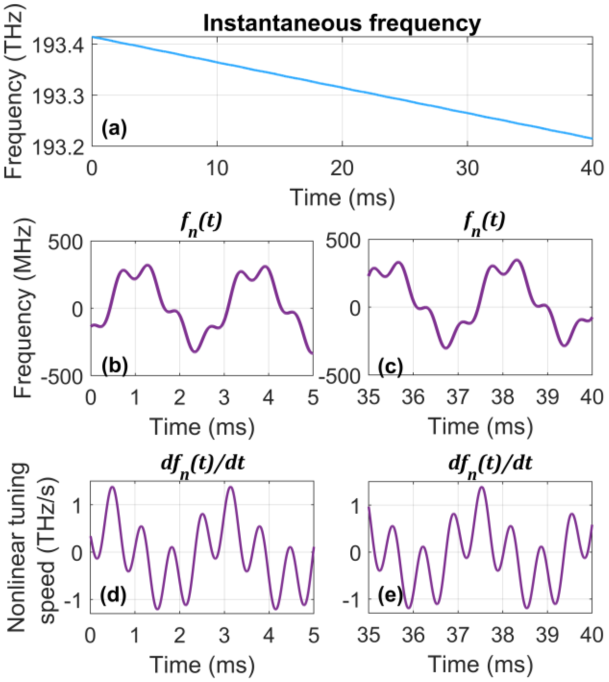

Fig. A2. Simulated nonlinear tuning of the tunable laser source according the parameters measured in year of 2007. (a): Instantaneous frequency. (b) and (c): Nonlinearity in frequency domain. (d) and (e): second order derivatives at the start and the end of tuning.

In this work, the time delay between the reference arm and the calibration path is less than 3 ns. Substitute the result in Fig. A2 to the expression of error Eq. A11, we have:

$$\epsilon D = D\frac{\frac{[\dot{f}_n(t_2) - \dot{f}_n(t_1)]\Delta\tau}{2}}{v_S \cdot \Delta t + [f_n(t_e - \tau_3) - f_n(t_0 - \tau_3)]}$$

$$\leq D\frac{[1.5 - (-1.5)] \times 10^{12} \times \frac{D}{c}}{5 \times 10^{12} \times 40 \times 10^{-3} + [500 - (-500)] \times 10^{6}} \qquad \text{Eq. 13}$$

$$= 5 \times 10^{-8} D^2$$

Appendix B. Instability of an Oscillator

Background, problem. Unwanted deviations of the oscillating frequency may be caused by aging of the oscillators, the fluctuation of power supply and the disturbance of the environment conditions such as temperature and pressure. In this section, the concept of frequency stability of an oscillator and how to characterize and measure is presented. It should be noted that, the frequency stability always involves complex stochastic process, only some key points are introduced without too detailed mathematical discussions. Further information on this topic can be found in some books and review articles, e.g. Ref. [90, 91].

The output of a practical oscillator can be expressed as a sine wave modulate by amplitude and phase noise:

$$V(t) = [V_0 + \epsilon(t)] \sin[2\pi f_0 + \phi(t)] \qquad \text{Eq. B1}$$

Where V_0 and f_0 are the nominal amplitude and frequency of the oscillator. The amplitude noise ϵ are neglected in most discussions because the degradation of the spectral purity of the oscillator frequency is smaller than the phase noise $\phi(t)$ [90]. The instantaneous frequency is the phase changing rate divided by 2π:

$$f(t) = \frac{1}{2\pi} \frac{d[2\pi f_0 + \phi(t)]}{dt} = f_0 + \Delta f(t) \qquad \text{Eq. B2}$$

with the frequency deviation:

$$\Delta f(t) = \frac{1}{2\pi} \frac{d\phi(t)}{dt} \qquad \text{Eq. B3}$$

For high quality oscillators, $\Delta f(t)$is much smaller than f_0. A more interesting quantity is the instantaneous fractional (or normalized) frequency deviation $y(t)$ because it remains unchanged after multiplication and division operations of the frequency if the multiplier and the divider is noiseless. The fractional frequency deviation $y(t)$ is defined as:

$$y(t) = \frac{\Delta f(t)}{f_0} \qquad \text{Eq. B4}$$

The $y(t)$ parameter always denoted in as a fractional of the power of ten. It allows for comparison of frequency stability for oscillators that have different nominal frequencies.

Since the frequency instability are time variances of frequency or phase, the characterization can be done in time or in Fourier frequency domain. The name ‘Fourier frequency’ here is used to distinguish the frequency of the oscillator. Both these two domains reveal the same information of the instability of the oscillator and can be mutually translated [90].

Frequency Stability Characterization in Time Domain

Time domain characterization focuses the variance of the average frequency $\bar{y}_k$ measured within a given period of time. From Eq. B3 and Eq. B4, the average frequency measured in time period $[t_k, t_k + \tau]$ can be written as:

$$\bar{y}_k(\tau) = \frac{\phi(t_k + \tau) - \phi(t_k)}{2\pi\nu_0\tau} \qquad \text{Eq. B5}$$

Since the phase $\phi(t)$ undergoes a stochastic process, the average frequency $\bar{y}_k$ is a random variable. Assuming the $y(t)$ and hence $\bar{y}_k$ has zero mean, the variance can be written as:

$$I^2(\tau) = \langle y_k^2(\tau) \rangle \qquad \text{Eq. B6}$$

where $\langle \cdot \rangle$ denotes the ensemble average of a random variable. A plot of $I^2(\tau)$ versus τ gives an entire information of the stability characterization. Meanwhile, the characterization in Fourier frequency domain can be obtained from the plot. This variance is called as 'true variance' that exists only in theory, because one cannot measure the average frequency $\bar{y}_k$ twice at the same time, and neither one can measure infinite times. The development of characterization of frequency instability took place in 1960s proposed different estimators based on the measurement for a better estimation of the true variance $I^2(\tau)$.

In practical, the average frequency can be easily related to the measurement result of counting technique. The frequency counter counts the number of events, such as the rising edge over a trigger level, of the signal under investigation within a given time τ, which is delivered by a reference or the internal clock. The measurements are performed in sequence as depicted in Fig. B1, where τ is the measuring time or the averaging time and T is the interval between two measurements. The gap between two measurements is called as the dead time.

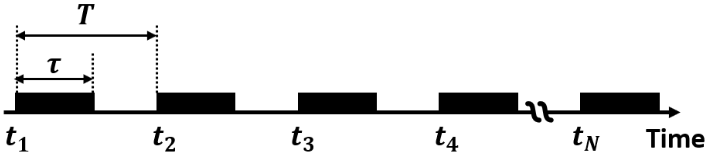

Fig. B1. Measurement sequence of the average frequency in time domain.

The sample variance similar to Eq. B6 can be written as:

$$\sigma_1^2(N,T,\tau) = \frac{1}{N}\sum_{i=1}^{N}\left(\bar{y}_i - \frac{1}{N}\sum_{j=1}^{N}\bar{y}_j\right)^2 \qquad \text{Eq. B7}$$

However, it has been found out that σ_1^2 is a biased estimator of the true variance I^2 [90]. A non-biased estimator modified from σ_1^2 is defined as:

$$\sigma_2^2(N,T,\tau) = \frac{1}{N-1}\sum_{i=1}^{N}\left(\bar{y}_i - \frac{1}{N}\sum_{j=1}^{N}\bar{y}_j\right)^2 \qquad \text{Eq. B8}$$

The commonly accepted Allan deviation is the two-sample zero-deadtime σ_2^2:

$$\sigma_y^2(2,\tau,\tau) = \frac{1}{2}\langle(\bar{y}_2 - \bar{y}_1)^2\rangle \qquad \text{Eq. B9}$$

Appendix C. Specification of Filters

Specifications of ceramic filter (Model SFE10.7A, Murata Ceramic Filter).

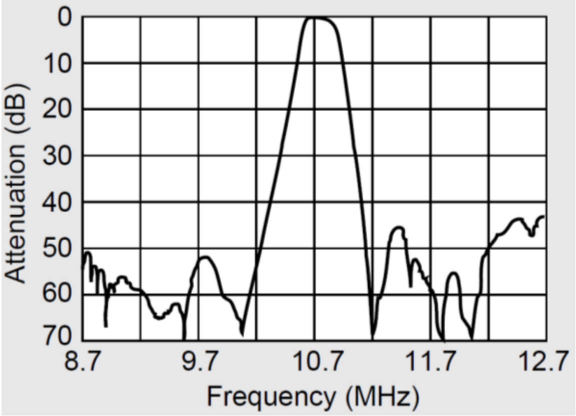

Fig. C1. Transfer function of the Ceramic filter (Model SFE10.7A, Murata).

Specifications of the 62 MHz Surface Acoustic Wave (SAW) filters (Model TB0888A, Golledge).

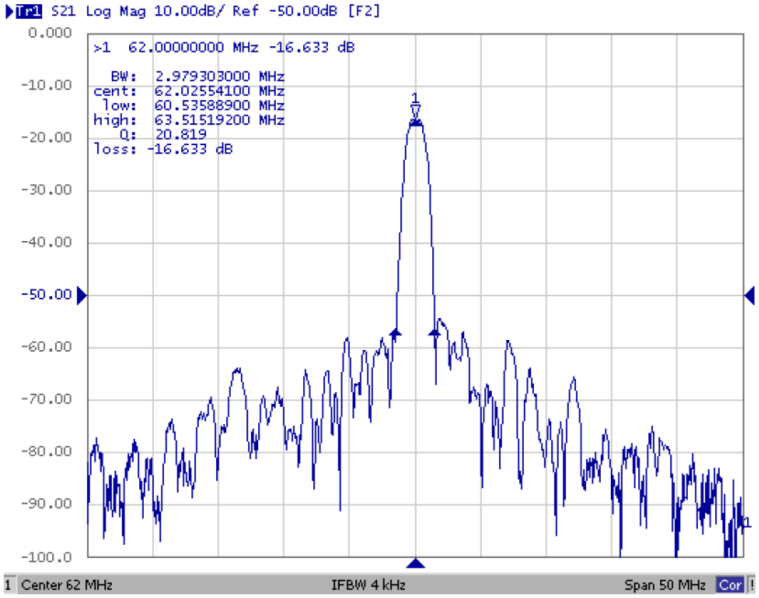

```
>1  62.00000000 MHz -16.633 dB

  BW:  2.979303000 MHz
cent:  62.02554100 MHz
 low:  60.53588900 MHz
high:  63.51519200 MHz
   Q:  20.819
loss: -16.633 dB
```

Fig. C2. Transfer function of the SAW filter (Model TB0888A, Golledge). Horizontal: $5\,\frac{\mathrm{MHz}}{\mathrm{Div}}$, Vertical: $10\,\frac{\mathrm{dB}}{\mathrm{Div}}$. Span: 50 MHz.

Appendix D. Parameters Used in the Modeling

Table A2 summarized the parameters used in the modeling of phase noise effect on calibration peak envelope in Chapter 4.

Table A2. Parameters used in modeling and simulations in Chapter 4.

Parameter	Description	Normalization	Unit
v_{SN}	Normalized chirp rate of the heterodyne signal (linear tuning speed of the sweeping laser)	$\frac{v_S}{B^2}$	-
B	Noise equivalent bandwidth of the narrow bandwidth filter.	-	Hz
$T_{samping}$	The time step in the numerical integration.	1/N	s
Δν	The linewidth of the local oscillator laser.	-	Hz
$\Delta\nu_N$	Normalized linewidth of the local oscillator laser (phase noise level).	$\frac{\Delta\nu}{B}$	-
$h(t)$	The impulse response	-	-
v_S	Tuning speed of the sweeping laser (chirp rate of the heterodyne signal).	-	Hz/s
$\psi(t)$	Standard Brownian motion process.	$\frac{\theta(t)}{\sqrt{2\pi\Delta\nu}}$	-
S_N	Envelope amplitude of the filtered peak.	-	-
T	Truncation time of the impulse response $h(t)$.	-	s
τ	Normalized truncation time.	BT	-
$\theta(t)$	Phase noise of the laser.	-	rad
u	Normalized time variable.	$\frac{t}{T} = \frac{Bt}{\tau}$	-
f_N	Normalized frequency of the narrow bandwidth filter.	$\frac{v_S t}{B} = v_{SN}\tau u$	-

List of Publication

1. Wenhui Yu, Pierre Pfeiffer, Alireza Morsali, Jianming Yang and Joël Fontaine, "Comb-referenced absolute distance and vibration measurement using frequency sweeping interferometry," Optics Letters (under consideration).

2. Wenhui Yu, Pierre Pfeiffer, Sylvain Lecler and Joël Fontaine, "Effect of Phase Noise on the Frequency Calibration of a Tunable Laser by Heterodyne Signal Filtering," IEEE Journal of Quantum Electronics, 54 (6), 1-8 (2018).

3. Wenhui Yu, Pierre Pfeiffer and Joël Fontaine, "Filter design for dynamic frequency calibration of an external cavity diode tunable laser using frequency comb", Proc. SPIE 10680, Optical Sensing and Detection V, 106800G (9 May 2018); doi: 10.1117/12.2305865;

4. Jianming Yang, Patrice Twardowski, Philippe Gérard, Wenhui Yu, and Joël Fontaine, "Chromatic analysis of harmonic Fresnel lenses by FDTD and angular spectrum methods," Appl. Opt. 57, 5281-5287 (2018)

References

[1] B. Schwarz, "Mapping the world in 3D," *Nature Photonics,* vol. 4, no. 7, pp. 429-430, 2010.

[2] S. Xu, K. Ouedraogo, L. Chassagne, S. Topcu, P. Juncar, and Y. Alayli, "Polarimetric interferometer for nanoscale positioning applications," (in English), *Rev Sci Instrum,* vol. 79, no. 12, p. 125104, Dec 2008.

[3] R. H. Schmitt *et al.*, "Advances in large-scale metrology–review and future trends," *CIRP Annals-Manufacturing Technology,* vol. 65, 2016 2016.

[4] W. Gao *et al.*, "Measurement technologies for precision positioning," (in English), *Cirp Annals-Manufacturing Technology,* vol. 64, no. 2, pp. 773-796, 2015.

[5] D. R. Richard and C. C. Stephen, *Direct-detection LADAR systems* (SPIE Press Bellingham). 2010, p. 156.

[6] M. J. Puttock, "Large-Scale Metrology," *CIRP Annals,* vol. 27, no. 1, 1978.

[7] M. Saadat and L. Cretin, "Measurement systems for large aerospace components," *Sensor Review,* vol. 22, no. 3, pp. 199-206, 2002 2002.

[8] J. Muelaner, "Large scale metrology in aerospace assembly," *5th International Conference on Digital Enterprise Technology,* 2008.

[9] K. Lau, R. J. Hocken, and W. C. Haight, "Automatic Laser Tracking Interferometer System for Robot Metrology," (in English), *Precision Engineering-Journal of the American Society for Precision Engineering,* vol. 8, no. 1, pp. 3-8, Jan 1986.

[10] P. A. Coe, "An investigation of frequency scanning interferometery for the alignment of the ATLAS semiconductor tracker," *University of Oxford,* 2001.

[11] B. Peng *et al.*, "Preparatory Study for Constructing FAST, the World's Largest Single Dish," (in English), *Proceedings of the Ieee,* vol. 97, no. 8, pp. 1391-1402, Aug 2009.

[12] R. N. Bracewell, "Detecting nonsolar planets by spinning infrared interferometer," *Nature,* vol. 274, no. 5673, pp. 780-781, 1978.

[13] Z. W. Barber *et al.*, "Characterization of an actively linearized ultrabroadband chirped laser with a fiber-laser optical frequency comb," *Opt Lett,* vol. 36, no. 7, pp. 1152-4, Apr 1 2011.

[14] E. Baumann *et al.*, "Comb-calibrated frequency-modulated continuous-wave ladar for absolute distance measurements," *Opt Lett,* vol. 38, no. 12, pp. 2026-8, Jun 15 2013.

[15] W. Zhang, H. Wei, H. Yang, X. Wu, and Y. Li, "Comb-referenced frequency-sweeping interferometry for precisely measuring large stepped structures," *Appl Opt,* vol. 57, no. 5, pp. 1247-1253, Feb 10 2018.

[16] N. Schuhler, Y. Salvade, S. Leveque, R. Dandliker, and R. Holzwarth, "Frequency-comb-referenced two-wavelength source for absolute distance measurement," *Opt Lett,* vol. 31, no. 21, pp. 3101-3, Nov 1 2006.

[17] J. Lee, K. Lee, S. Lee, S. W. Kim, and Y. J. Kim, "High precision laser ranging by time-of-flight measurement of femtosecond pulses," (in English), *Measurement Science and Technology,* vol. 23, no. 6, Jun 2012.

[18] K. Minoshima and H. Matsumoto, "High-accuracy measurement of 240-m distance in an optical tunnel by use of a compact femtosecond laser," (in English), *Applied Optics,* vol. 39, no. 30, pp. 5512-5517, Oct 20 2000.

[19] X. Lu, S. Zhang, C. G. Jeon, C. S. Kang, J. Kim, and K. Shi, "Time-of-flight detection of femtosecond laser pulses for precise measurement of large microelectronic step height," *Opt Lett,* vol. 43, no. 7, pp. 1447-1450, Apr 1 2018.

[20] H. Wu, F. Zhang, T. Liu, F. Meng, J. Li, and X. Qu, "Absolute distance measurement by chirped pulse interferometry using a femtosecond pulse laser," *Opt Express,* vol. 23, no. 24, pp. 31582-93, Nov 30 2015.

[21] H. Z. Wu *et al.*, "Absolute Distance Measurement Using Frequency Comb and a Single-Frequency Laser," (in English), *Ieee Photonics Technology Letters,* vol. 27, no. 24, pp. 2587-2590, Dec 15 2015.

[22] F. R. Giorgetta, I. Coddington, E. Baumann, W. C. Swann, and N. R. Newbury, "Fast high-resolution spectroscopy of dynamic continuous-wave laser sources," (in English), *Nature Photonics,* vol. 4, no. 12, pp. 853-857, Dec 2010.

[23] S. A. van den Berg, S. van Eldik, and N. Bhattacharya, "Mode-resolved frequency comb interferometry for high-accuracy long distance measurement," *Sci Rep,* vol. 5, p. 14661, Sep 30 2015.

[24] I. Coddington, W. C. Swann, L. Nenadovic, and N. R. Newbury, "Rapid and precise absolute distance measurements at long range," (in English), *Nature Photonics,* vol. 3, no. 6, pp. 351-356, Jun 2009.

[25] T. A. Liu, N. R. Newbury, and I. Coddington, "Sub-micron absolute distance measurements in sub-millisecond times with dual free-running femtosecond Er fiber-lasers," *Opt Express,* vol. 19, no. 19, pp. 18501-9, Sep 12 2011.

[26] J. Lee, Y. J. Kim, K. Lee, S. Lee, and S. W. Kim, "Time-of-flight measurement with femtosecond light pulses," (in English), *Nature Photonics,* vol. 4, no. 10, pp. 716-720, Oct 2010.

[27] J. M. Payne, D. Parker, and R. F. Bradley, "Rangefinder with Fast Multiple Range Capability," (in English), *Review of Scientific Instruments,* vol. 63, no. 6, pp. 3311-3316, Jun 1992.

[28] I. Fujima, S. Iwasaki, and K. Seta, "High-resolution distance meter using optical intensity modulation at 28 GHz," (in English), *Measurement Science and Technology,* vol. 9, no. 7, pp. 1049-1052, Jul 1998.

[29] C. R. Tilford, "Analytical procedure for determining lengths from fractional fringes," *Appl Opt,* vol. 16, no. 7, pp. 1857-60, Jul 1 1977.

[30] R. Dändliker, R. Thalmann, and D. Prongué, "Two-wavelength laser interferometry using superheterodyne detection," *Optics Letters,* vol. 13, no. 5, 1988.

[31] O. P. Lay *et al.*, "MSTAR: a submicrometer absolute metrology system," (in English), *Opt Lett,* vol. 28, no. 11, pp. 890-2, Jun 1 2003.

[32] D. H. Phung, C. Alexandre, and M. Lintz, "Two-mode interference measurement for nanometer accuracy absolute ranging," (in English), *Opt Lett,* vol. 38, no. 3, pp. 281-3, Feb 1 2013.

[33] H. Wu, F. Zhang, T. Liu, P. Balling, and X. Qu, "Absolute distance measurement by multi-heterodyne interferometry using a frequency comb and a cavity-stabilized tunable laser," *Appl Opt,* vol. 55, no. 15, pp. 4210-8, May 20 2016.

[34] R. J. Tansey, "An Absolute Distance Interferometer Using a Dye-Laser Heterodyne Interferometer and Spatial Separation of Beams," (in English), *Proceedings of the Society of Photo-Optical Instrumentation Engineers,* vol. 429, pp. 43-54, 1983.

[35] H. Kikuta, K. Iwata, and R. Nagata, "Distance measurement by the wavelength shift of laser diode light," *Appl Opt,* vol. 25, no. 17, p. 2976, Sep 1 1986.

[36] Z. W. Barber, W. R. Babbitt, B. Kaylor, R. R. Reibel, and P. A. Roos, "Accuracy of active chirp linearization for broadband frequency modulated continuous wave ladar," *Appl Opt,* vol. 49, no. 2, pp. 213-9, Jan 10 2010.

[37] P. A. Roos, R. R. Reibel, T. Berg, B. Kaylor, Z. W. Barber, and W. R. Babbitt, "Ultrabroadband optical chirp linearization for precision metrology applications," *Opt Lett,* vol. 34, no. 23, pp. 3692-4, Dec 1 2009.

[38] K. Knabe *et al.*, "Frequency characterization of a swept- and fixed-wavelength external-cavity quantum cascade laser by use of a frequency comb," (in English), *Opt Express,* vol. 20, no. 11, pp. 12432-42, May 21 2012.

[39] C. Lu, G. Liu, B. Liu, F. Chen, and Y. Gan, "Absolute distance measurement system with micron-grade measurement uncertainty and 24 m range using frequency scanning interferometry with compensation of environmental vibration," *Opt Express,* vol. 24, no. 26, pp. 30215-30224, Dec 26 2016.

[40] T. Pfeifer and J. Thiel, "Absolute interferometry with tunable semiconductor lasers (Geman)," (in Germany), *Technishes Messen,* vol. 60, no. 5, 1993.

[41] R. Mokdad, B. Pecheux, P. Pfeiffer, and P. Meyrueis, "Fringe pattern analysis with a parametric method for measurement of absolute distance by a frequency-modulated continuous optical wave technique," *Appl Opt,* vol. 42, no. 6, pp. 1008-12, Feb 20 2003.

[42] M. Suematsu and M. Takeda, "Wavelength-shift interferometry for distance measurements using the Fourier transform technique for fringe analysis," *Appl Opt,* vol. 30, no. 28, pp. 4046-55, Oct 1 1991.

[43] J. A. Stone, A. Stejskal, and L. Howard, "Absolute interferometry with a 670-nm external cavity diode laser," *Appl Opt,* vol. 38, no. 28, pp. 5981-94, Oct 1 1999.

[44] A. Cabral and J. Rebordao, "Absolute distance metrology with frequency sweeping interferometry," *SPIE,* vol. 5879, 2005.

[45] B. Calvel *et al.*, "High-precision optical metrology for Darwin: design and performance," (in English), *Proceedings of the 5th International Conference on Space Optics (Icso 2004),* vol. 554, pp. 501-507, 2004.

[46] G. P. Barwood, P. Gill, and W. R. C. Rowley, "Laser-Diodes for Length Determination Using Swept-Frequency Interferometry," (in English), *Measurement Science and Technology,* vol. 4, no. 9, pp. 988-994, Sep 1993.

[47] G. P. Barwood, P. Gill, and W. R. C. Rowley, "High-accuracy length metrology using multiple-stage swept-frequency interferometry with laser diodes," (in English), *Measurement Science and Technology,* vol. 9, no. 7, pp. 1036-1041, Jul 1998.

[48] G. Prellinger, K. Meiners-Hagen, and F. Pollinger, "Spectroscopicallyin situtraceable heterodyne frequency-scanning interferometry for distances up to 50 m," *Measurement Science and Technology,* vol. 26, no. 8, 2015.

[49] J. Ye, "Absolute measurement of a long, arbitrary distance to less than an optical fringe," (in English), *Optics Letters,* vol. 29, no. 10, pp. 1153-1155, May 15 2004.

[50] M. Cui, R. N. Schouten, N. Bhattacharya, and S. A. van den Berg, "Experimental demonstration of distance measurement with a femtosecond frequency comb laser," (in English), *Journal of the European Optical Society-Rapid Publications,* vol. 3, 2008.

[51] J. Jin, "Dimensional metrology using the optical comb of a mode-locked laser," (in English), *Measurement Science and Technology,* vol. 27, no. 2, Feb 2016.

[52] E. Baumann, J. D. Deschenes, F. R. Giorgetta, W. C. Swann, I. Coddington, and N. R. Newbury, "Speckle phase noise in coherent laser ranging: fundamental precision limitations," *Opt Lett,* vol. 39, no. 16, pp. 4776-9, Aug 15 2014.

[53] J. J. Talamonti, R. B. Kay, and D. J. Krebs, "Numerical model estimating the capabilities and limitations of the fast Fourier transform technique in absolute interferometry," *Appl Opt,* vol. 35, no. 13, pp. 2182-91, May 1 1996.

[54] P. Luc and P. Pierre, "Sinusoidal nonlinearity in wavelength-sweeping interferometry," *Applied Optics,* vol. 46, no. 33, pp. 8074-8079, 2007.

[55] S. A. Kingsley and D. E. N. Davies, "Ofdr Diagnostics for Fiber and Integrated-Optic Systems," (in English), *Electronics Letters,* vol. 21, no. 10, pp. 434-435, 1985 1985.

[56] S. P. Poole and J. H. Dowell, "Application of interferometry to the routine measurement of block gauges," (in English), *Pergamon Press,* 1960.

[57] A. A. Michelson, "Comparison of the international metre with the wavelength of the light of cadmium," *Astronomy and Astro-Physics,* vol. 12, 1893.

[58] K. E. Gillilland, H. D. Cook, K. D. Mielenz, and R. B. Metrologia, "Use of a laser for length measurement by fringe counting," *Metrologia,* vol. 2, no. 3, 1966.

[59] B. Chen, J. Luo, and D. Li, "Code counting of optical fringes: methodology and realization," *Appl Opt,* vol. 44, no. 2, pp. 217-23, Jan 10 2005.

[60] K. H. Bechstein and W. Fuchs, "Absolute interferometric distance measurements applying a variable synthetic wavelength," (in English), *Journal of Optics-Nouvelle Revue D Optique,* vol. 29, no. 3, pp. 179-182, Jun 1998.

[61] R. Smythe and R. Moore, "Instantaneous Phase Measuring Interferometry," (in English), *Optical Engineering,* vol. 23, no. 4, pp. 361-364, 1984.

[62] B. L. Swinkels, N. Bhattacharya, and J. J. Braat, "Correcting movement errors in frequency-sweeping interferometry," *Opt Lett,* vol. 30, no. 17, pp. 2242-4, Sep 1 2005.

[63] L. Tao, Z. G. Liu, W. B. Zhang, Z. Liu, and J. Hong, "Real-time drift error compensation in a self-reference frequency-scanning fiber interferometer," (in English), *Optics Communications,* vol. 382, pp. 99-104, Jan 1 2017.

[64] P. E. Ciddor, "Refractive index of air: new equations for the visible and near infrared," *Appl Opt,* vol. 35, no. 9, pp. 1566-73, Mar 20 1996.

[65] B. Edlén, "The Refractive Index of Air," *Metrologia,* vol. 2, no. 2, pp. 71-80, 1966/04 1966.

[66] L. Perret, "Conception et optimisation d'un télémètre laser multi-cibles à balayage de longueur d'onde," *University of Strasbourg,* PhD Thesis Fri Nov 23.

[67] C. Corning, "Corning® Single-Mode Optical Fiber," *Corning® Single-Mode Optical Fiber*.

[68] P. de Groot, "Chromatic dispersion effects in coherent absolute ranging," *Opt Lett,* vol. 17, no. 12, p. 898, Jun 15 1992.

[69] H. J. Yang, J. Deibel, S. Nyberg, and K. Riles, "High-precision absolute distance and vibration measurement with frequency scanned interferometry," *Appl Opt,* vol. 44, no. 19, pp. 3937-44, Jul 1 2005.

[70] M. Kourogi, K. Nakagawa, and M. Ohtsu, "Wide-Span Optical Frequency Comb Generator for Accurate Optical Frequency Difference Measurement," (in English), *Ieee Journal of Quantum Electronics,* vol. 29, no. 10, pp. 2693-2701, Oct 1993.

[71] R. Kallenbach, B. Scheumann, C. Zimmermann, D. Meschede, and T. W. Hansch, "Electro-Optic Sideband Generation at 72 Ghz," (in English), *Appl Phys Lett,* vol. 54, no. 17, pp. 1622-1624, Apr 24 1989.

[72] T. Kobayashi, T. Sueta, Y. Cho, and Y. Matsuo, "High-repetition-rate optical pulse generator using a Fabry-Perot electro-optic modulator," *Appl Phys Lett,* vol. 21, no. 8, pp. 341-343, 1972.

[73] M. Imrul Kayes and M. Rochette, "Optical frequency comb generation with ultra-narrow spectral lines," *Opt Lett,* vol. 42, no. 14, pp. 2718-2721, Jul 15 2017.

[74] P. Del'Haye, A. Schliesser, O. Arcizet, T. Wilken, R. Holzwarth, and T. J. Kippenberg, "Optical frequency comb generation from a monolithic microresonator," *Nature,* vol. 450, no. 7173, pp. 1214-7, Dec 20 2007.

[75] D. B. Sullivan, D. W. Allan, D. A. Howe, and F. L. Walls, "Characterization of clocks and oscillators," *NIST Publications,* 1990.

[76] D. A. Howe, "The total deviation approach to long-term characterization of frequency stability," *IEEE Trans Ultrason Ferroelectr Freq Control,* vol. 47, no. 5, pp. 1102-10, 2000.

[77] R. Fessenden, "Electric signal apparatus," *Electric signal apparatus,* Tue Jan 14.

[78] S. Jacobs, "Technical Note on Heterodyne Detection in Optical Communications," *Technical Research Group, Inc.,* Technical Note Sun Dec 30.

[79] I. T. Turbovitch, "Dynamic frequency characteristics of selectivity systems," *Radiotechnika,* vol. 12, no. 11, 1957 1957.

[80] J. Jennings, S. Halverson, R. Terrien, S. Mahadevan, G. Ycas, and S. A. Diddams, "Frequency stability characterization of a broadband fiber Fabry-Perot interferometer," *Opt Express,* vol. 25, no. 14, pp. 15599-15613, Jul 10 2017.

[81] P. Del'Haye, O. Arcizet, M. L. Gorodetsky, R. Holzwarth, and T. J. Kippenberg, "Frequency comb assisted diode laser spectroscopy for measurement of microcavity dispersion," (in English), *Nature Photonics,* vol. 3, no. 9, pp. 529-533, Sep 2009.

[82] R. Paschotta, A. Schlatter, S. C. Zeller, H. R. Telle, and U. Keller, "Optical phase noise and carrier-envelope offset noise of mode-locked lasers," (in English), *Applied Physics B-Lasers and Optics,* vol. 82, no. 2, pp. 265-273, Feb 2006.

[83] M. Medhat, M. Sobee, H. M. Hussein, and O. Terra, "Distance measurement using frequency scanning interferometry with mode-hoped laser," (in English), *Opt Laser Technol,* vol. 80, pp. 209-213, Jun 2016.

[84] G. Prellinger, K. Meiners-Hagen, and F. Pollinger, "Spectroscopically in situ traceable heterodyne frequency-scanning interferometry for distances up to 50 m," (in English), *Measurement Science and Technology,* vol. 26, no. 8, Aug 2015.

[85] J. Dale, B. Hughes, A. J. Lancaster, A. J. Lewis, A. J. Reichold, and M. S. Warden, "Multi-channel absolute distance measurement system with sub ppm-accuracy and 20 m range using frequency scanning interferometry and gas absorption cells," (in English), *Opt Express,* vol. 22, no. 20, pp. 24869-93, Oct 6 2014.

[86] P. A. Coe, D. F. Howell, and R. B. Nickerson, "Frequency scanning interferometry in ATLAS: remote, multiple, simultaneous and precise distance measurements in a hostile environment," (in English), *Measurement Science and Technology,* vol. 15, no. 11, pp. 2175-2187, Nov 2004.

[87] R. Mokdad, M. Remouche, O. Lamrous, P. Pfeiffer, and P. Meyrueis, "Irregular sampling to reduce the limitations induced by the nonlinearities in wavelength scanning," (in English), *Opt Laser Technol,* vol. 39, no. 4, pp. 828-830, Jun 2007.

[88] J. Thiel, T. Pfeifer, and M. Hartmann, "Interferometric measurement of absolute distances of up to 40 m," *Measurement,* vol. 16, no. 1, pp. 1-6, 1995.

[89] D. Anthon *et al.*, "External cavity diode laser tuned with silicon MEMS," *Ieee,* 2002 2002.

[90] J. Rutman, "Characterization of phase and frequency instabilities in precision frequency sources: Fifteen years of progress," *Proceedings of the IEEE,* vol. 66, no. 9, 1978.

[91] W. j. Riley, "Handbook of frequency stability analysis," (in English), *National Institute of Standards and Technology,* vol. 1065, 2008.

Résumé de la thèse de doctorat de Wenhui YU

Titre : Mesure de distance absolue utilisant l'interférométrie à balayage de longueur d'onde étalonnée par un peigne de fréquences

Unité de Recherche : ICUBE, Equipe Instrumentation et Procédés Photoniques

Directeur de thèse : Pierre Pfeiffer, Maître de Conférences HDR à Université de Strasbourg

Co-directeur: Joël Fontaine, Professeur à l'INSA de Strasbourg

1. Introduction

La connaissance de la distance absolue avec une grande résolution est une nécessité dans maintes applications comme le calibrage de l'instrumentation, la construction de télescopes, la fabrication de précision et le vol en formation de satellites. Selon la technique mise en œuvre, d'autres grandeurs physiques comme les vibrations, l'indice de réfraction peuvent être dérivées de la mesure de distance. L'interférométrie laser classique permet d'atteindre une précision du nanomètre, l'intervalle de non ambiguïté étant limité à la moitié de la longueur d'onde. Ainsi l'interférométrie avec un seul laser est la technique de prédilection pour atteindre la précision nanométrique pour des déplacements ou des systèmes ayant une précision meilleure que le nanomètre. Différentes approches comme l'interférométrie multi longueurs d'onde [1,2], l'interférométrie par balayage de fréquence sont l'objet de recherche pour mesurer des distances absolues (ou ADM pour *Absolute Distance Measurement*) hautement résolues. L'interférométrie par balayage de fréquence (FSI pour *Frequency Sweeping Interferometry*) a ses atouts propres [3-5]. Elle permet de réaliser des mesures même en cas de coupure du faisceau et cela dans des temps très courts dépendant de la vitesse de balayage du laser. Celle-ci peut atteindre 100 nm/s pour des lasers accordables basés sur la rotation du miroir ou du réseau de diffraction avec un entraînement moteur et, dans le cas de micro systèmes electro-mécaniques du type MEOMS en résonance des plages de 8 nm sont réalisables avec une fréquence de 1kHz. La fréquence de la source de lumière est continument syntonisée sur une plage de longueur d'onde donnée. La technique utilise une cible référence et une cible mesure. Les fréquences des signaux de battement diffèrent par $\Delta f = v_b \tau$, où v_b et τ sont la vitesse de balayage et la différence de temps de parcours. Ainsi le signal de battement entre le faisceau réfléchi par la cible et le réflecteur de référence va former le signal hétérodyne. Connaissant la vitesse de balayage et en mesurant le signal de battement, la différence de temps de parcours et par conséquent la distance, peuvent être dérivées. Avec un laser accordable large bande de la dizaine de nanomètres, une grande résolution peut être atteinte.

En pratique, pour des lasers accordables, la fréquence est syntonisée avec des non-linéarités causant des changements de fréquences. Différentes méthodes ont été proposées pour linéariser la vitesse de balayage. La première méthode est basée sur un interféromètre auxiliaire de longueur connue avec une grande exactitude. Une autre technique est basée sur un étalon Fabry-Perot pour calibrer la plage de balayage [5]. Ces deux techniques sont confrontées au problème de l'instabilité du chemin optique (Optical Path Difference ou OPD) de l'interféromètre de référence ou intervalle spectral libre (Free Spectral Range ou FSR) de l'étalon dû à un changement des conditions environnementales. Les raies d'absorption atomiques ou moléculaires constituent une source de calibrage plus stable. Cependant la largeur à mi-hauteur de la raie d'absorption est relativement large (une dizaine de GHz) et le nombre de raies est limité. De ce fait, le référencement de la fréquence du laser accordable sur les raies d'absorption introduit une grande incertitude.

La dernière décennie a vu un rapide développement des applications utilisant les peignes de fréquences générés par les lasers femtosecondes [6,7]. Comme règle de fréquences large bande, ils constituent une manière élégante pour mesurer la fréquence avec une précision sans précédent, avec un accès aisé. Le peigne de fréquence a été implémenté pour stabiliser et bloquer la phase des lasers en ADM utilisant l'interférométrie à plusieurs longueurs d'onde. Il était logique d'implémenter un peigne de fréquences pour calibrer la fréquence instantanée d'un laser accordable et d'étudier les performances d'un système de mesure de distance absolue à balayage de fréquences calibré par un peigne de fréquences.

Objectif de la thèse

Afin de résoudre les problèmes de balayage non linéaires ou le calibrage de la plage de balayage instantanée du laser accordable en FSI, différents outils de calibrage en fréquence sont nécessaires. Il a été rapporté dans la littérature, que même avec un excellent contrôle de la température, de l'humidité et de l'isolation, il est difficile de maintenir les interféromètres de références à des précisions meilleures qu'une partie par million (ppm, i.e. 10^{-6}) sur une journée. Par contre un peigne de fréquences généré par un laser femto peut être stabilisé à 10^{-16}, permettant d'atteindre des mesures de distance avec une incertitude nettement meilleure. Dans un premier temps le peigne de fréquences n'a pas été stabilisé mais, en contrepartie, nous mesurons la fréquence de répétition pendant les mesures. Les effets de bruit de phase sur les raies du peigne de fréquence sont analysés. Ce bruit de phase du peigne de fréquence est la résultante de deux phénomènes présents dans le laser femto. La fréquence ν d'une raie du peigne peut être exprimée par $\nu = f_0 + Nf_r$ où f_0 est la fréquence d'offset de l'enveloppe, N un entier et f_r la fréquence de répétition du laser. Le premier est issu d'une dérive lente de la fréquence d'offset de l'enveloppe et est liée aux dérives thermiques. Le deuxième est liée à la stabilité de la fréquence de répétition du laser qui peut fluctuer avec chaque impulsion. Le référencement en temps réel de la fréquence de répétition sur le temps standard garantit une précision à long terme. L'objectif principal de cette thèse consiste à intégrer un peigne de fréquence comme source de calibrage dans le FSI afin d'augmenter la précision sur un temps de balayage court. A cette fin les points suivants ont été étudiés:

- Optimisation du filtre du signal hétérodyne entre le laser accordable et le peigne de fréquences.
- Linéarisation de la source de balayage à partir du peigne de fréquences.
- Implémentation d'une technique de sous-mesures dérivée à partir d'une seule acquisition afin d'augmenter la résolution.
- Traitement du signal pour l'ADM et incertitude de l'analyse.
- Application à la mesure de vibrations.

2. Résultats

2.1. Système de mesure proposé

La figure 1 montre le système ADM proposé. La source de lumière, une diode laser à cavité externe (ECLD pour *External Cavity Laser Diode*) a été syntonisée de manière quasi linéaire. Afin de calibrer la fréquence instantanée de l'ECLD, une portion de lumière a été utilisée pour réaliser l'hétérodynage avec un peigne de fréquences généré par le laser femtoseconde à blocage de modes sans asservissement. Le laser femtoseconde délivre des impulsions de 100 fs avec une fréquence de répétition de 76 MHz. Le signal hétérodyne qui contient aussi bien les signaux de battement entre les raies du peigne que les fréquences résultants du battement entre les raies du peigne et la fréquence de répétition du laser de balayage est détecté par un amplificateur à photodiode rapide (PD2). Le signal hétérodyne est ensuite filtré par un filtre passe bande à bande étroite (BPF, bande passante ≈ 2 MHz, centré à 25 MHz). Les pics de signal sont générés lorsque le signal hétérodyne est égal à la fréquence centrale f_{cf} du filtre passe bande. Un oscilloscope rapide en mode détection de crête enregistre les pics de calibrage. Les pics représentent les marqueurs temporels correspondants à la fréquence du laser de balayage$\nu_T = \nu_n \pm f_{cf}$, où ν_n et f_{cf} sont respectivement les fréquences des raies du peigne et la fréquence centrale du BPF. La plage de balayage est obtenue par simple comptage du nombre de pics de calibrage (divisé par deux) et multiplié par la fréquence de répétition f_R. Il est à noter qu'en réduisant sa bande passante, le filtre passe bande augmente le rapport signal sur bruit du signal hétérodyne. Ce point est important, sachant que la puissance d'une raie du peigne est très faible et n'excède pas quelques dizaines de nanowatts. A ce niveau, différents aspects sont à considérer. En effet la puissance du signal lié à la fréquence de répétition du laser est très importante et conduit rapidement à la saturation du détecteur. Trois options se présentent. Soit on ne travaille qu'avec une partie spectrale du signal femto en intégrant un filtre, soit on travaille sur toute la bande spectrale du laser femto après avoir atténué le signal ou en exploitant le signal de la cavité femtoseconde avant amplification.

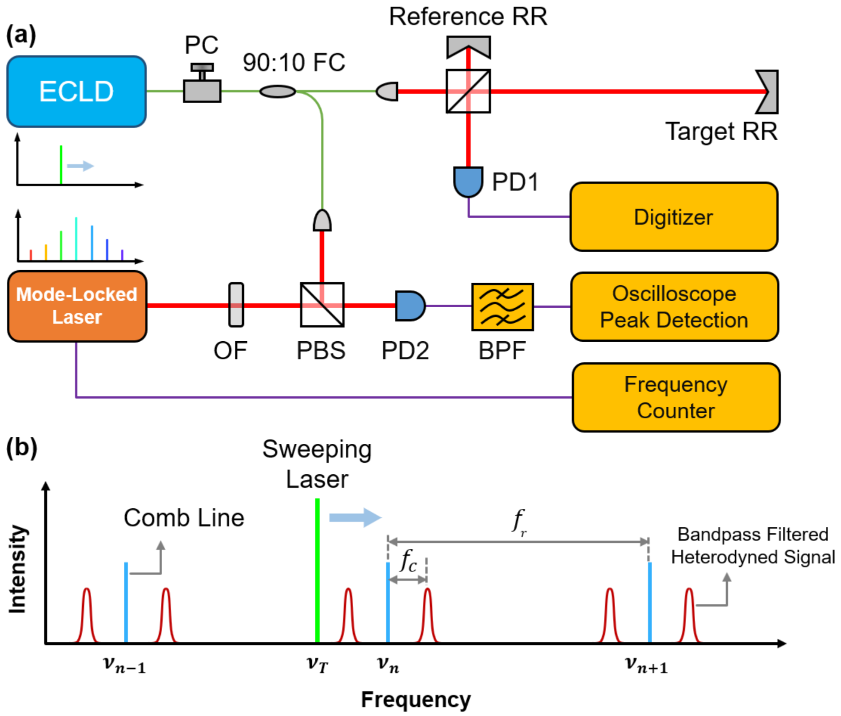

Figure 1. (a). Dispositif de mesure. Une portion de la lumière du laser accordable (ECLD) permet de faire l'hétérodynage avec un peigne généré par un laser femtoseconde. Le signal est envoyé dans un filtre passe bande à bande étroite (BPF) puis vers l'oscilloscope. Lorsque la fréquence du signal hétérodyne se trouve dans la bande passante du filtre, un signal crête est généré comme marqueur de calibrage de la fréquence du laser accordable. La fréquence de répétition du laser femto est mesurée par un compteur de fréquence. **(b).** Illustration des positions de la fréquence du laser accordable, des raies du peigne et du signal hétérodyne filtré par le BPF. PC: contrôleur de polarisation. FC: coupleur à fibre optique. RR: rétro-réflecteur. PD1 et PD2: détecteur à photodiodes. OF: filtre optique. PBS: Cube séparateur polarisé. f_{cf}: fréquence centrale du BPF. f_r: fréquence de répétition du laser femto (fréquence de séparation des raies du peigne).

Nous avons fait le choix de filtrer une partie du signal femto de manière à avoir davantage de puissance dans les raies ce qui se traduit par un signal hétérodyne plus puissant et par conséquent un rapport signal sur bruit plus important. Dans la littérature les meilleurs résultats ont été obtenus en diffractant par un réseau le signal femtoseconde avant de faire l'hétérodynage avec le signal de balayage. Malgré cette sélectivité du réseau, un rapport signal sur bruit de 30 dB n'a pu être dépassé.

2.2. Optimisation du filtre

Les pics de calibrage sont obtenus après filtrage avec un filtre passe bande à bande étroite du signal hétérodyne résultant du battement entre le peigne de fréquences et le laser accordable. La question de l'optimisation du filtre se pose. En effet prendre un filtre avec une bande étroite permet d'augmenter la résolution fréquentielle du système mais va introduire une atténuation plus importante pour des vitesses de balayage élevées et par conséquent réduire le rapport signal sur bruit. En mesure de distances absolue et en particulier pour de grande distances, il est important d'exécuter la mesure rapidement, de préférence sur une durée inférieure à la centaine de millisecondes de manière à éviter la fluctuation du chemin optique en fonction de la température, de l'hygrométrie et de la pression. Différents aspects sont à considérer comme la bande passante du filtre, le taux d'ondulation dans la bande passante, l'atténuation de la bande d'atténuation, la pente dans la bande de transition ainsi que le temps de retard et la fluctuation du retard en fonction de la fréquence. La bande passante du filtre est de l'ordre de 2 MHz. Dans le but d'obtenir une bonne résolution spectrale et un bon rapport signal sur bruit, le filtre passe bande (BPF) a été optimisé en fonction de la réponse temporelle invariable dans le temps à un signal chirpé.

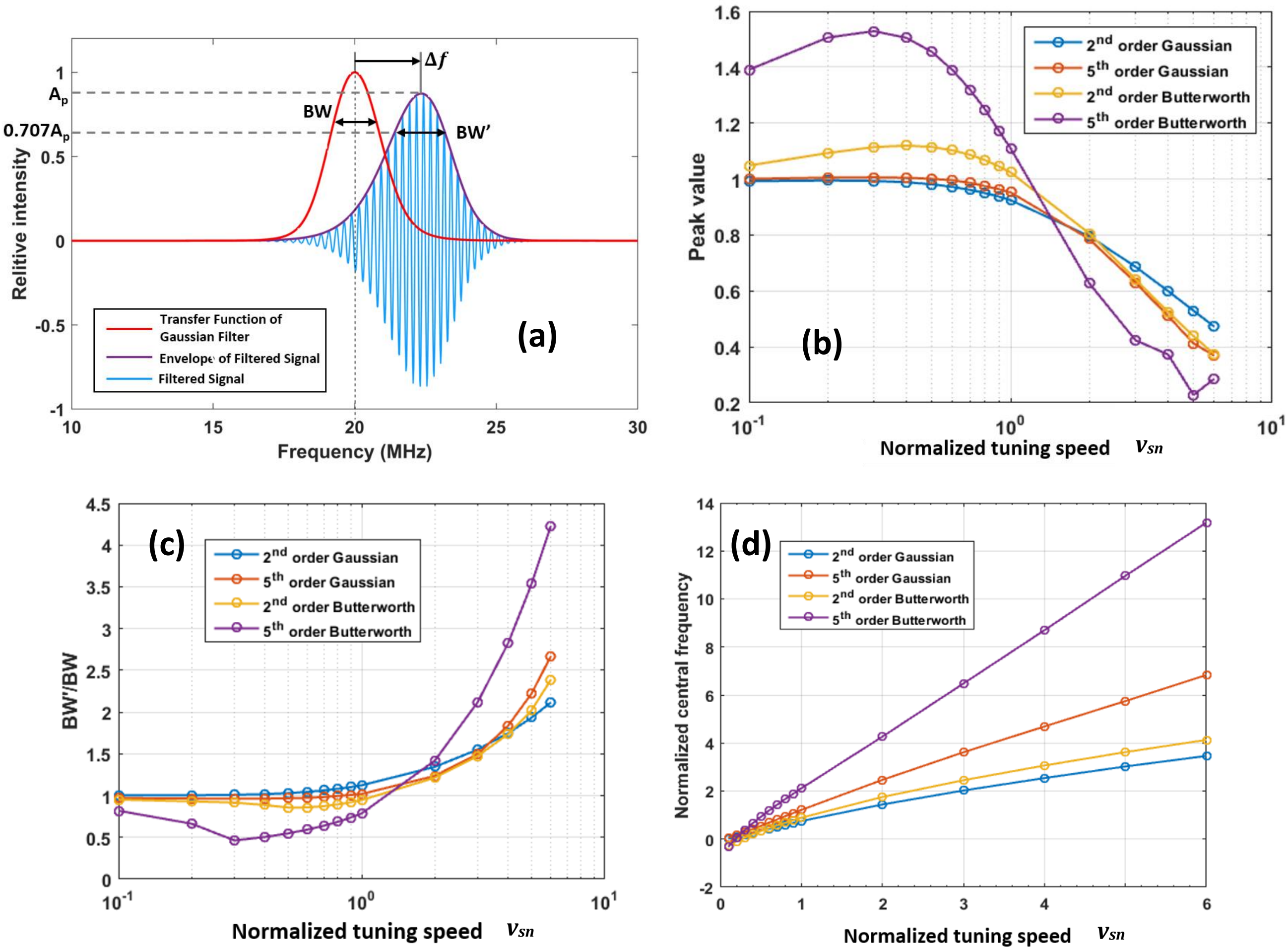

Figure 2. Caractéristiques des signaux crêtes filtrés. **(a).** Illustration de la distorsion du pic filtré en fonction de la fréquence d'entrée chirpée, en considérant l'amplitude, la bande passante et la fréquence centrale. **(b)-(d)**. L'amplitude, la bande passante et le pic filtré en fonction de différentes vitesses de balayage.

On peut voir que les caractéristiques du signal pic en sortie du filtre sont reliées à la réponse normalisée du filtre ainsi qu'à la vitesse de balayage normalisée définie par :

$$v_{sn} = \frac{v_s}{B^2} \; ; \tag{1}$$

v_s est la vitesse de balayage du laser accordable et B est la bande passante du BPF. Pour une vitesse de balayage normalisée élevée, l'intensité crête du signal filtré est atténuée, et la bande passante est élargie.

La figure 2 montre que pour un signal d'entrée chirpé, on observe que la bande passante du filtre, l'amplitude de réponse dépendent du type de filtre et de la vitesse de balayage. La figure 2(a)montre que pour un signal d'entrée chirpé, on observe un décalage en fréquence Δf ainsi qu'un élargissement de la bande passante B'. Si la réponse en fréquence du filtre est symétrique, il n'en est pas de même pour le signal chirpé. On observe un signal qui est atténué de manière moindre pour les faibles fréquences, observation qui est confirmé par la figure 3.

La simulation (figure 2(b)) montre que le filtre gaussien possède une atténuation supérieure et en conséquence, nous avons un meilleur rapport signal sur bruit. Afin d'éliminer la fréquence de répétition, une atténuation de 60 dB dans la bande d'atténuation est requise pour le filtre. La figure 2(b) montre qu'un filtre d'ordre 2 est insuffisant et que le filtre de Butterworth a une réponse en amplitude supérieure au filtre gaussien. Cet effet est nettement visible lorsqu'on prend un filtre d'ordre 5 où on remarque que la réponse en sortie peut être 50% supérieure.

La figure 2c montre l'élargissement de la bande du signal chirpé filtré. On observe pour le filtre de Butterworth une augmentation de la bande avec l'ordre du filtre qui est conséquente et qui va réduire de ce fait la résolution du système. La figure 3(c) montre le décalage de la fréquence centrale pour un signal chirpé et que le filtre de Butterworth d'ordre 5 est particulièrement sensible à la vitesse de balayage.

A cette fin nous avons construit un filtre constitué de deux filtres en cascade, un filtre gaussien et un filtre de Butterworth, les deux filtres sont d'ordre 3. L'atténuation dans la bande d'atténuation d'un filtre d'ordre 3 seul est trop faible pour rejeter la fréquence de répétition et un filtre d'ordre 5 ou 6 ayant une pente dans la bande de transition plus forte, a une fluctuation du retard plus importante, un compromis a été retenu en associant un filtre sans ondulation dans la bande passante et de faible pente à un filtre plus sélectif de Butterworth. La combinaison des deux filtres en cascade permet d'obtenir un filtre ayant une allure gaussienne. L'atténuation apportée par chaque filtre (4 à 6 dB) a été compensée par l'intégration d'amplificateurs, le tout adapté sur une impédance de 50 Ω. Le filtre final a une bande passante de 2,6 MHz.

2.3. Enveloppe du signal de calibrage

Après hétérodynage entre le signal balayé en fréquence et les raies du peigne, le signal est filtré par le filtre passe bande de fréquence centrale f_{cf} autour de 25 MHz. Une détection de l'enveloppe (figure 3(b)) permet d'établir les marqueurs de fréquence. On relève la présence d'un pic principal et les pics secondaires qui sont en autre issus du bruit de phase du laser femto [10].
Les pics secondaires traduisent la fluctuation de phase entre les impulsions laser. Selon la vitesse de balayage, on peut avoir plusieurs dizaines d'impulsions émises entre deux signaux hétérodynes. Avec un laser femtoseconde ayant un asservissement de la fréquence de l'enveloppe et de la fréquence de répétition, les pics secondaires seraient plus fortement atténués voire inexistants bien que dans la littérature aucune équipe n'a complètement réussi à supprimer ces pics secondaires.

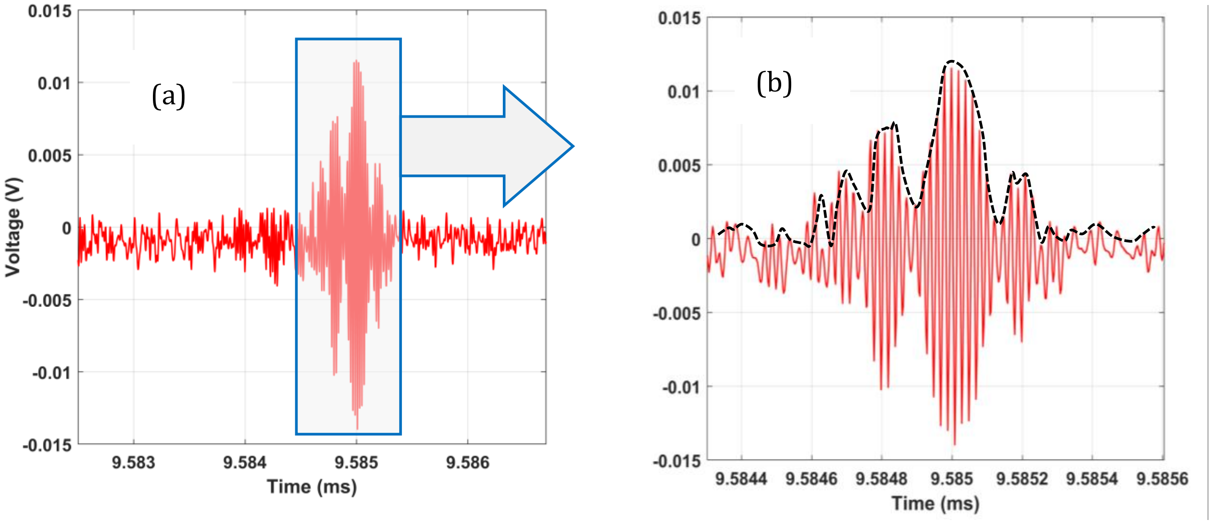

Figure 3. (a) Signal hétérodyne. **(b)** Détection de crête

2.4. Résultats expérimentaux

2.4.1. Calibrage en fréquence du laser accordable

Le montage expérimental pour la mesure de distance absolue est similaire à celui de la figure 1. Le signal filtré est enregistré par un oscilloscope en mode détection de crête. La figure 4 montre les pics de calibrage enregistrés ainsi que la fréquence synthétique de l'interféromètre de référence. La fréquence relative de la $m^{ème}$ paire de pics de calibrage est égale à $\Delta\nu = mf_r$. Afin d'illustrer la précision, l'échelle temporelle a été transformée en échelle fréquentielle dans la figure 4(c) par interpolation des intervalles de fréquence entre les pics de calibrage. La largeur à mi-hauteur mesurée est proche de 1 MHz comme le montre la figure 4(a). Une interpolation linéaire a été appliquée à ces pics de calibrage et la figure 5 montre les résidus de l'interpolation. On peut observer une non-linéarité quasi périodique du laser accordable pour les différentes vitesses de balayage. Ces non-linéarités sont attribuées à l'asservissement de la vitesse de balayage du laser accordable [8].

Les raies du peigne sont en général très fines et peuvent avoir des largeurs du kHz pour des lasers femto asservis [1]. La raie du laser accordable est proche de la centaine de kHz.

Le laser accordable est asservi de manière à avoir aucun saut de mode dans la plage de balayage. Plusieurs paramètres sont en général affectés par l'asservissement, entre autre l'intensité, la vitesse de balayage etc.

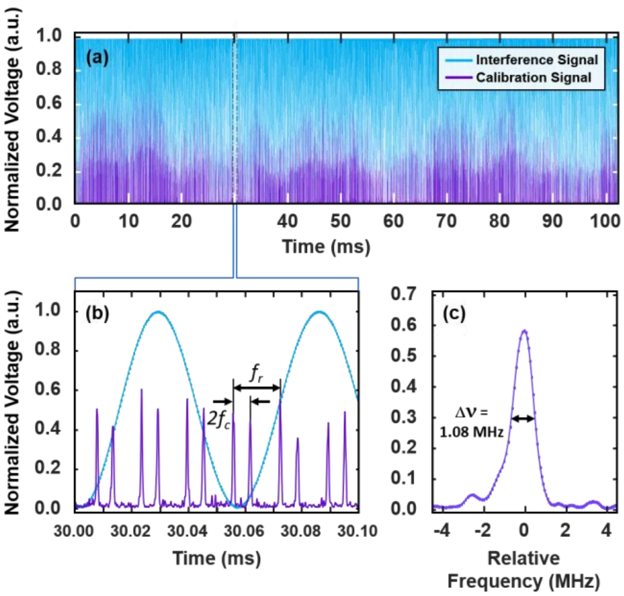

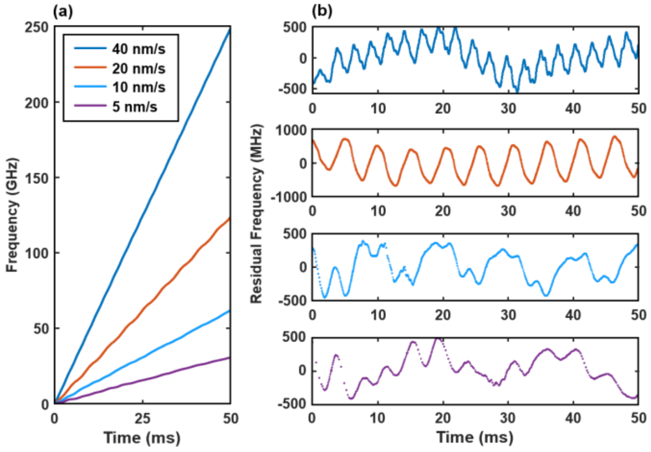

Figure 4. (a). Signal d'interférence et pics de calibrage référencés au peigne de fréquences. **(b).** Zoom de la partie encadrée de la section (a). Chaque paire de pics est produite lorsque la fréquence de balayage se rapproche puis s'éloigne d'une raie du peigne. **(c).** Un autre zoom de (b) montre la largeur spectrale du pic et la grande résolution du pic de calibrage.

Figure 5. (a). La plage de balayage instantanée du laser accordable est quasi-linéaire. **(b).** Fréquences résiduelles de l'interpolation linéaire par rapport à (a). On peut observer différents comportements de balayage non linaire de la source.

2.4.2. Mesurage de distance absolue

Une méthode de comptage de franges a été implémentée pour mesurer la distance absolue de la cible. Comme nous disposons d'une règle de fréquences, à savoir de marqueurs temporels correspondants à chaque signal hétérodyne, il est possible avec une seule acquisition de déterminer un ensemble de sous-mesures. Chaque sous-mesure réalise une mesure déterminée à partir du signal enregistré entre deux marqueurs temporels différents. Ainsi par moyennage il sera possible de réduire l'incertitude de mesure. Pour la $i^{ème}$ mesure, deux pics de calibrage (ou marqueurs temporels) séparés par environ r pics (e.g. 1000) ont été sélectionnés comme pics de départ et de fin de balayage. Le nombre de franges d'interférence $N_i + \varepsilon_i$ a pu être déterminé, où N_i et ε_i sont respectivement la partie entière et la partie fractionnaire du nombre de franges. La distance obtenue par la mesure D_i est déterminée par:

$$D_i = \frac{c}{2n_a} \frac{N_i + \varepsilon_i}{r f_r} \tag{2}$$

où f_r est la fréquence de répétition du peigne, c est la vitesse de la lumière dans le vide et n_a est l'indice de réfraction de l'air.

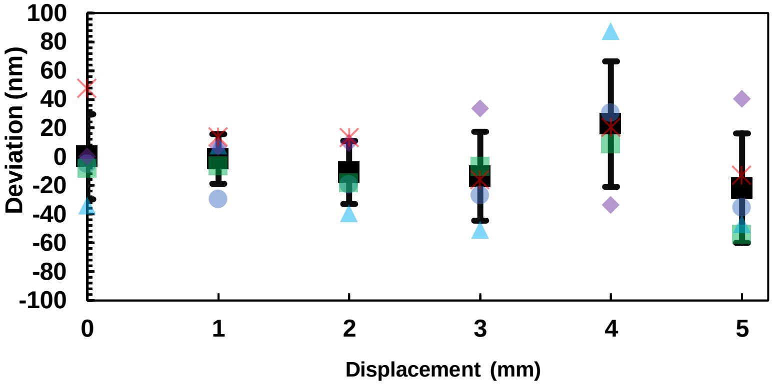

Figure 6. Résultats de mesure pour 6 déplacements de 1 mm à partir de la distance D_0. L'écart de 5 mesures consécutives est inférieur à 80 nm.

Deux mesures adjacentes sont décalées par un pic de calibrage. Ainsi à partir d'un mesurage, R - r mesures peuvent être réalisées, R étant le nombre total de pics de calibrage. Par moyennage de ces mesures, l'écart-type diminue sachant que les incertitudes sur le comptage de fréquence et la détermination du pic sont décorrélées pour les différentes mesures. Pour l'expérience de la mesure de distance, l'interféromètre de mesure a été placé sur une table optique isolée des vibrations environnementales. L'écart maximum sur 5 mesures successives était inférieur à ±80 nm, comme on peut le voir sur la figure 6. Ceci se traduit par une incertitude relative inférieure à 37 parties par milliard (ppb), à un sigma, pour une distance de mesure d'environ 763 mm. La figure 7 confirme qu'avec des déplacements de 1 µm, le micromètre est parfaitement résolu.

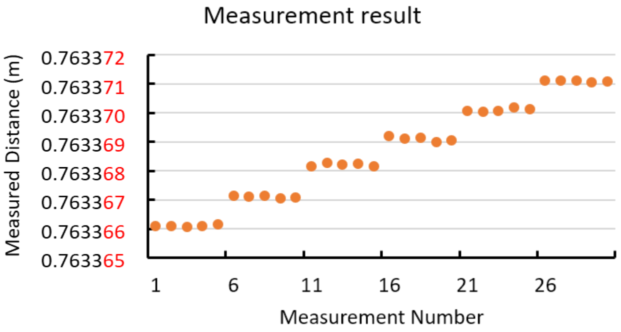

Figure 7. Mesure de distance par pas de déplacement de 1 µm

Ces mesures ont été obtenues sous des conditions environnementales contrôlées. Le système est monté sur une table optique antivibration, et les variations des conditions atmosphériques au niveau de la température, de la pression et de l'hygrométrie sont contenues à des valeurs minimales. Toute turbulence est évitée par une isolation phonique et thermale du chemin optique. En effet la moindre vibration ou variation de chemin optique est amplifiée par un facteur égal au rapport de la longueur d'onde synthétique divisée par la longueur d'onde.

2.4.3. Mesure de vibrations

Durant les phases de mesure nous avons observé une grande sensibilité du système aux perturbations ce qui nous a conduit à évaluer ces dernières. En effet comme le montre la figure 8(a) la technique de sous mesures permet de reconstruire intégralement l'évolution du signal dans le temps en fonction du balayage. On observe les vibrations dans la reconstruction des mesures. Deux facteurs sont à l'origine des vibrations : la première une fluctuation du chemin optique due aux turbulences atmosphériques et la deuxième une vibration de la cible ou du coupleur émetteur de l'interféromètre de mesure.

Avec le principe de mesure proposé, il est également possible de déterminer la vibration de la cible étant donné que la durée de mesure est très courte. Une expérience de mesure de vibrations a été effectuée en plaçant un transducteur piézoélectrique (PZT) au niveau du rétro-réflecteur de mesure et en appliquant une vibration délivrée par un générateur de fonctions. La figure 8 montre les résultats de mesures.

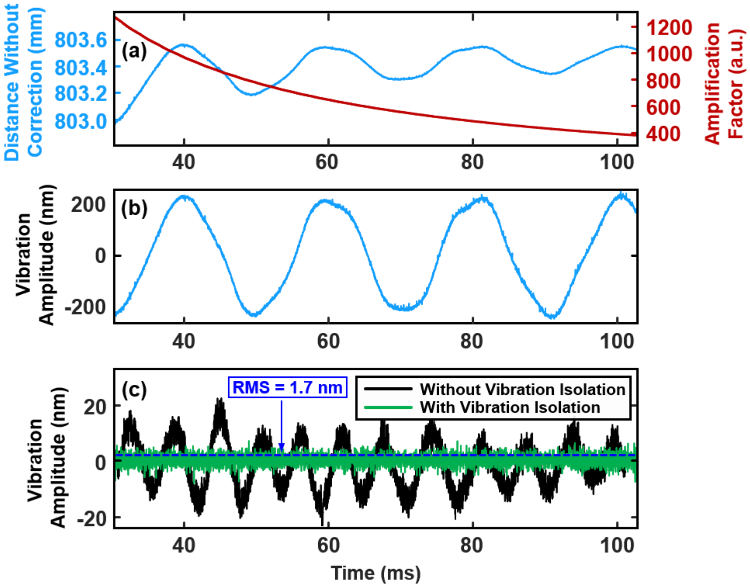

Figure 8. Résultats des mesures de vibrations. **(a).** Mesure de la distance d'une cible mise en vibration par un PZT et le facteur d'amplification résultant. Comme les points finaux des mesures sont décalées par un pic de calibrage, la plage de balayage de fréquence augmente de f_r , se traduisant par une décroissance du facteur d'amplification avec la durée de balayage. **(b).** Vibration extraite à partir de (a). **(c).** Vibration d'une cible avec et sans isolation de la vibration. La vibration est introduite par les ventilateurs des instruments. On relève qu'il est possible de détecter des vibrations avec une sensibilité proche de quelques nanomètres.

En figure 8(c) on observe la fluctuation de la mesure en présence de perturbations externes provenant dans ce cas de la ventilation des instruments et proches de la fréquence de 150 Hz. Après isolation du montage de ces vibrations le niveau de bruit est réduit à 1,7 nm ce qui présage la capacité de mesure de vibration ayant des amplitudes de la dizaine de nanomètres.

3. Conclusion

Dans le présent travail, un système de mesure de distance par FSI référencé avec un peigne de fréquences d'un laser femtoseconde a été étudié. La fréquence de répétition d'un laser femtoseconde sans asservissement a été mesurée durant le balayage de fréquence d'un laser accordable afin de corriger l'instabilité à long terme du laser femto seconde. L'exactitude de la mesure de distance a été améliorée en tirant avantage du grand nombre de raies du peigne. Une incertitude relative de 37×10^{-9} sur la mesure de la distance a été obtenue sur une longueur proche de 1 mètre. Ce résultat montre les performances qu'on peut attendre de cette technique. En plus, grâce à cette technique de référencement par un peigne de fréquence, des mesures de vibrations sur la cible objet avec une sensibilité proche du nanomètre ont été démontrées.

Références bibliographiques

[1] D. H. Phung, C. Alexandre, and M. Lintz, "Two-mode interference measurement for nanometer accuracy absolute ranging," *Opt. Lett.,* vol. 38, no. 3, pp. 281-283, 2013.

[2] O. P. Lay *et al.*, "MSTAR: a submicrometer, absolute metrology system," , *Opt. Lett.,* vol. 28, no. 11, pp. 890-892, Jun 1 2003.

[3] J. A. Stone, A. Stejskal, and L. Howard, "Absolute interferometry with a 670-nm external cavity diode laser," *Appl. Opt.,* vol. 38, no. 28, pp. 5981, 1999.

[4] C. Lu, G. Liu, B. Liu, F. Chen, and Y. Gan, "Absolute distance measurement system with micron-grade measurement uncertainty and 24 m range using frequency scanning interferometry with compensation of environmental vibration," *Opt. Express,* vol. 24, no. 26, pp. 30215, 2016.

[5] A. Cabral and J. Rebordao, "Absolute distance metrology with frequency sweeping interferometry," *SPIE,* vol. 5879, 2005.

[6] N. Schuhler, Y. Salvadé, S. Lévêque, R. Dändliker, and R. Holzwarth, "Frequency-comb-referenced two-wavelength source for absolute distance measurement," *Opt. Lett.,* vol. 31, no. 21, pp. 3101, 2006.

[7] E. Baumann *et al.*, "Comb-calibrated frequency-modulated continuous-wave ladar for absolute distance measurements," *Opt. Lett.,* vol. 38, no. 12, pp. 2026, 2013.

[8] P. Perret and P. Pfeiffer, "Sinusoidal nonlinearity in wavelength-sweeping interferometry," *Appl. Opt.,* vol. 46, no. 33, pp. 8074-8079, 2007.

[9] A.M. Zollot, F.R. Giorgetta, E. Baumann, J. W. Nicholson, W.C. Swann, I. Coddington and N.R. Newburry, "Direct comb molecular spectroscopy with accurate resolved comb teeth over 43 THz," *Opt. Lett.,* vol. 42, no. 14, pp. 2718, 2017.

[10] F. R. Giorgetta, I. Coddington, E. Baumann, W. C. Swann, and N. R. Newbury, "Fast high-resolution spectroscopy of dynamic continuous-wave laser sources," *Nature Photonics,* vol. 4, no. 12, pp. 853, 2010.

Publications relatives à la thèse

1. **Wenhui Yu**, Pierre Pfeiffer, Joël Fontaine, "Filter design for dynamic frequency calibration of an external cavity diode tunable laser using frequency comb", Proc. SPIE 10680, Optical Sensing and Detection V, 106800G (9 May 2018); doi: 10.1117/12.2305865;

2. **Wenhui Yu**, Pierre Pfeiffer, Sylvain Lecler and Joël Fontaine, "Effect of Phase Noise on the Frequency Calibration of a Tunable Laser by Heterodyne Signal Filtering," IEEE Journal of Quantum Electronics. doi: 10.1109/JQE.2018.2879482

4. **Wenhui Yu**, Pierre Pfeiffer, Alireza Morsali, Jianming Yang, Joël Fontaine, "High precision absolute distance and vibration measurement by comb calibrated frequency sweeping interferometry". *In reviewing process*